ANODIC DISSOLUTION OF URANIUM DIOXIDE IN SIMPLE ELECTROLYTE SOLUTIONS AND SIMULATED GROUNDWATERS

A Thesis
Presented to
The Faculty of Graduate Studies
of
The University of Manitoba

by
JODI L. M. LUHT

In partial fulfillment of requirements
for the degree of
Master of Science
April 27, 1998

THE UNIVERSITY OF MANITOBA

FACULTY OF GRADUATE STUDIES

*****

COPYRIGHT PERMISSION PAGE

ANODIC DISSOLUTION OF URANIUM DIOXIDE IN SIMPLE ELECTROLYTE SOLUTIONS AND SIMULATED GROUNDWATERS

BY

JODI L.M. LUHT

A Thesis/Practicum submitted to the Faculty of Graduate Studies of The University of Manitoba in partial fulfillment of the requirements of the degree of

MASTER OF SCIENCE

ABSTRACT

The anodic dissolution of UO_2 has been studied in $NaClO_4$, NaCl, Standard Canadian Shield Saline Solution (SCSSS) and SCSSS + HCO_3^- solutions using potentiostatic and cyclic voltammetry techniques. Under potentiostatic conditions two oxidation/dissolution regions were observed. Over the anodic potential range $0.1V \leq E \leq 0.425V$ (vs. SCE) currents decayed continuously with time due to the formation of oxidized surface films which blocked dissolution. Using X-ray photoelectron spectroscopy and scanning electron microscopy, the UO_2 surface was determined to be blocked by a thin film of $UO_{2.33}$ and a deposited U^{VI} solid which was distributed uniformly over the surface. In $NaClO_4$ and NaCl solutions, the U^{VI} solid was a $UO_3.2H_2O$ deposit, while in SCSSS and SCSSS + HCO_3^- solutions, the dissolution/deposition process was blocked by the incorporation of calcium and silicon ions into the U^{VI} solid. Over the anodic potential range $0.425V \leq E \leq 0.55V$ (vs. SCE), the rate of $UO_{2.33}$ film formation was equal to the rate of its oxidative dissolution as UO_2^{2+} (i.e. steady state conditions). In all four solutions, the dissolution / hydrolysis / acidification rate was sufficiently rapid to establish local acidity at high anodic potentials. This local acidity lead to an increase in local solubility of U^{VI} which was then transported away from the dissolution sites as UO_2^{2+} rather than deposited as a U^{VI} solid. After anodic oxidation in SCSSS, steady state was established at a higher potential than that for $NaClO_4$ and NaCl which indicated

that calcium/silicon containing U^{VI} phases blocked the oxidative dissolution process until a higher potential was reached. Conversely, after anodic oxidation in SCSSS + HCO_3^-, steady state was established at a lower potential than that for $NaClO_4$ and NaCl which indicated that HCO_3^- accelerated the oxidative dissolution process despite the presence of calcium and silicon ions.

TABLE OF CONTENTS

1.0 INTRODUCTION

1.1 MOTIVATION FOR STUDYING UO_2

The Canadian Nuclear Fuel Waste Management Program is located at the Whiteshell Laboratories, 100 kilometers north east of Winnipeg. In this program, a concept has been developed for the geological disposal of fuel waste resulting from the operation of nuclear generating stations.

The waste will be in the form of CANDU (CANada Deuterium Uranium) fuel bundles. It would be sealed in a corrosion resistant metallic container. These containers would be emplaced in rooms in a disposal vault 500 to 1000 meters deep in granite rock in the Canadian Shield. Each waste container would be separated from the rock by a clay buffer material, and each room sealed with a clay/crushed rock backfill (Figure 1.1) [1].

Radionuclide release will commence when the groundwater corrodes through the containers, and comes into contact with the uranium dioxide (UO_2) fuel. This will result in the dissolution of the UO_2 matrix, and the release of radionuclides by two mechanisms (Figure 1.2):

1. rapid release (hours to days) of 2% of the total inventory of volatile fission products (^{135}Cs, ^{129}I, ^{14}C, ^{36}Cl) from the gap and grain boundaries. The gap region is the area between the UO_2 and the Zircalloy sheath, and the grain boundaries are the areas between each grain of UO_2;
2. slower release (10 to 1,000,000's years) of the remaining inventory of radionuclides.

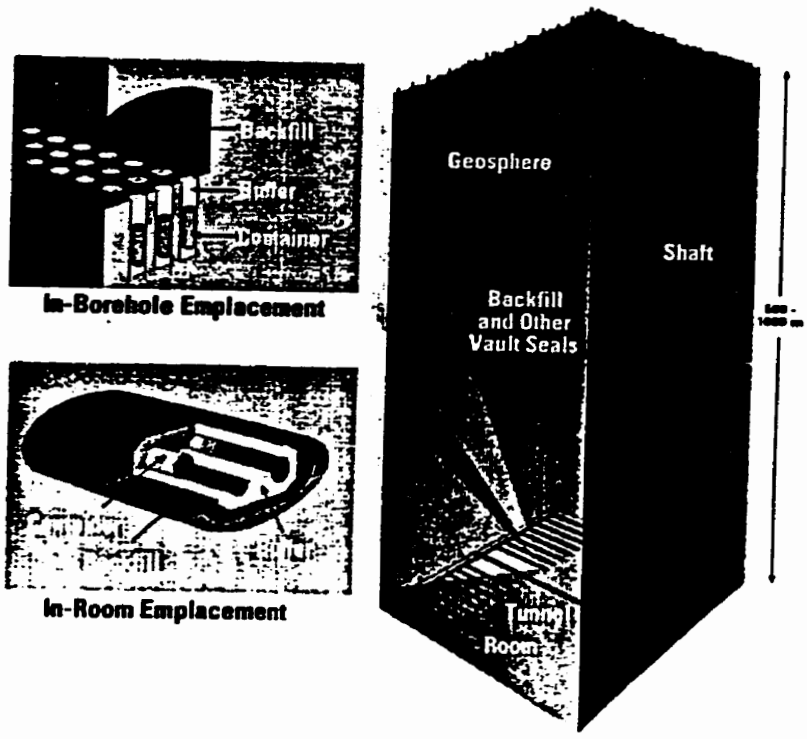

FIGURE 1.1: Schematic representation of a Nuclear fuel Waste Disposal Vault in the Canadian Shield [1].

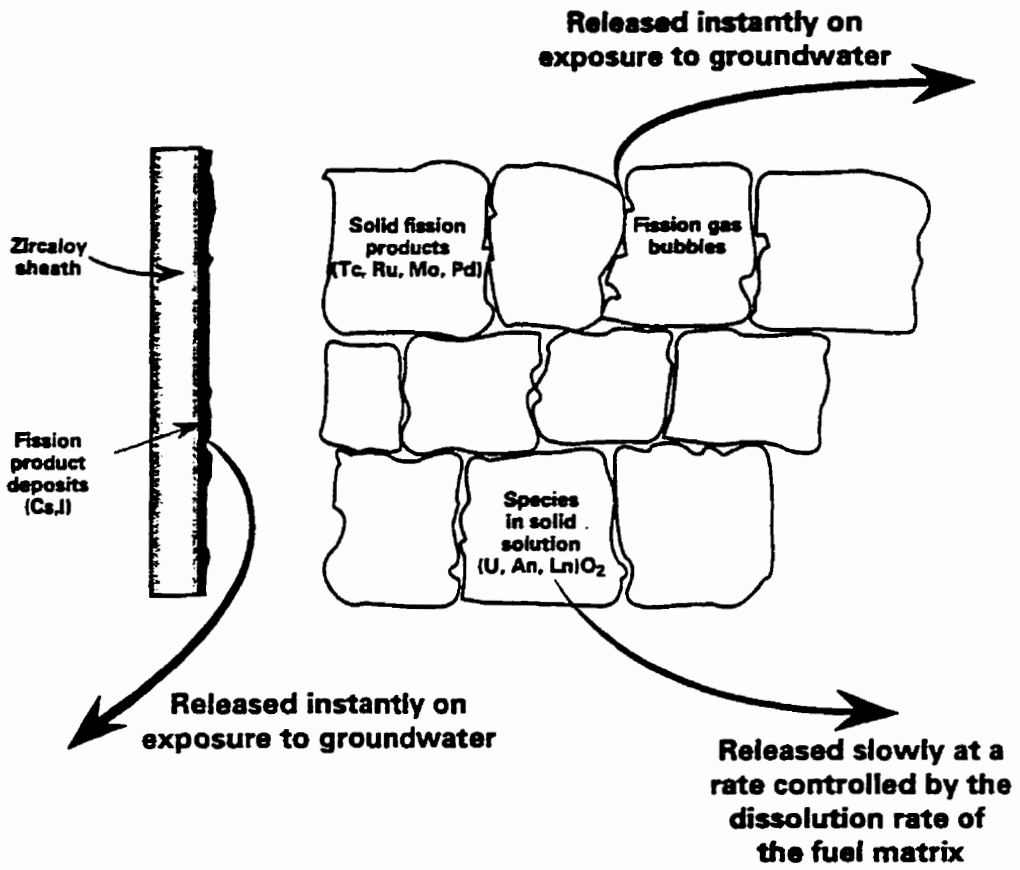

FIGURE 1.2: Schematic illustrating the release of radionuclides from used fuel [1].

The majority of radionuclides (> 90 %) are found in the grains of the fuel pellets and will be released as the UO_2 matrix dissolves.

A major problem in measuring the dissolution rate of UO_2 is the dependence of uranium solubility on the redox condition [2-6]. The dissolution rate will be related to the solubility of the phase present on the UO_2 surface

[6,7,8] when the fuel surface is in equilibrium with the surrounding redox environment [9,10]. The solubility-limited boundary condition defines the dissolution process as being chemical, not electrochemical, and is justified under non-oxidizing conditions since U^{IV} is highly insoluble, with measured solubilities in the range from 10^{-6} to 10^{-12} mol.L^{-1} [7-9,11]. The solubility of U^{VI} is generally several orders of magnitude higher, with a value in synthetic groundwaters $>10^{-6}$ mol.L^{-1} [11]. Under oxidizing conditions, UO_{2+x} dissolves to form UO_2^{2+} and associated hydrolysis products [11]. As well, groundwater species may also complex with uranyl ions and enhance the solubility of UO_2 [11]. Hence, under oxidizing conditions, the solubility boundary condition is not justified since dissolution is irreversibly driven by oxidants present in the vault. The redox condition at the fuel surface, is established by the balance between the kinetics of the anodic and cathodic reactions involved in the corrosion of UO_2 [12]. Therefore, an experimental program has been established to determine the mechanism and kinetics of UO_2 dissolution over a wide range of redox conditions, from oxidizing to non-oxidizing.

Redox conditions in a waste vault will be initially oxidizing due to the oxygen trapped in the buffer and backfill materials upon vault closure. Over time, conditions will become non-oxidizing as the oxygen is consumed by corrosion of the metallic container and by reaction with minerals and organic material contained in the buffer and backfill materials. However, once containers fail and the fuel is exposed to groundwater, conditions within the container could become oxidizing due to the production of oxidants by the radiolysis of water [2,13].

Consequently, we would expect the dissolution of UO_2 to be a major mechanism for release of the radionuclides into the groundwater. The oxidizing agents available to drive the dissolution are dissolved oxygen, and hydrogen peroxide and radicals produced by the radiolysis of water [2].

Since the dissolution rate of UO_2 depends on the redox conditions at the fuel surface, it can be expressed as a corrosion process and determined based on electrochemical principles. The electrochemical nature of UO_2 dissolution has been demonstrated by many studies [2,13-25]. In these studies dissolution rates were measured by using a combination of electrochemical and natural corrosion experiments. Electrochemical methods are very useful for studying rates since the potential at the surface of the UO_2 can be controlled. By using electrochemical methods, a corrosion reaction can be separated into two half reactions and the rate dependence on potential for each half reaction can be determined. The overall anodic half reaction is,

$$UO_2 \rightarrow UO_2^{2+} + 2e \qquad (1.1)$$

and the cathodic reaction is,

$$Ox + ne \rightarrow Red \qquad (1.2)$$

where Ox represents the various oxidizing agents and Red is the species formed by its reduction.

1.2 JUSTIFICATION AND SCOPE

The dissolution rates of uranium from used UO_2 nuclear fuels and release rates of radionuclides from these fuels have been measured as part of a program to assess the disposal of used nuclear fuel. Attempts have also been made to develop models to predict the dissolution and radionuclide release rates under deep geological disposal conditions in granite rocks. Although only a few comparisons have been made between the measured and the predicted values, they are generally in good agreement. However, to fully justify these models, a more extensive comparison of measured and predicted values is required.

The most rapid release of radionuclides is expected to occur under oxidizing conditions. Under these conditions fuel dissolution is an electrochemical process in which the oxidative dissolution of UO_2 is driven by the reduction of available oxidants. The main sources of oxidants are products of water radiolysis (by alpha, beta and gamma radiation) due to the decay of radionuclides in the fuel, and dissolved oxidants (predominantly oxygen). Consequently, the model for fuel dissolution is based on electrochemical measurements in which the dissolution rate is calculated from electrochemical currents.

In this model the dissolution currents are measured on UO_2 electrodes as a function of the applied electrochemical potential (Tafel plots) to determine the anodic dissolution of UO_2. The currents are extrapolated to the steady state corrosion potential measured in solutions containing various concentrations of

oxidants. In this procedure, the rate of fuel dissolution as a function of oxidant concentration has been predicted for hydrogen peroxide concentrations, and gamma and alpha radiation dose rates.

The Tafel relationship must be understood in more detail for reliable dissolution rates to be predicted. To date, this relationship has been studied in solutions containing simple electrolytes ($NaClO_4$, NaCl, $NaHCO_3$). However, the groundwaters available in the disposal vault are expected to contain a more complex mixture of electrolytes. Consequently, the primary focus of this project will be to concentrate on how the steady state electrochemical currents for the anodic dissolution of UO_2, and therefore the corrosion rate, change with natural and/or simulated groundwater composition. Based on these studies, an attempt to verify the proposed mechanism for the oxidative dissolution of UO_2 has been made.

2.0 LITERATURE REVIEW

2.1 FUEL COMPOSITION

Uranium oxide fuels are ceramic pellets that have been fabricated by pressing fine grained oxide powders and then sintering them at ~1700°C under a reducing atmosphere [16, 26, 27]. The sintered pellets have grain sizes in the range 2 - 15 μm and contain non-interconnected submicron pores. Uranium dioxide fuels are slightly hyper-stoichiometric in composition consisting of UO_{2+x}, where $0.01 \geq x \geq 0.0001$ [26, 28]. The composition can vary slightly depending on conditions during fabrication. During the reductive sintering process, the defects in UO_{2+x} (in the form of O^{2-} interstitial ions) will segregate to the grain boundaries. If the reducing process is incomplete, there will be a higher degree of hyper-stoichiometry with the UO_{2+x} present most probably in the grain boundaries (Figure 2.1).

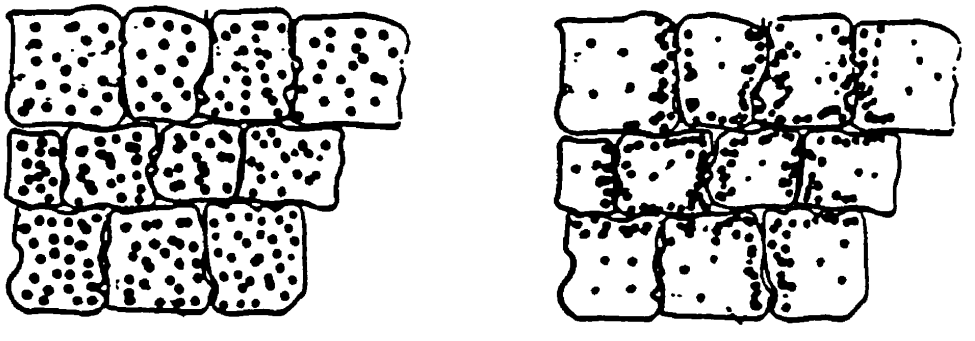

FIGURE 2.1: (A) Distribution of oxidized U atoms before sintering; (B) Possible distribution of oxidized U atoms after incomplete reductive sintering.

During reactor irradiation many fission products and actinides, with varying solubilities in the UO_2 matrix, are created inside the fuel matrix [16, 29]. The actinides substitute for uranium in the UO_2 lattice, whereas many fission products (e.g. Xe, Kr, I, Br, Cs, Rb, Zr, Mo, Te, Tc, Ru, Rh, Pd, Cd and Sn) are initially trapped at defect sites but gradually segregate to either grain boundaries or the fuel cladding gap by thermal and radiation-enhanced diffusion [12, 16, 29-37]. A small increase in hyperstoichiometry as a function of burnup is also expected because the valence of fission products is generally less than 4 [38, 39].

2.2 ELECTRICAL PROPERTIES

Figure 2.2 [16] shows an energy level diagram for UO_2. A narrow U 5f band lies in the gap between the filled valence band and the empty conduction band. This U 5f band has two electrons per uranium atom for stoichiometric UO_2. For stoichiometric UO_2, the source of electronic conductivity to promote electrons from the occupied U 5f level to the conduction band has a high activation energy (Ea ~ 1.1 eV), and therefore a low probability at room temperature [40-43]. Usually, UO_2 fuel pellets have a slight excess of oxygen present as interstitial O^{2-} ions up to a composition near $UO_{2.33}$ with the overall charge balance maintained by ionization of U^{4+} ions to the U^{5+} and/or U^{6+} valence state [25,42-44]. This creates holes in the narrow occupied U 5f band. The holes can migrate by the polaron hopping mechanism with a low activation

energy (Ea ~ 0.2 eV) [25, 42-44]. Consequently, hyperstoichiometric UO_2 will conduct an electric current for electrochemical reactions to occur and will exhibit behaviour similar to a p-type semiconductor.

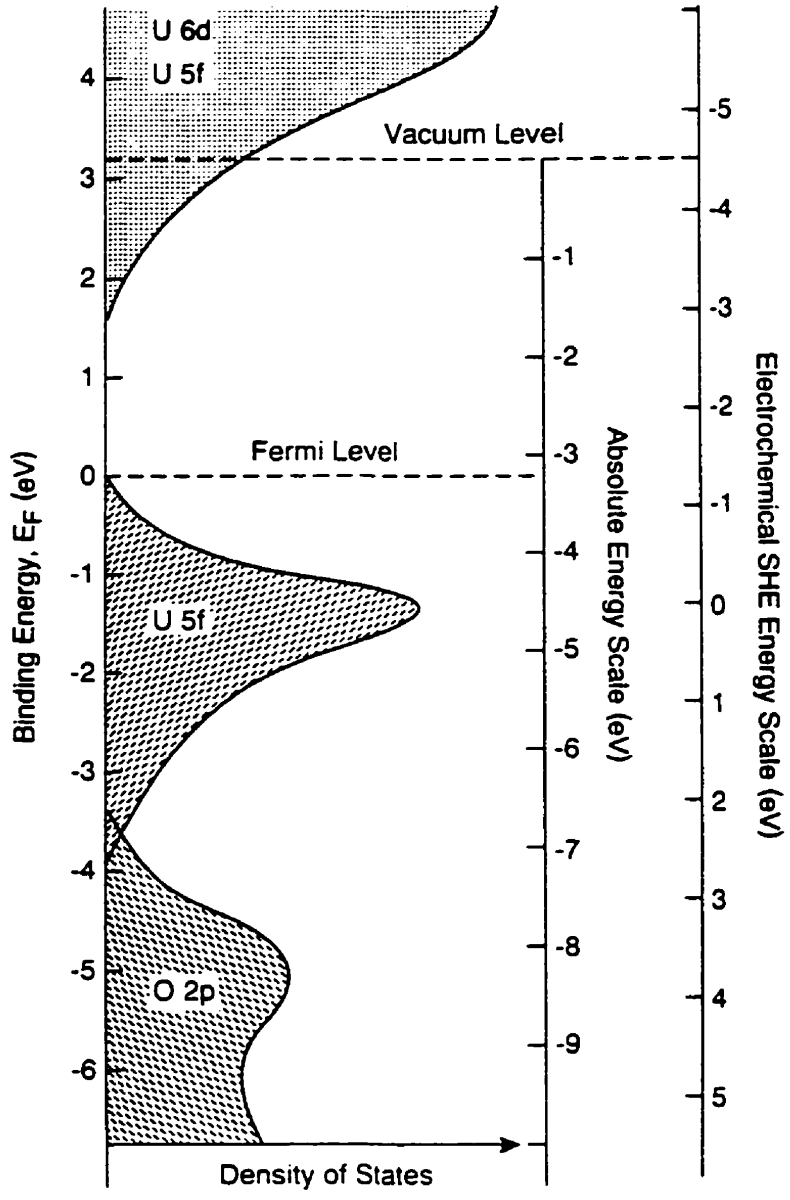

FIGURE 2.2: Schematic energy-level diagram for UO_2 from electrochemical and spectroscopic data. The filled valence band has O 2p character and the empty conduction band has mainly U 5f, 6d and 7s states [16].

As the electrode is polarized to more cathodic potentials, a point must be reached in which most of the holes have migrated away from the surface resulting in a potential gradient across the surface as well as at the electrode / solution interface [25]. The change from ideally polarizable to capacitive electrode behaviour occurs at the flatband potential, E_{fb}. A normal p-type semiconductor would exhibit an abrupt transition at its flatband potential, but more gradual changes are expected for UO_{2+x} because of the larger number densities of holes with low mobilities [25,45]. A flatband potential (E_{fb}) in dilute aqueous solutions at pH 9.5 of -1.7 ± 0.4 V (vs SCE) has been calculated [46]. This is an unusually negative flatband potential, but has allowed electrochemical experiments to be performed on UO_{2+x} at significantly more cathodic potentials than you would usually find on a normal p-type semiconductor [45].

Figure 2.3 illustrates how the presence of O^{2-} interstitials produces p-type conductivity. Initially, slight oxidation of UO_2 injects O^{2-} at interstitial sites which are readily available in UO_2 (Figure 2.4) followed by the oxidation of a sufficient number of U^{4+} to U^{5+} atoms at lattice sites to maintain overall electroneutrality.

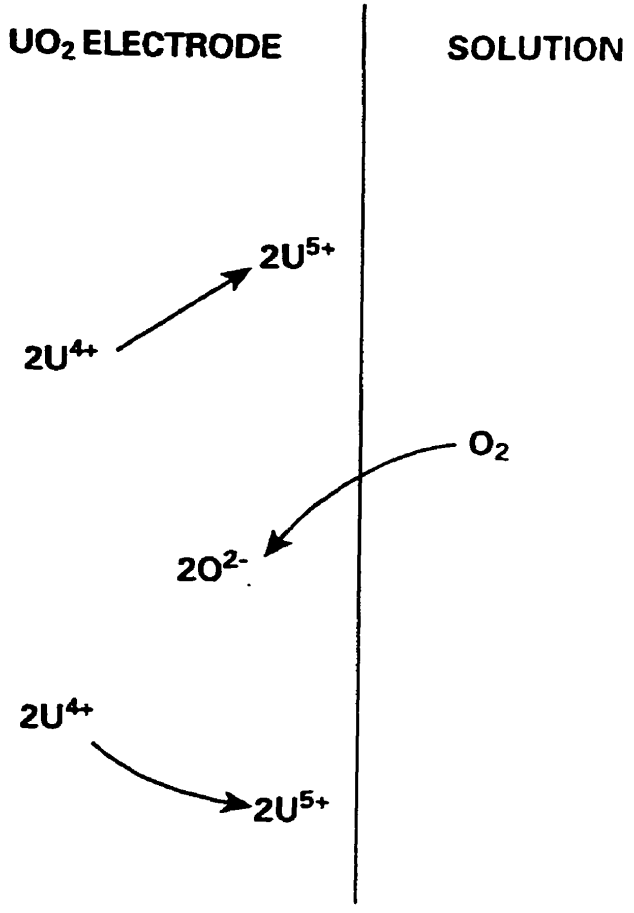

FIGURE 2.3: Illustration of O^{2-} interstitials producing p-type conductivity at the UO_2 surface / solution interface.

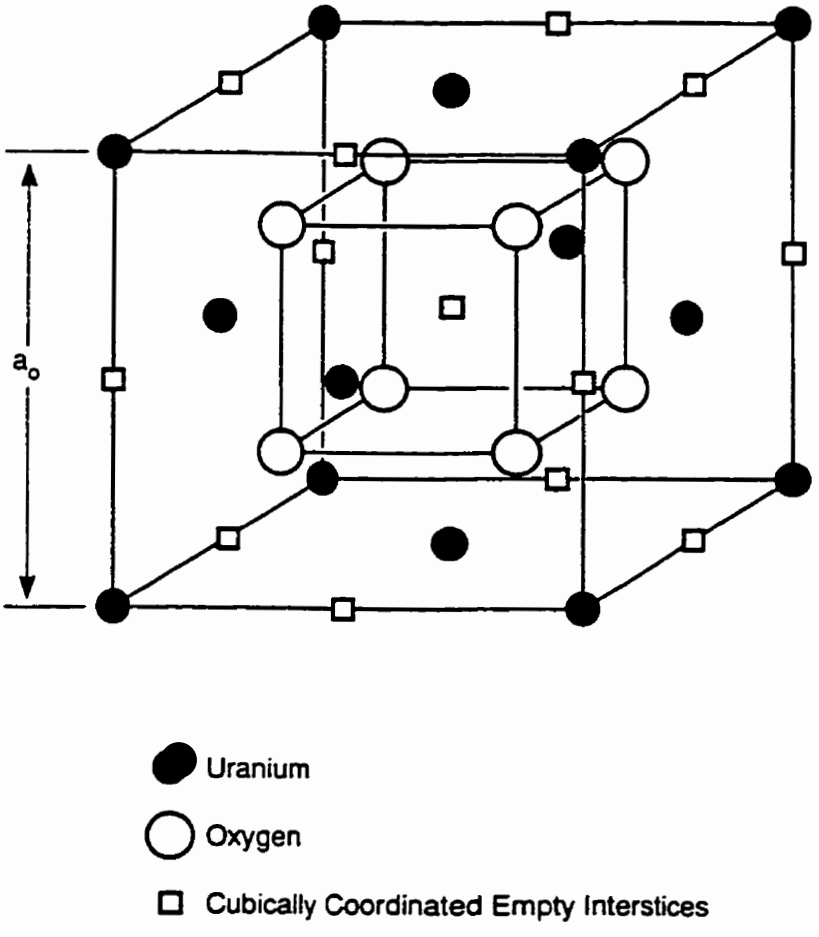

FIGURE 2.4: Schematic of the cubic fluorite structure of UO_2 [16].

2.3 STRUCTURAL AND SOLID STATE PROPERTIES OF URANIUM OXIDES

Figure 2.5 [16] shows a simplified energy level diagram, which illustrates the expected behaviour of UO_2 when exposed to aerated solutions at pH 9.5.

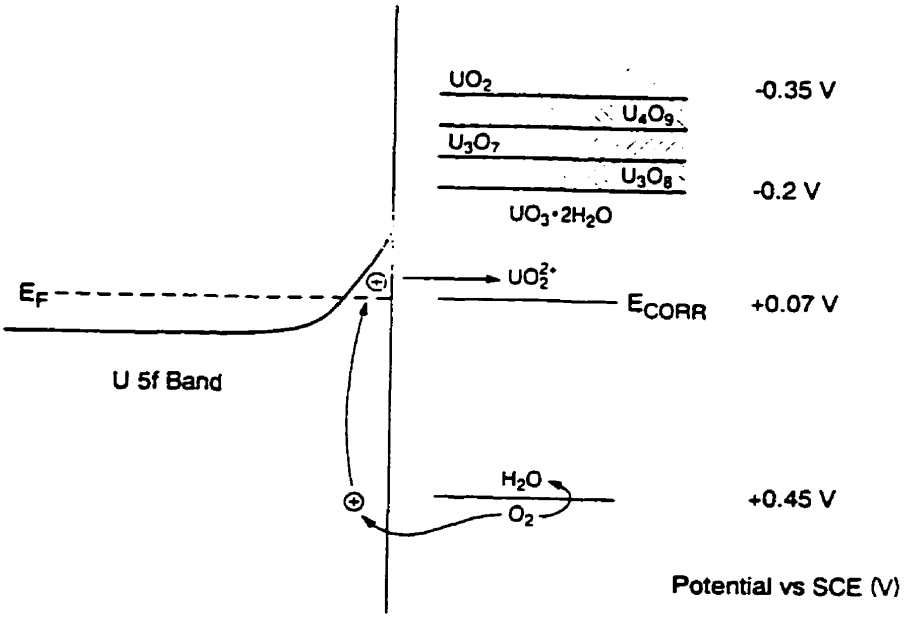

FIGURE 2.5: Simplified energy level diagram for UO_2 to illustrate the expected behaviour of UO_2 exposed to aerated solutions at pH 9.5 [16].

The range of equilibrium potentials (E_e) for oxide transformations is ~-0.35 to -0.2 V versus Saturated Calomel Electrode (SCE). However, reaction with oxygen in aerated solutions is capable of driving the corrosion potential (E_{corr}) much more positive than this range [21]. As a result, complex oxide chemistry is

thermodynamically possible.

The dissolution of UO_2 will take place from a surface of UO_{2+x}, where x is determined by the redox conditions at the dissolving surface. The surface composition and semiconducting properties will influence the kinetics of both the anodic dissolution and cathodic reduction reactions.

A review of the phase relationships, crystal structures and semiconducting properties of the phases that may affect UO_2 reactivity (particularly oxidative dissolution) are briefly discussed below.

2.3.1 UO_2 to $UO_{2.25}$ ('UO_2 to U_4O_9')

In the composition range UO_2 to U_4O_9, all the phases are based on the fluorite structure (Figure 2.4). Each metal atom is surrounded by eight equivalent nearest neighbor oxygen atoms, which in turn are surrounded by a tetrahedron of four equivalent metal atoms. An important feature of this lattice is that it has large cubically coordinated interstitial sites which can accommodate additional oxygen atoms. As the composition deviates from $UO_{2.00}$ to UO_{2+x}, density and X-ray measurements have indicated that the unit cell size shrinks [47]. Also, neutron diffraction measurements have shown that small defect structures are formed without disruption of the overall symmetry of the lattice [48,49]. An increase in oxygen in the interstitial sites from $UO_{2.00}$ to $UO_{2.06}$ results in a substantial increase in electrical conductivity [41, 44, 50]. The conductivity is p-type since positive holes are the charge carriers and move by a hopping mechanism as the holes jump between uranium cation sites [44].

2.3.2 $UO_{2.25}$ ('U_4O_9')

For the composition $UO_{2.25}$, the structure is based on the fluorite structure, with uranium atoms being displaced to accommodate interstitial oxygen [48]. Eventually, increases in the oxygen content lead to derivative phases such as UO_{2+x} and U_4O_{9-y}. Non-stoichiometric U_4O_9 is an n-type semiconductor and is anion deficient [44, 50, 51]. Therefore, as the oxidation of UO_2 proceeds there is the possibility to develop mixed p-type / n-type conductivity. The mixed conductivity could result in heterogeneous dissolution since n-type sites support cathodic processes and p-type sites support anodic dissolution.

2.3.3 $UO_{2.33}$ ('U_3O_7')

The composition $UO_{2.33}$ is the end of the fluorite structure range. Further oxidation induces a complete transformation to a more open configuration with a significantly lower density. Several different phases near a composition $UO_{2.33}$ have been obtained by the oxidation of UO_2 and U_4O_9. The phase α-U_3O_7 is tetragonal with a distorted fluorite structure and can be considered an extension of the UO_{2+x} and U_4O_{9-y} structures and exhibit n-type conductivity [50, 51, 52].

2.3.4 $UO_{2.5}$ ('U_2O_5')

The composition of U_2O_5 has been reported and is thought to exist only at pressures > 10^3 MPa [53]. Three phases with U_2O_5 composition have structures

in between the fluorite structure and the layer structure found in orthorhombic higher oxides. The U_2O_5 composition is thought to represent the change from U^{4+} and U^{5+}, which controls the lower oxide structures, and U^{5+} and U^{6+}, which controls the higher oxide structures [54]. Also, it has been claimed that the U_2O_5 composition is where U^{6+} oxide dissolution begins to dominate the redox chemistry, as discussed below in Section 2.4.

2.3.5 $UO_{2.5}$ to $UO_{2.67}$ ('U_2O_5 to U_3O_8')

Twelve different phases have been reported in the composition range from U_2O_5 to U_3O_8 [54]. The U_3O_8 composition is generally non-stoichiometric, U_3O_{8-p}, and exhibits n-type semiconducting properties due to its oxygen deficiency [50, 51, 55]. Overall, the structure is similar for compositions in the range from U_2O_5 to UO_3.

2.3.6 $UO_{3.00}$ (Hydrated oxides ($UO_3.2H_2O$ and $UO_2(OH)_2$))

Hydrated uranium oxides are generally formed once uranium is fully oxidized to U^{6+}. The $UO_3.2H_2O$ phase is the stable hydrate around room temperature [56]. The $UO_2(OH)_2$ phase is important in dissolution kinetics, because it appears to limit oxidative dissolution rates in alkaline solutions. The $UO_2(OH)_2$ phase consists of uranyl groups bonded to hydroxyl groups in a layered structure, and is expected to be formed by the oxidation of U_3O_8 in aqueous solutions [54, 56, 57].

2.4 ELECTROCHEMISTRY OF UO_2 DISSOLUTION

2.4.1 Thermodynamic Properties

The redox potential is the most important parameter for the dissolution of UO_2 and the release of radionuclides since the solubility of UO_2 depends on the redox potential of the exposure environment.

The calculated solubility of uranium in water as a function of pH in both reducing (UO_2) and oxidizing ($UO_3.2H_2O$) conditions is shown in Figure 2.6A [16]. Figure 2.6B [16] shows the distribution of the most stable solution soluble species as a function of the redox potential and pH for a defined uranium concentration of 10^{-6} mol.L^{-1}.

The uranyl ion, UO_2^{2+}, is the soluble form of U^{VI} and the U^{IV} dissolves as the U^{4+} ion. However, both ions, especially U^{4+}, are extensively hydrolyzed in aqueous solutions and form species such as $U_x(OH)_y^{(4x-y)+}$ for U^{4+} at pH > 1 and $(UO_2)_x(OH)_y^{(2x-y)+}$ for UO_2^{2+} at pH > 4 [3, 4, 58, 59]. Also, the stability of uranium in aqueous solution may be enhanced by complexation with inorganic and organic anions leading to an increase in the solubility of U^{VI} and U^{IV} over the neutral to alkaline pH range [3, 4, 6, 58-60]. Some of these complexation effects will be discussed below in the section on groundwaters.

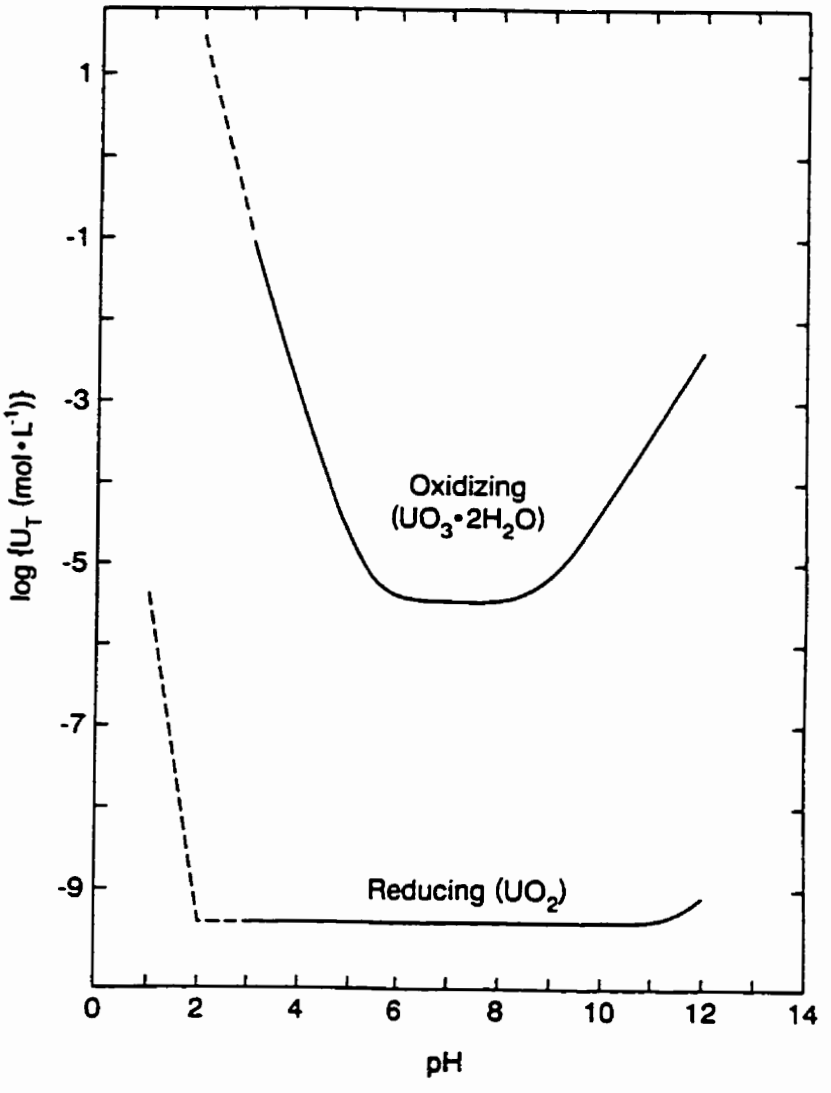

FIGURE 2.6A: Solubilities of UO_2 and $UO_3.2H_2O$ as a function of pH at 25°C [16].

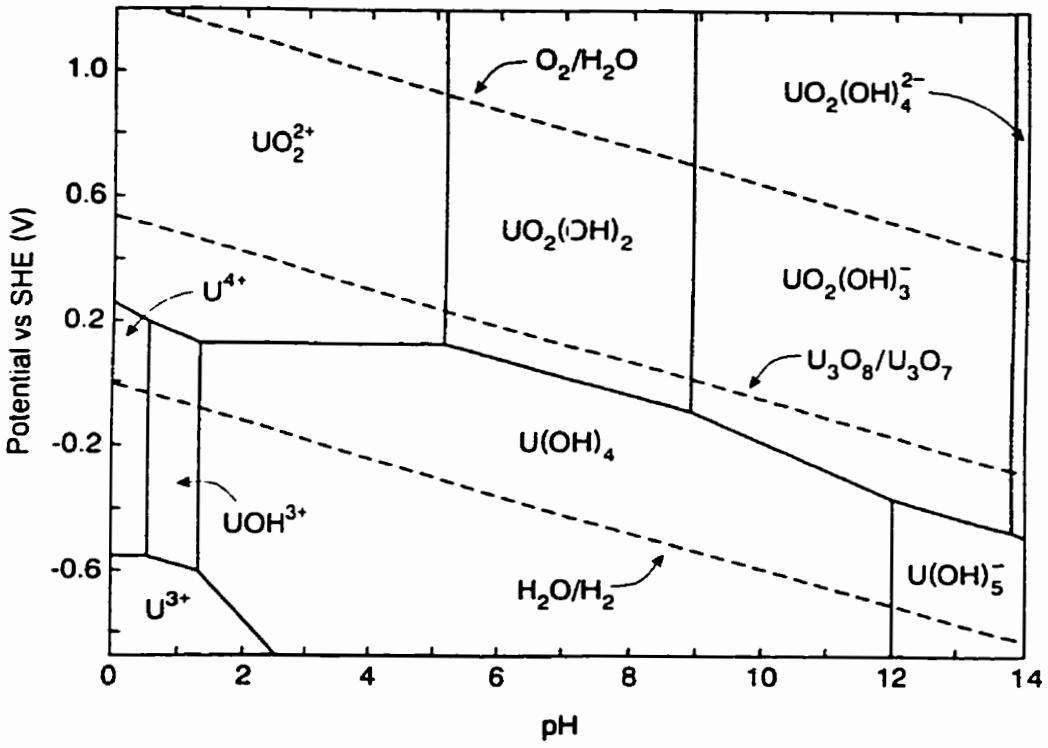

FIGURE 2.6B: Predominant soluble U species in water as a function of potential and pH at a uranium concentration of 10^{-6} mol.L^{-1} [16].

2.4.2 Reaction Scheme for UO_2 Dissolution

Figure 2.7 [12] shows the reaction scheme proposed for the oxidation and dissolution of UO_2 in neutral and alkaline solutions, when strongly complexing anions are not present. This mechanism of the oxidation and dissolution of UO_2 was determined by a combination of electrochemical and X-ray photoelectron spectroscopy (XPS) methods [23, 61, 62, 63, 64,64].

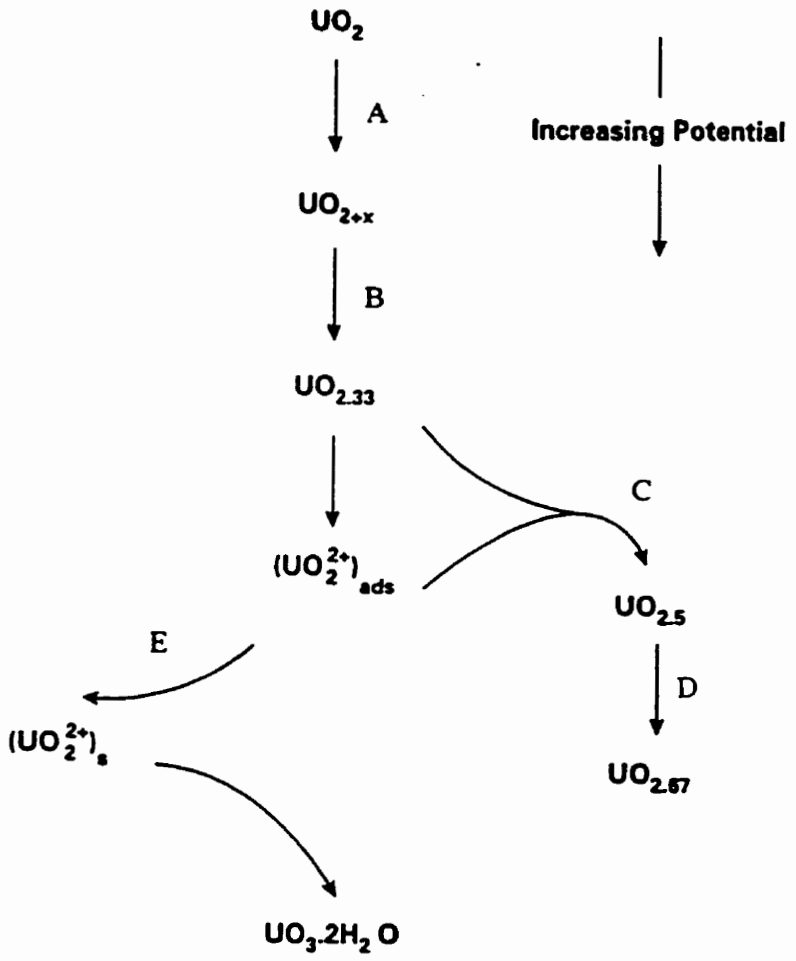

FIGURE 2.7: Reaction scheme for the anodic dissolution of UO_2 in neutral to alkaline solutions ($5 \leq pH \leq 10.5$).

2.4.3 Surface Composition under Cyclic Voltammetric Conditions

The behaviour of UO_2 as a function of redox conditions has been determined using a combination of electrochemical and surface analytical techniques [2, 13, 14, 16-24, 62, 63, 64, 64, 66]. This behaviour can be

conveniently presented by considering the stages of oxidation and reduction exhibited in a cyclic voltammogram. In a cyclic voltammogram, the potential is scanned from a relatively negative potential, at which the electrode is unoxidized, to a positive limit (the anodic limit) and then back again. During the positive scan, oxidation of the electrode is observed as a positive current which varies with potential. Oxidation leads to the formation of surface films, generally observed as current peaks, and dissolution. Subsequently, on the reverse scan, the surface films formed during oxidation, providing they are reducible, appear as reduction peaks in the cyclic voltammogram. Dissolved material will be transported to the bulk solution. Figure 2.8 is a cyclic voltammogram showing the oxidation and reduction peaks obtained on a UO_2 rotating disk electrode (RDE) in neutral to slightly alkaline solutions.

Peak I in Figure 2.8 occurs in the potential range of -0.8 to -0.4 V (vs. SCE). At these low potentials, oxidation should not be thermodynamically feasible (Figure 2.6B). The surface oxidation is reversible with 100% charge recovery on the reverse voltammetric scan. This is consistent with photothermal deflection spectroscopic measurements which show that dissolution is not observed until potentials $\geq$ -0.3 V are achieved [16]. From the above evidence, peak I can be attributed to the formation of a film in which only a few monolayers, or specific areas of the surface, are oxidized. These areas are possibly in the grain boundaries where enhanced hyperstoichiometry could exist due to the fuel fabrication process (Figure 2.1).

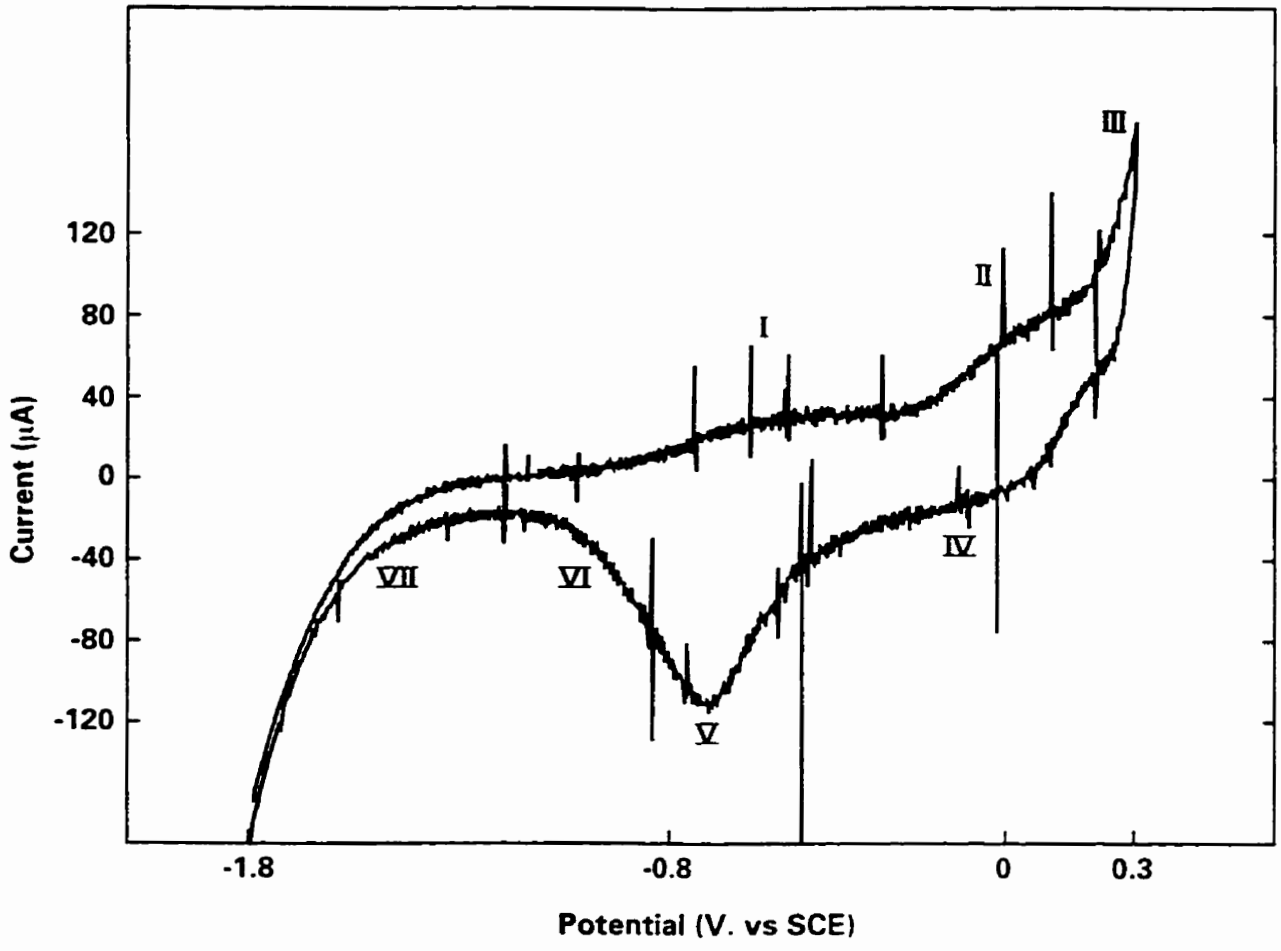

FIGURE 2.8: Cyclic voltammogram recorded on a rotating disc electrode at 10 $mV.s^{-1}$ at a rotation rate 1000 rpm using IR compensation in 0.1 $mol.L^{-1}$ $NaClO_4$ at pH 9.5.

Peak II (Figure 2.8) is attributed to the oxidation of the UO_2 electrode matrix (reaction A in Figure 2.7) involving the incorporation of O^{2-} ions at the interstitial sites in the fluorite lattice until a stoichiometry close to $UO_{2.33}$ (U_3O_7) is reached (Figure 2.4) [16]. The oxidation is irreversible beyond ~-0.4 V as

indicated by the loss of a photocurrent signal after scanning into this potential region and by XPS analysis of the electrode surface after subsequent cathodic reduction [16, 24, 61]. Also, as the potential goes more positive than -0.4 V, the surface film thickens as determined by the increase in the charge associated with the cathodic reduction, peak V (discussed below). Further evidence can be seen in a logarithmic current (i) - time plot recorded at a constant potential, E > -0.4 V, where the current for film growth is a linear function of time, with a slope ~-1, consistent with growth via a high-field ion conduction process [62].

A composition of $UO_{2.33}$ is the end of the fluorite structure range (Section 2.3.3), and further oxidation involves the oxidative dissolution of this layer as uranyl ions and/or its recrystallization into $UO_{2.5}/UO_{2.67}$, region III, Figure 2.8. The film thickens at a very slow rate with most of the anodic charge going to dissolution. The uranyl ion (UO_2^{2+}) appears to be the common intermediate required for the formation of $UO_{2.5}$ and $UO_{2.67}$ [24, 61]. Recrystallization to yield $UO_{2.5}/UO_{2.67}$ appears favoured at potentials ≥ +0.35 V vs SCE, where the adsorbed intermediate coverage by $(UO_2^{2+})_{ads}$ on the UO_2 surface will be high. However, more recent studies [63] have shown the formation of the secondary precipitate $UO_3.2H_2O$ subsequent to dissolution is more likely in low temperature aqueous conditions. This will be discussed in more detail in Section 2.4.4 below.

Peak IV (Figure 2.8) is a current due to the reduction of an easily reduced species and is observed at potentials as positive as -0.2 V. There is only a small amount of charge associated with this peak, suggesting the oxidized species is

present either as a monolayer or at a small number of discrete sites on the electrode surface. It is possible peak IV is the reduction of the adsorbed UO_2^{2+} species which can act as a precursor to either the formation of oxide films or dissolved uranyl species [63]. However, its chemical identity is still unknown.

Peak V (Figure 2.8) is attributed to the reduction of $UO_{2.33}$ to UO_{2+x}. A layer of this oxide remains on the electrode surface even after steady state anodic dissolution at potentials more positive than 0.35 V [63, 67].

Peak VI (present only as a shoulder in Figure 2.8) is attributed to the reduction of either $UO_{2.5}/UO_{2.67}$ or $UO_3.2H_2O$ to UO_{2+x} [63]. Since the formation of $UO_3.2H_2O$ is thought to be more likely than that of $UO_{2.5}/UO_{2.67}$, the second process is more likely. The size of this peak increases as the potential on the forward scan becomes more positive, or when the potential is held at a constant potential for long times, but is not observed on the cathodic scan after a period of oxidation at high potentials ($E \geq 0.35$ V) [63]. The $UO_3.2H_2O$ layer has insulating properties and thus would be expected to block the dissolution of UO_2 [63]. Previous experiments suggested that the $UO_3.2H_2O$ was located at grain boundaries [65]. Reduction at Peak VI will be discussed further in the anodic dissolution section 2.4.4.

Area VII (Figure 2.8) is the reduction of water leading to the evolution of hydrogen [25].

2.4.4 Anodic Dissolution of UO_2 under Potentiostatic Conditions

While the stages of oxidation / reduction as a function of potential are clearly portrayed under voltammetric conditions, oxidation under controlled potential conditions yields a more meaningful description of the behaviour to be expected as redox conditions change. Sunder et al. [63] have shown that the anodic oxidation and dissolution of UO_2 in neutral to slightly alkaline solutions can be separated into two regions for potentials ≥ 0.1 V (vs. SCE).

The first region covers the potential range from 0.1 to 0.35 V in which the anodic oxidation of the UO_2 surface leads to coverage by oxidized films which block further oxidation. Initially, the surface becomes covered by a 5 to 8 nm layer of composition $UO_{2.33}$ followed by a second film of composition $UO_{2.67}$, or more likely $UO_3.2H_2O$, which is thought to be located predominantly at grain boundaries.

The second region occurs at potentials ≥ 0.35 V where the UO_2 surface reaches steady state dissolution conditions and the dissolution currents follow a Tafel relationship. Also, dissolution seems to be occurring locally, most probably in the grain boundaries.

Previously, the composition of the second film formed in the potential range from 0.1 to 0.35 V, and subsequently reduced at peak VI in a cathodic stripping voltammogram, was thought to be $UO_{2.5}/UO_{2.67}$. However, Sunder et al. [63] have shown that the second film possesses insulating properties and its dissolution requires an overpotential > 0.55 V. Consequently, a more likely

possibility is that the reduction at peak VI is due to the reduction of a $UO_3.2H_2O$ layer, a fully oxidized phase which does possess insulating properties.

Sunder et al. [63] concluded that the insulating layer was too thin (20 to 30 nm) to be universally present across the electrode surface since its formation by a solution mediated recrystallization would be expected to produce a porous layer that would have to grow much thicker to block the surface oxidation. Also, the layer does not appear to be uniform over the electrode surface since the current was not dependent on the rotation rate of the electrode. Hence, $UO_3.2H_2O$ was thought to be located at occluded sites, possible grain boundaries, where its formation and removal would depend on the local chemistry in these sites. Further evidence is required to conclude unequivocally that dissolution occurs predominantly in the grain boundaries.

2.4.5 Proposed Mechanism for the Oxidative Dissolution of UO_2

Based on the above evidence, a more detailed mechanism for the electrochemical oxidation / dissolution of UO_2 can be given. A layer close in stoichiometry to $UO_{2.33}$ has been shown to form by the oxidation of the UO_2 lattice [63],

$$UO_2 + 0.33H_2O \rightarrow UO_{2.33} + 0.66H^+ + 0.66e \qquad (2.1)$$

The oxidation of the $UO_{2.33}$ layer to form an intermediate U^{VI} species can be represented by the reaction,

$$UO_{2.33} + 0.33H^+ \rightarrow (UO_2^{2+})_{ads} + 0.33OH^- + 1.34e \qquad (2.2)$$

The adsorbed intermediate UO_2^{2+} species may dissolve or be incorporated into oxidized surface phases,

$$3UO_{2.33} + 3(UO_2^{2+})_{ads} + 3H_2O \rightarrow 6UO_{2.67} + 6H^+ \quad (2.3)$$

$$(UO_2^{2+})_{ads} + 3H_2O \rightarrow UO_3.2H_2O + 2H^+ \quad (2.4)$$

in which reaction 2.4 is thought to be kinetically more favorable. At potentials ($E < 0.35$ V) where film growth predominates, the acidity produced in reactions 2.3 and 2.4 occurs locally but does not appear able to increase the solubility of U^{VI} species sufficiently to prevent the precipitation of $UO_3.2H_2O$ which blocks reaction 2.2. At high potentials ($E > 0.35$ V), in the steady state region, the uranyl ion production is rapid and dissolution is extensive. The fast hydrolysis of the uranyl ions produces local acidity,

$$2UO_2^{2+} + 2H_2O \rightarrow (UO_2)_2(OH)_2^{2+} + 2H^+ \quad (2.5)$$

$$3UO_2^{2+} + 5H_2O \rightarrow (UO_2)_3(OH)_5^{+} + 5H^+ \quad (2.6)$$

which either prevents the precipitation of $UO_3.2H_2O$ (reaction 2.4) or leads to chemical dissolution of oxidized phases formed at lower potentials,

$$UO_3.2H_2O + 2H^+ \rightarrow UO_2^{2+} + 3H_2O \quad (2.7).$$

2.4.6 Groundwater Composition

The dissolution of UO_2 will be influenced by pH, complexing anions and species that cause secondary phase formations [12].

2.4.6.1 pH

For pH < 5, the solubility of U^{VI} increases markedly, Figure 2.6A, and $UO_{2.33}$, $UO_{2.5}$, $UO_{2.67}$ and $UO_3.2H_2O$ film formation does not occur [15]. Therefore, reaction E is favored over reactions C and D in the reaction mechanism (Figure 2.7). A surface film of undetermined composition is formed, but does not appear to significantly affect oxidative dissolution.

The behaviour in neutral to alkaline solution (pH ≥ 5) has been discussed in detail above. A surface film of $UO_{2.33}$ forms followed by its oxidative dissolution. This film reaches a steady state thickness (~6 nm) under natural aqueous corrosion conditions (as opposed to electrochemical conditions) in 5 to 10 hours and the thickness increases as the pH increases. Further oxidation to a hydrated form of UO_3 then occurs until steady state dissolution conditions are achieved [13, 15].

The behaviour in alkaline solutions (12 ≥ pH >10) at potentials between -0.3 and +0.2 V showed that the thickness of the surface film formed at peak I increased with increasing pH and potential. At an applied electrochemical potential of 0.1 V and at short times (t < 1 minute), the surface composition changed with time. For 1 < t < 10 minutes, a film of composition U_2O_5 formed which transformed to U_3O_8 ($UO_{2.67}$) at t > 10 minutes. Dissolution as UO_2^{2+} started once a layer of U_2O_5 was formed. At pH = 12 a partially passivating UO_3 layer was formed [65].

From the Waste Management viewpoint, the behaviour in the pH range 5

to 10 is of greatest significance since the pH of the groundwaters anticipated in the waste disposal area, is expected to be in this range [68].

2.4.6.2 Groundwater Species

Groundwater analyses show the important species to consider are the anions Cl^-, SO_4^{2-}, $H_2PO_4^-$, HCO_3^-/CO_3^{2-} and F^-; the cations Na^+, K^+ and Ca^{2+}; and dissolved silica [12].

The uranyl ion will preferentially complex with carbonate and phosphate over the neutral to alkaline pH range [16]. At sufficiently high concentrations, phosphate will form insoluble uranyl phosphates. Sulphate and fluoride will also complex the uranyl ion, but much less favorably except at low pH and high concentrations. For the U^{4+} ion, the opposite trend is observed in which the carbonate will not complex with U^{4+}, but sulphate and especially fluoride will. Consequently, the groundwater anions have an effect on increasing the difference in solubility between U^{VI} and U^{IV} over the neutral to alkaline pH range [3, 4, 12, 13, 16]. From the Waste Management viewpoint, the groundwaters expected in the Canadian Shield should not be complexing, and only carbonate appears capable of exerting any significant influence on the fuel dissolution process [60].

Nicol and Needes [68] showed that sulphate does accelerate the anodic dissolution of UO_2 at pH values between 2 and 5, but has no effect in neutral solutions. Shoesmith and Bailey [69] found a similar effect for F^-. For Cl^-, no complexing effect was observed for concentrations up to 0.5 $mol.L^{-1}$ in the pH

range 5 to 11 [12].

Sunder et al. [70] observed that both carbonate and phosphate accelerate the anodic dissolution of UO_2 in neutral to alkaline solutions. Figure 2.9 summarizes the reaction steps involved for dissolution in carbonate and phosphate.

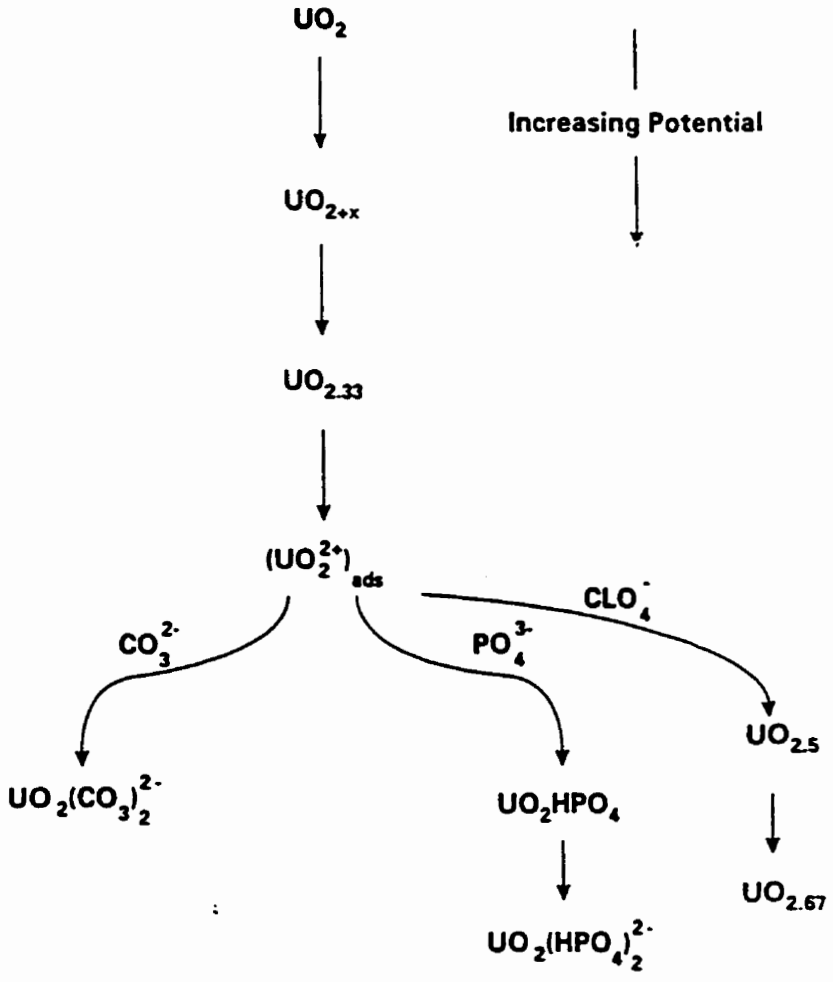

FIGURE 2.9: Reaction scheme for the anodic dissolution of UO_2 in carbonate and phosphate solutions.

The early stages of oxidation, up to $UO_{2.33}$, appear not to be affected between pH 5 and 11. However, the subsequent dissolution reaction is favored over the subsequent film formation processes for carbonate concentrations $\geq 10^{-3}$ mol.L^{-1} and phosphate concentration $\geq 10^{-1}$ mol.L^{-1} [12].

The acceleration of dissolution in carbonate solutions is due partly to a thermodynamic effect and partly to a kinetic effect. Thermodynamically, the dissolution product, UO_2^{2+}, is stabilized by complexation with the carbonate anion. The complexation equilibria, at zero ionic strength and 25°C [71], are:

$$UO_2^{2+} + CO_3^{2-} \rightarrow UO_2CO_3(aq) \qquad \log K_1 = 9.5 \pm 0.4 \qquad (2.8)$$

$$UO_2^{2+} + 2CO_3^{2-} \rightarrow UO_2(CO_3)_2^{2-} \qquad \log \beta_2 = 16.6 \pm 0.3 \qquad (2.9)$$

$$UO_2^{2+} + 3CO_3^{2-} \rightarrow UO_2(CO_3)_3^{4-} \qquad \log \beta_3 = 21.6 \pm 0.6 \qquad (2.10)$$

where K_1 is a stepwise formation constant and β_n is an overall formation constant for the reaction, in which n corresponds to the number of moles of complexing species that combine with one mole of cation. The complexation of the uranyl ion with carbonate favors dissolution by shifting the equilibrium potential of the anodic dissolution half reaction (reaction 1.1) to more negative potentials. A kinetic influence has been demonstrated by ac impedance experiments. For sufficiently high concentrations, carbonate accelerates the rate of oxidative dissolution [72] by the formation of surface complexes such as UO_2CO_3. At low anodic potentials and at the natural corrosion potential of UO_2, dissolution of UO_2 will occur at a faster rate than the formation of surface complexes such as UO_2CO_3. Hence, the thermodynamic influence (i.e. dissolution) dominates over the kinetic influence (i.e. UO_2CO_3).

For sulphate ions, the acceleration of UO_2 dissolution is minor compared to carbonate since a less stable complex with UO_2^{2+} is formed [3],

$$UO_2^{2+} + SO_4^{2-} \rightarrow UO_2SO_4\,(aq) \qquad \log K_1 = 2.9 \pm 0.5 \qquad (2.11)$$

The effect of phosphate anions on UO_2 dissolution is more involved. Complexation of phosphate with uranyl ions increases the dissolution rate under moderately oxidizing conditions ($E < 0.3V$) [6, 12],

$$UO_2^{2+} + HPO_4^{2-} \rightarrow UO_2HPO_4(aq) \qquad \log K_1 = 8 \pm 2 \qquad (2.12)$$

$$UO_2^{2+} + 2HPO_4^{2-} \rightarrow UO_2(HPO_4)_2^{2-} \qquad \log \beta_2 = 17.5 \pm 2 \qquad (2.13)$$

When strongly oxidizing conditions ($E \geq 0.3V$) are present, phosphate forms an insoluble surface layer of uranyl phosphate whose chemical dissolution rate limits the overall reaction [3, 12],

$$(UO_2)_3(PO_4)_2 + 2H^+ \rightarrow 2UO_2^{2+} + 2HPO_4^{2-} \qquad \log K_1 = -24 \pm 3 \qquad (2.14)$$

$$(UO_2)_2(HPO_4)_2 \rightarrow 2UO_2^{2+} + 2HPO_4^{2-} \qquad \log K_1 = -23 \pm 2 \qquad (2.15)$$

Impedance experiments show that phosphate ions are directly involved in the formation of an adsorbed intermediate, but the mechanism is still unclear.

Cations present in the groundwater do not affect the dissolution rate of UO_2 directly, but may affect the stability and rate of formation of secondary phases formed subsequent to dissolution. The formation of secondary phases on the surface of UO_2 may accelerate or inhibit dissolution. If the dissolution reaction is close to equilibrium (ie. the surface concentration of dissolved uranium is close to the solubility of the phase on the surface of UO_2) the dissolution rate could increase [13]. At present there is no experimental evidence to support this. A more likely process would be for the secondary

phase (e.g. $UO_3.2H_2O$) to inhibit the dissolution rate of UO_2. The phase will act as a semi-impermeable layer for oxidant transport to, or dissolved uranium transport away from, the UO_2 surface [13].

After long exposure to groundwaters containing Ca^{2+} and SiO_4^{4-}, precipitated secondary phases should form by a mineral paragenetic sequence [11]. Figure 2.10 [11] shows the sequence observed for natural uranium deposits in which the UO_2 surface is initially altered to UOH minerals (e.g. schoepite), followed by the formation of soddyite and finally alkali and alkaline earth-bearing uranyl silicates [11].

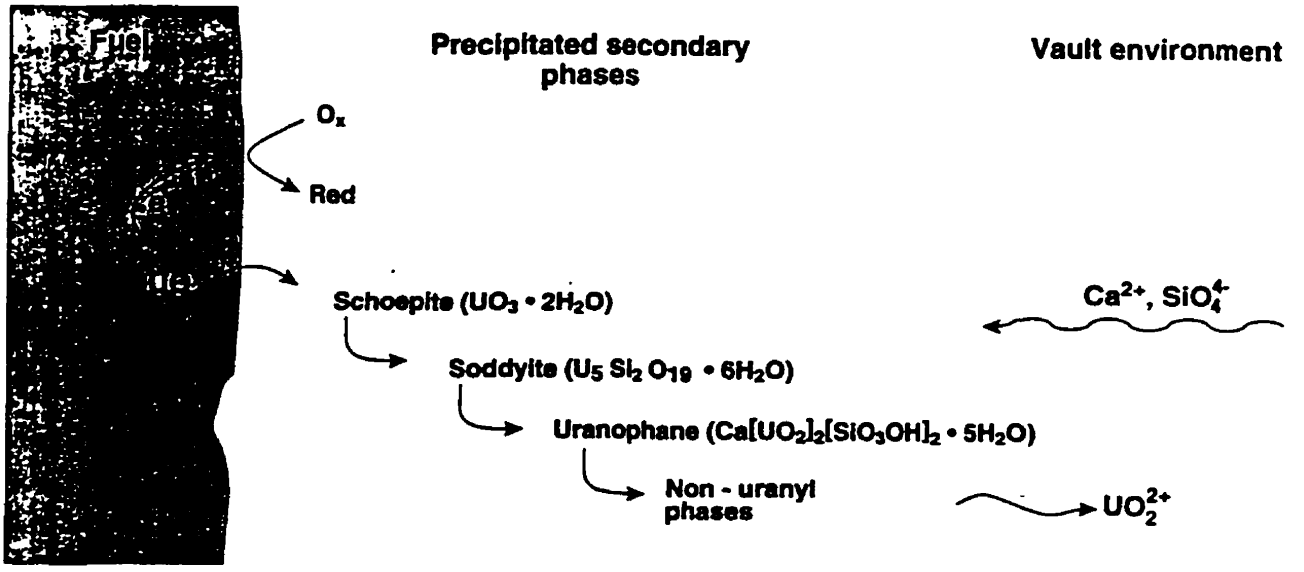

FIGURE 2.10: Reaction sequence showing the alteration of precipitated uranyl phases derived for natural uranium deposits [11].

These precipitated phases are very insoluble and would be expected to eventually block dissolution by suppressing the oxidation of UO_2.

2.5 OPEN CIRCUIT CORROSION BEHAVIOUR OF UO_2

While this thesis will concentrate on the anodic dissolution of UO_2, it is the behaviour of UO_2 under natural corrosion conditions which must be interpreted if fuel behaviour under disposal conditions is to be predicted.

Figure 2.11 [73] is a summary of the corrosion behaviour of UO_2 in aerated neutral to alkaline solutions which illustrates the stages of oxidation observed on an initially unoxidized UO_2 surface as the corrosion potential (E_{corr}) changes with time and approaches a steady state value of $(E_{corr})_{ss}$.

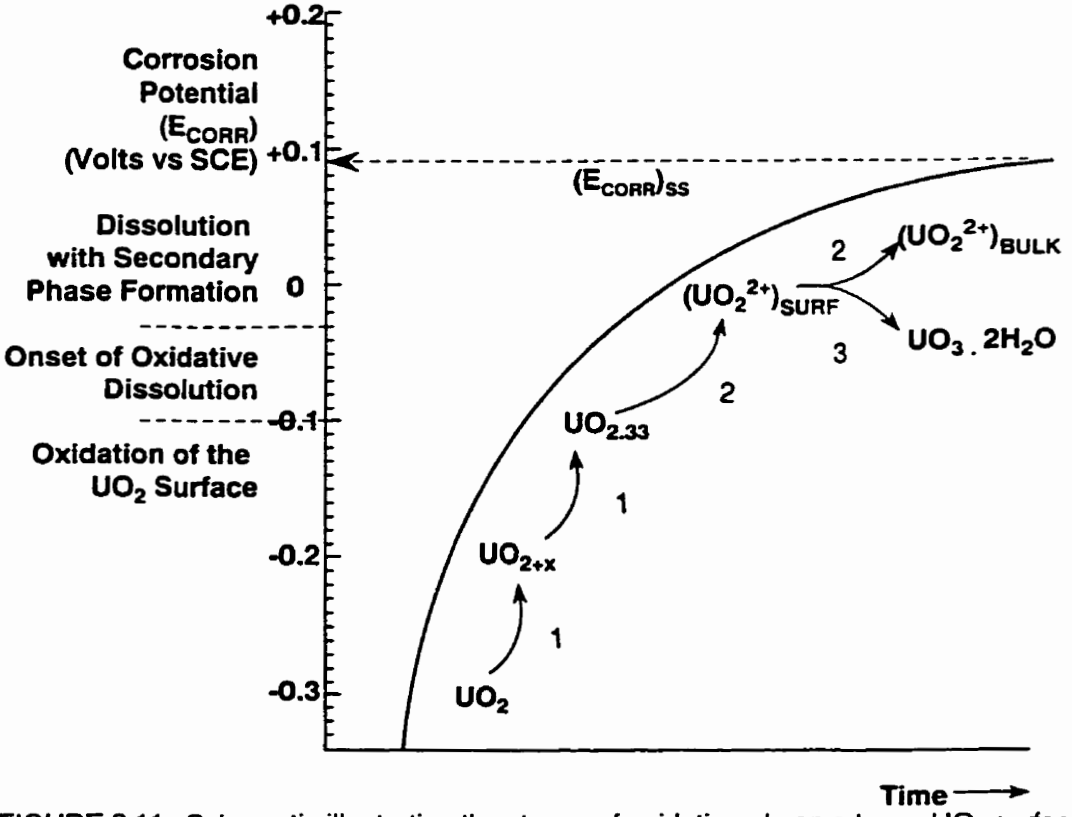

FIGURE 2.11: Schematic illustrating the stages of oxidation observed on a UO_2 surface as the corrosion potential (E_{corr}) changes with time and approaches steady-state ($(E_{corr})_{ss}$) [73].

The results of voltammetric and XPS measurements enable us to interpret the composition of the UO_2 surface as E_{corr} approaches a steady state value of ~0.05 to 0.10 V. This steady state potential varies with the type and concentration of oxidant. For fuel disposal conditions we are primarily interested in dissolved O_2 and those oxidants (H_2O_2, $OH^{\cdot}$, etc.) likely to be produced by the radiolytic decomposition of H_2O [25, 73-76].

Over potential region 1 in Figure 2.11 ($E_{corr} \leq$ -0.1 V), the extent of oxidation of the UO_2 surface increases as E_{corr} increases [24, 77]. Electrochemical and XPS experiments have shown that the oxidized surface layer increases in thickness and/or changes composition in this potential range until a composition close to $UO_{2.33}$ is achieved around -0.1 V [77]. The rate of this surface oxidation can be roughly estimated from the time required for E_{corr} to reach this value.

In potential region 2, oxidative dissolution of this oxidized surface film as UO_2^{2+} occurs. It should be noted that recent experiments using photothermal deflection spectroscopy [22] have indicated that dissolution can occur at potentials as low as -0.3 V, before the $UO_{2.33}$ layer reaches a steady state thickness. Once $(E_{corr})_{ss}$ is reached, the rate of $UO_{2.33}$ film formation is equal to the rate of its oxidative dissolution as UO_2^{2+}, and a steady state condition is achieved [73].

Region 3 is the potential range in which local supersaturation occurs and secondary phases (e.g. $UO_3.2H_2O$) accumulate on the dissolving electrode

surface. XPS has shown that this occurs as the dissolution rate increases for $E_{corr} > 0$ V [78, 79].

2.6 EFFECTS OF VARIOUS OXIDANTS

The oxidants and reductants formed during the radiolysis of water are shown in Figure 2.12 [13].

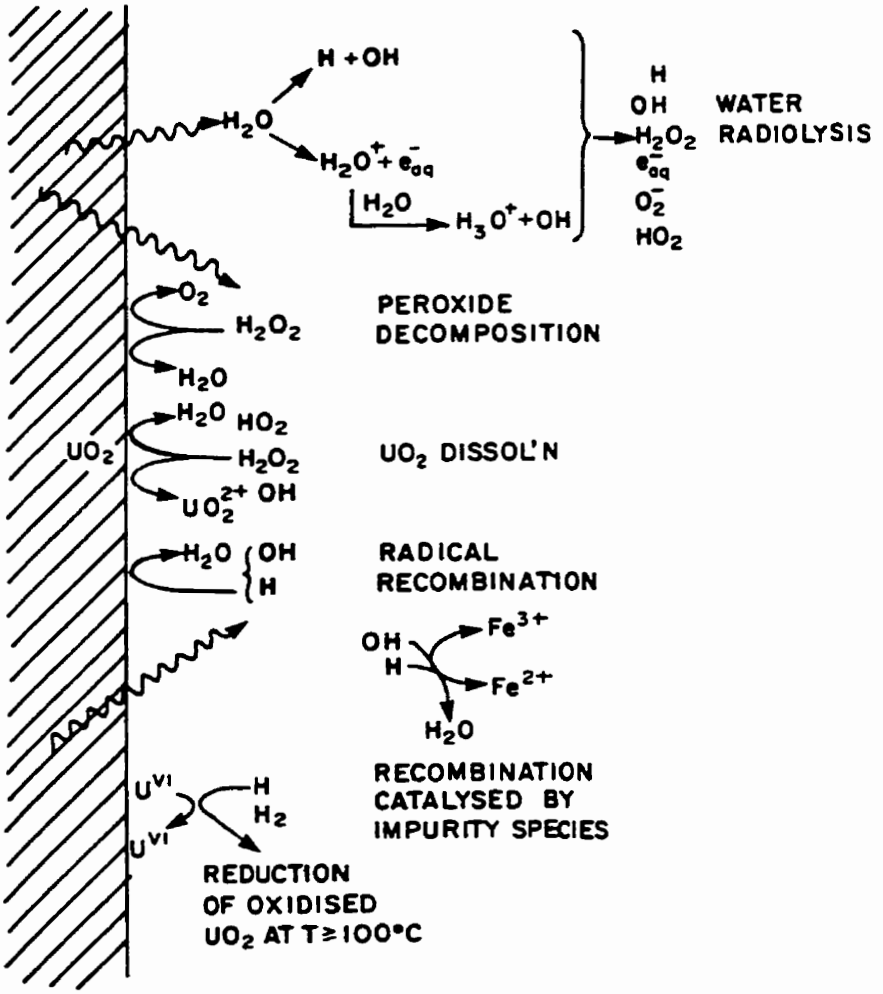

FIGURE 2.12: Schematic representation of oxidants and reductants formed during radiolysis, their interrelationships, and their influence on UO_2 oxidative dissolution [13].

Electrochemical methods have been used to determine how oxygen and the products of water radiolysis affect the oxidation and dissolution of UO_2. The direct effects of alpha and gamma radiolysis of water have also been studied [15, 21, 64, 78, 80, 81]. Here, the specific effects of various oxidants are briefly reviewed. Fuller descriptions have been published elsewhere [15, 21, 64, 78, 80, 81].

2.6.1 Oxygen Reduction

Reduction of dissolved oxygen on the UO_2 surface is a very slow reaction because of the necessity to break the strong O-O bond. From corrosion potential experiments, the steady state potential, $(E_{corr})_{ss}$, depends on the concentration of dissolved oxygen present. The $(E_{corr})_{ss}$ values fall within the range +0.1 V and -0.24 V for aerated and argon purged solutions, respectively [81].

2.6.2 Hydrogen Peroxide

In solutions containing H_2O_2, the oxidation of UO_2 is much more rapid than in the presence of oxygen [81]. However, the behaviour is complicated by the simultaneous decomposition of H_2O_2 which can also be considered an electrochemical coupling of an anodic and cathodic reaction as shown in the equations below,

$$H_2O_2 \rightarrow O_2 + 2H^+ + 2e \qquad (2.16)$$

$$H_2O_2 + 2e \rightarrow 2OH^- \qquad (2.17)$$

The significance of this decomposition process in determining the value of E_{corr} is still being investigated. The range of E_{corr} values in solutions containing H_2O_2 concentrations from 10^{-4} to 10^{-1} mol.L^{-1} is between ~0.07 V and 0.1 V. For H_2O_2 concentrations > 10^{-1} mol.L^{-1}, E_{corr} values as high as 0.25 V have been achieved suggesting enhanced oxidative dissolution of UO_2 at these high concentrations [81].

2.6.3 Gamma Radiolysis

The radical species produced by gamma radiolysis ($OH^{\cdot}$, O_2^{-}) are extremely reactive and rapidly oxidize UO_2. The oxidation of UO_2 in the presence of $OH^{\cdot}$ and O_2^{-} occurs in two stages. The first stage occurs in the potential range from -0.5 V to -0.1 V (vs. SCE) and involves the formation of a thin film of UO_{2+x}, which is close to a composition of $UO_{2.33}$. The second stage eventually reaches a steady state at a value of E_{corr}, which is dependent on the gamma dose rate. It involves the oxidative dissolution of the film as soluble U^{VI} species and the formation of secondary phases (i.e. probably $UO_3.2H_2O$) [78]. However, for waste disposal, the oxidative dissolution of UO_2 due to γ-radiolysis is only important for ~200 years. Since the container is expected to survive this period, γ-radiolysis will be of little concern in the fuel dissolution process.

2.6.4 Alpha Radiolysis

E_{corr} values were found to be dependent on the alpha source strength, but even for the highest source strength tested (400 μCi), E_{corr} does not exceed the values obtained in H_2O_2 solutions. This is consistent with the predominant formation of molecular radiolysis products (e.g. H_2O_2) by water radiolysis due to the absorption of high linear energy transfer radiation (alpha) [81].

2.7 PHYSICAL FACTORS

As well as the chemical factors discussed above, physical factors can also affect the dissolution rate of UO_2, although little is known about the influence of physical factors such as grain size, crystallinity, surface area and solid state defects [12].

Both the measurements of Nel [82], and the electrochemical results of Nicol and Needes [19] showed that the dissolution rate decreased as the number of defects in the structure of UO_2 decreased. Nicol and Needes used five different samples consisting of single crystals ($UO_{2.03}$) to sintered pellets ($UO_{2.01}$) and fused polycrystalline material ($UO_{2.10}$ to $UO_{2.14}$). They found that the sintered pellets were 20 to 50 times more reactive than the single crystals. The explanation offered was that the single crystals had no grain boundaries and defects, and were therefore less reactive. By contrast, the sintered pellets were made up of small crystallites having a high surface area and a higher number of reactive sites (ie. grain boundaries) leading to an increased reactivity. No

correlation between the dissolution rate and the oxygen:uranium ratio was found. Enhanced reactivity at the grain boundaries was also observed by Johnson et al. [83]. Their electrochemical experiments found extensive grain boundary etching concentrated around the edges of the UO_2 electrode. This indicated a higher reactivity at the edges, which are known to have a higher number of defects and reactive sites.

Based on these results, the dissolution rate will increase as the number of defects increases or the particle size decreases, due to an increase in the number of active sites at the surface of UO_2. In-reactor irradiation of UO_2 generally increases the number of defects, and care must be taken when using dissolution rates measured on unirradiated UO_2 to interpret the behaviour of used fuel. However, the general chemical mechanism for the dissolution of UO_2 should not change.

The semiconducting properties of UO_2 may also affect the reactivity [46]. The mechanism and kinetics of the cathodic reactions which drive the oxidative dissolution change as the surface composition and semiconducting character of the oxide change.

2.8 ELECTROCHEMICAL MODEL FOR THE OXIDATIVE DISSOLUTION OF UO_2

The understanding of UO_2 dissolution described above has been used to formulate a simple model for oxidizing conditions to predict fuel dissolution and radionuclide release rates under waste disposal conditions.

In this model the rates are predicted as a function of the redox conditions by extrapolating steady state electrochemical currents for the anodic dissolution of UO_2 to the corrosion potential measured in various groundwaters. This procedure is illustrated schematically in Figure 2.13 [84] in which the corrosion currents are converted to corrosion rates by the application of Faraday's law.

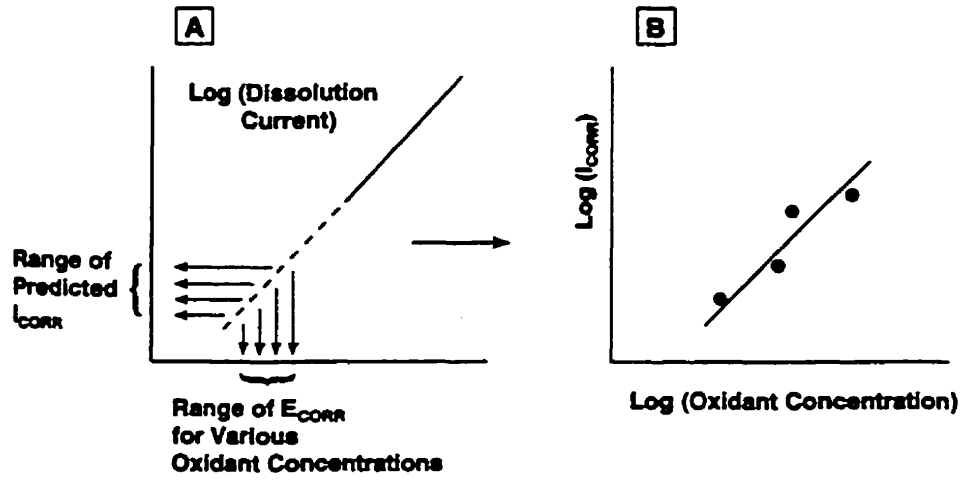

FIGURE 2.13: Graphical illustration of procedure used to obtain values of corrosion current ($I_{corr} \equiv$ corrosion rate) for the corrosion of UO_2. (A) Tafel plot of the anodic dissolution currents as a function of applied potentials. The dashed lines illustrates the extrapolation of the measured currents to the measured corrosion potential (E_{corr}) to obtain corrosion current (I_{corr}) values. (B) Corrosion currents as a function of oxidant concentration [84].

3.0 EXPERIMENTAL

3.1 UO_2 ELECTRODES

3.1.1 Source and Preparation of UO_2

The UO_2 electrodes were constructed from discs of sintered polycrystalline UO_2 cut from unirradiated CANDU fuel pellets. All the UO_2 electrodes were prepared the same way. A 2 to 3 mm slice from a UO_2 pellet was coated on one side with a thin layer of copper metal by electrodeposition [74]. The copper side of the slice was bonded to a stainless steel post with a high conductivity silver epoxy (HYSOL KE4238, HD3475). The UO_2 / stainless steel unit was placed into a machined lucite shell and the gap filled with a non-conductive epoxy (HYSOL RE2038, HD3404) to seal the electrode. The electrodes were polished using wet silicon carbide paper (18 μm finish) followed by washing with distilled deionized water. The stainless steel post of the electrode unit was threaded and screwed onto the rotating electrode shaft. The shaft was attached to the rotator and the electrode was lowered into the solution until there was an airtight seal between the shaft and the electrochemical cell. The airtight seal is achieved with a bearing packed collar around the electrode shaft. The lead was hooked up to the working electrode to create an electrical connection to the potentiostat used to control its potential.

3.1.2 Designation of electrodes used

The electrodes studied were designated L6, ZR1, ZR2, ZR3, L210, 1B2, J1 and J2 according to their source. Their resistance values were measured electrochemically in 0.1 mol.L^{-1} $NaClO_4$ using the current interrupt method, discussed below, and are shown in Table 3.1.

TABLE 3.1

Electrode Resistance Values

Electrode	Resistance (ohms)
L6	433
J2	409
ZR1	348
ZR2	387
ZR3	390
J1	455

The ZR1, ZR2 and ZR3 electrodes were made from the same UO_2 pellet with ZR3 reserved for XPS experiments. The J1 and J2 electrodes were also made from a common UO_2 pellet. A small decrease in resistance occurred as a number of experiments were performed on each electrode. This decrease was found to exert an insignificant effect since repeat cyclic voltammograms (CV's) were almost identical. CV's were performed on repolished electrodes after each experiment to ensure the electrode had not changed its properties and was still functional. The L6, ZR1 and ZR2 electrodes were used interchangeably for the majority of experiments because their resistance values and CV's were all similar.

A scanning electron photomicrograph (SEM) of a freshly prepared UO_2 electrode is shown in Figure 3.1. From the SEM figure it can be observed that the size of the grains is between 3 and 15 μm.

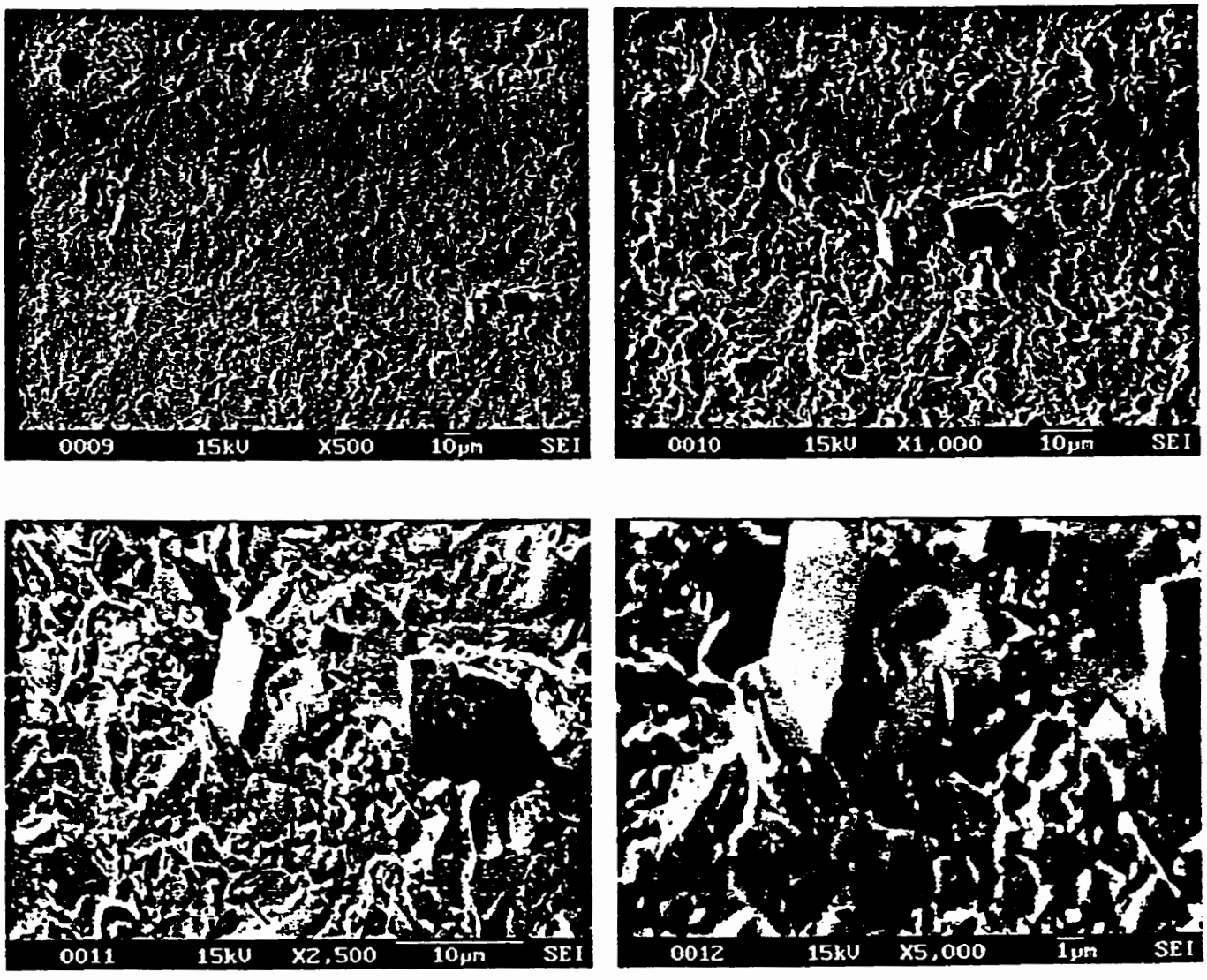

FIGURE 3.1: SEM photomicrographs of a freshly prepared UO_2 electrode at magnifications of (A) 500X, (B) 1000x, (C) 2500X and (D) 5000X.

3.2 ELECTROCHEMICAL CELL AND EQUIPMENT

All electrochemical experiments were performed in a standard three-electrode-three compartment glass cell (Figure 3.2).

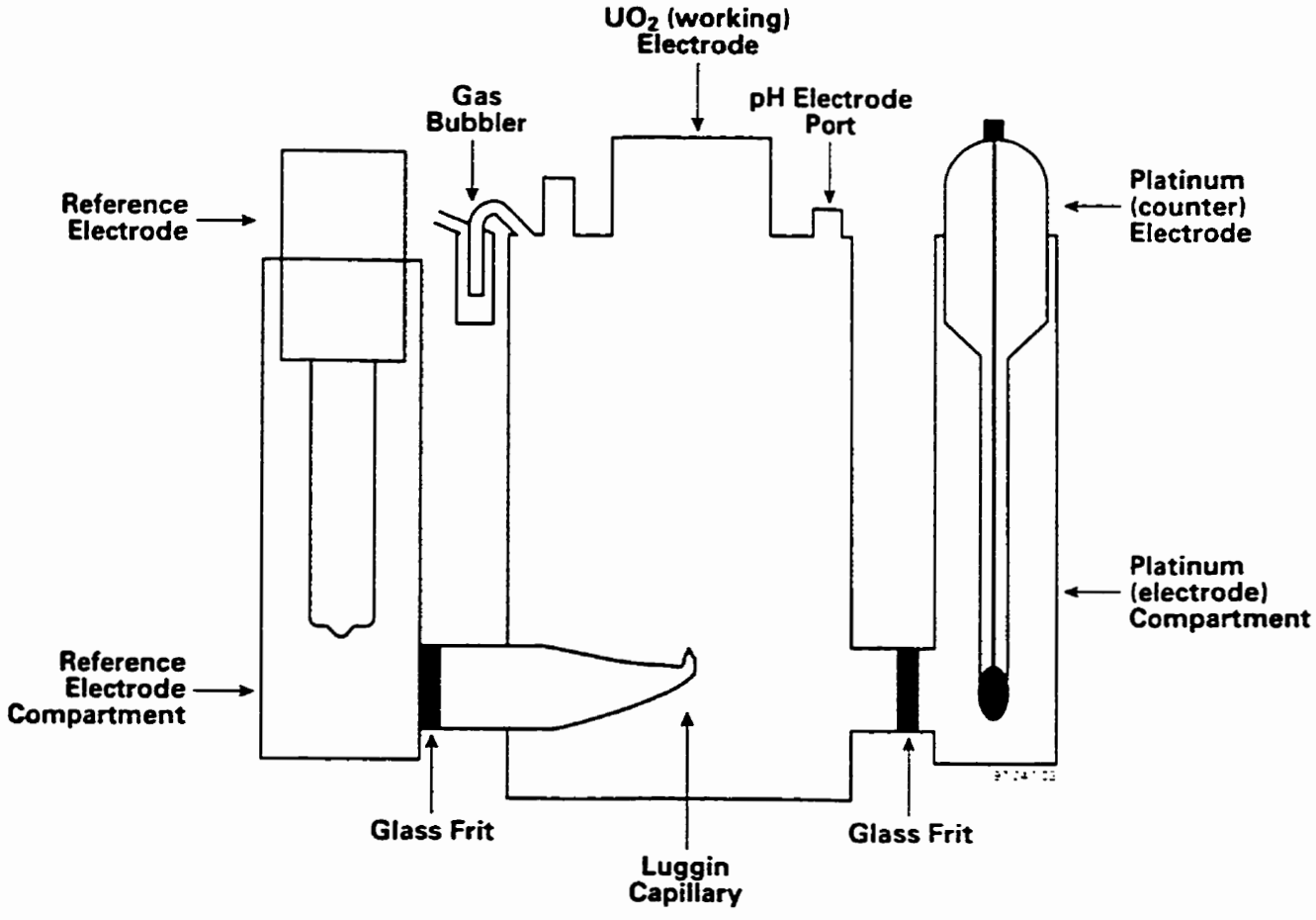

FIGURE 3.2: Schematic illustration of the standard three-electrode-three compartment cell used for electrochemical experiments.

The cell contained two side arms separated by glass frits from the main body. One side arm contained a commercial saturated calomel reference electrode (SCE) connected to the main body of the cell by a Luggin capillary to monitor the reference potential near the surface of the UO_2 working electrode. The other side arm contained a platinum wire counter electrode. The glass frits ensured that the saturated KCl solution in the reference electrode and the electrochemical products formed at the platinum counter electrode did not contaminate the electrolyte solution. The volume of electrolyte was approximately 500 mL.

The electrode potential was controlled by a potentiostat/galvanostat (EG&G Princeton Applied Research model 273) and the electrochemical data were monitored with a high impedance Keithly model 614 electrometer. All potentials were measured against a saturated calomel reference electrode (SCE). The rotation rate of the electrode was controlled by a model AFASR speed control from the Pine Instrument Company. The voltammograms were recorded on a Philips model PM8272 XYt recorder and the logarithmic current - time plots were recorded with a low impedance Electronic Controls Design (ECD) model M50 data logger and subsequently read into a Gateway 2000 4DX2-66P personal computer for graphical representation.

Rotating disc electrodes (RDE) were used to control the concentration of electroactive species or the products of the dissolution reaction at the electrode surface.

The scanning electron microscope (SEM) used was a model JEOL 6300V

microscope with a LaB6 Electron Gun and a Link ISIS Microanalysis Tower System. The X-ray photoelectron spectrometer (XPS) was a Physical Electronics Incorporated (PHI) - 500. The uranium analyzer was a model UA-3 SCINTREX.

3.3 SOLUTIONS

The solutions studied were 0.1 mol.L^{-1} $NaClO_4$, 0.97 mol.L^{-1} NaCl, Standard Canadian Shield Saline Solution (SCSSS), SCSSS + 10^{-2} mol.L^{-1} HCO_3^-, 0.97 mol.L^{-1} $CaCl_2$ and 0.1 mol.L^{-1} $NaClO_4$ + $5x10^{-4}$ mol.L^{-1} SiO_4^{4-}. The composition of SCSSS is shown in Table 3.2 [60].

TABLE 3.2

Composition of SCSSS

Ion	Concentration mol.L^{-1}
Na^+	$2.2x10^{-1}$
K^+	$1.3x10^{-3}$
Mg^{2+}	$8.2x10^{-3}$
Ca^{2+}	$3.7x10^{-1}$
Sr^{2+}	$2.3x10^{-4}$
Si^{4+}	$5.4x10^{-4}$
HCO_3^-	$1.6x10^{-4}$
Cl^-	$9.7x10^{-1}$
SO_4^{2-}	$8.2x10^{-3}$
NO_3^-	$8.1x10^{-4}$

The solutions used were made with distilled deionized water and analytical reagent-grade chemicals obtained from Fisher Scientific. The distilled deionized water was purified using a Millipore milli-RO6+ unit to remove organic and

inorganic impurities, followed by passage through Milli-Q-Plus ion exchange columns. This system provided water of high purity with a resistivity of 18.2 MΩ.cm. The pH of all solutions was adjusted to 9.5 with NaOH prior to the experiment except for the solution containing SCSSS buffered with HCO_3^-. This last solution was used with a pH of 7 to avoid the precipitation of Ca^{2+} as $Ca(OH)_2$. The pH was monitored with a Cole-Parmer pH electrode coupled to a Fisher Acumet meter (model 910). Solutions were sparged with Ultra high purity (UHP) Argon (Canada Liquid Air) for 30 minutes prior to cathodic cleaning and argon flow was then maintained over the solution while the experiment was in progress.

3.4 ELECTROCHEMICAL PROCEDURES

3.4.1 Cathodic Cleaning of UO_2 Electrode

The electrode was polished with 600 grit silicon carbide paper and then cathodically reduced at -2.0 V for 5 minutes after sparging with Argon for 30 minutes. XPS experiments show that a period of 5 minutes at -2.0 V is sufficient to reduce the electrode surface to a composition very close to $UO_{2.00}$ [24]. The steady state current, the applied potential and the IR corrected potential values were then recorded to calculate the resistance of the electrode using Ohms law,

$$R = \frac{E}{I} \qquad (3.1)$$

where R = resistance, E = potential and I = current. This procedure was used prior to the start of other experiments.

3.4.2 Cyclic Voltammetry or Potential Sweep Methods

In these experiments, the potential is scanned from E1 to E2 (Figure 3.3A) and back at a specific scan rate in the range 5 to 20 $mV.s^{-1}$ and the current recorded as a function of the potential. The output is a CV (Figure 3.3B) which allows us to separate the various stages of oxidation (anodic, or positive going, scan) and reduction (cathodic, or negative going, scan); i.e. obtain a redox spectrum.

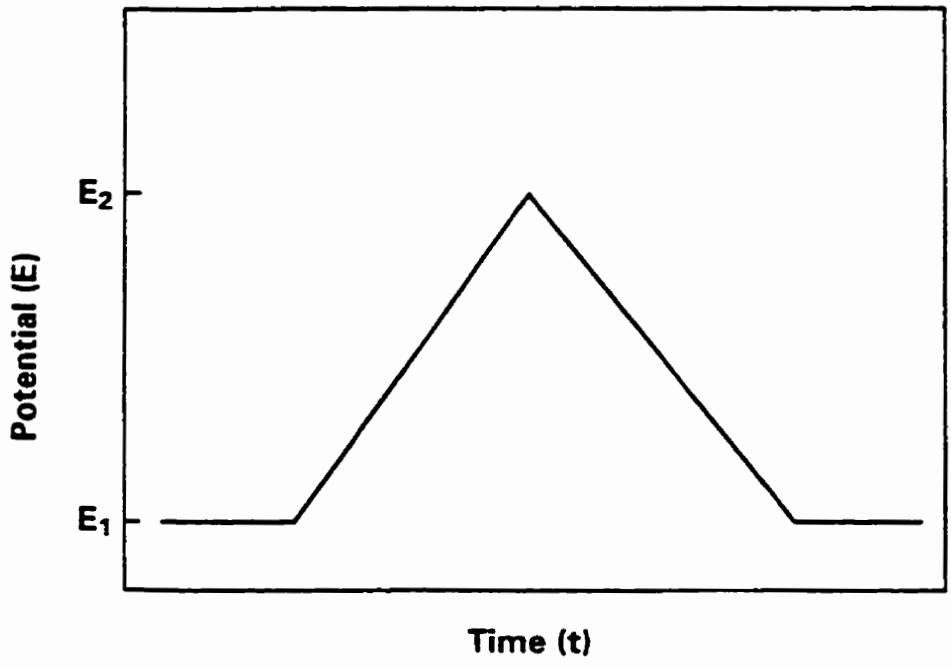

FIGURE 3.3A: Schematic outlining the experimental procedure for scanning the potential.

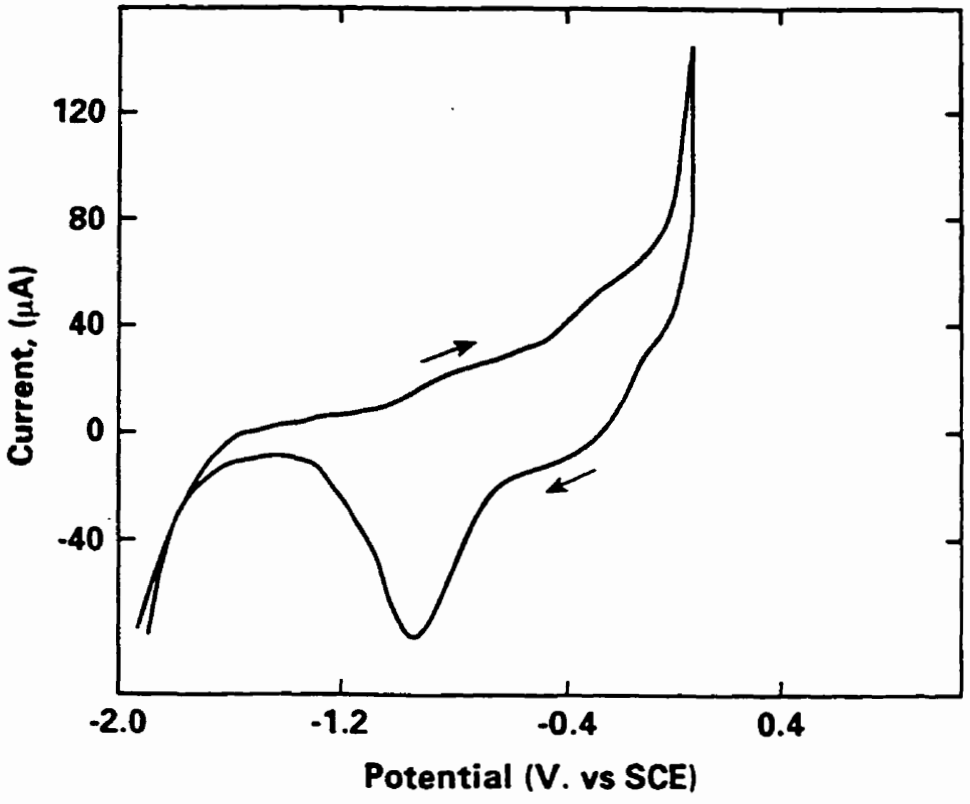

FIGURE 3.3B: Schematic outlining the cyclic voltammogram recorded for UO_2 in 0.1 mol.L^{-1} $NaClO_4$ (pH = 9.5) .

The size, shape and charge obtained by integration of a peak in the voltammogram can be used to obtain the amount of oxidation or reduction that has occurred within a specific potential interval. The peak positions over the anodic potential range are an indication of various stages of oxidation and help to determine the anodic oxidation mechanism of UO_2. The reverse cathodic scan peak positions indicate whether the oxidized species formed during the anodic scan are reduced or lost to solution by dissolution. The extent of oxidation can be controlled by changing the value of the potential at the anodic limit, E2. The E2 values for the experiments ranged from +0.1 V to +0.5 V.

3.4.3 Anodic Oxidation Under Controlled Potential (Potentiostatic) Conditions

In these experiments the potential of the working electrode (UO_2) is held constant for the duration of the oxidation (Figure 3.4).

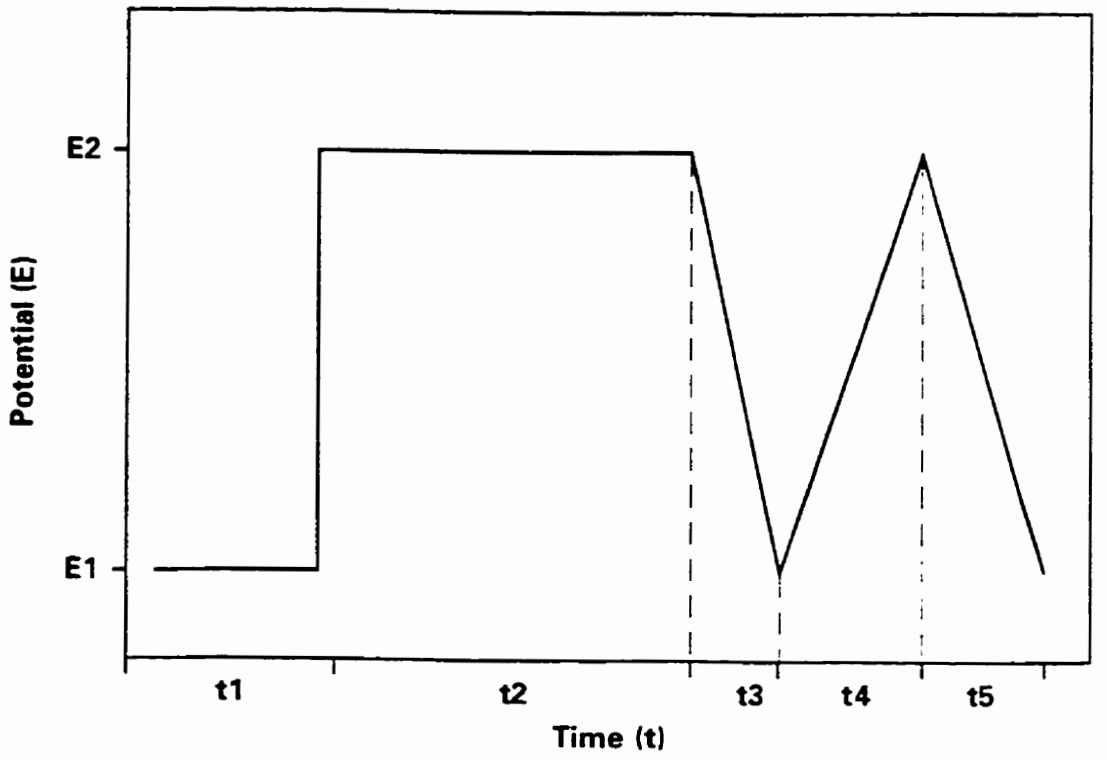

FIGURE 3.4: Schematic outlining the experimental procedure for anodic oxidation.

After cathodic cleaning at -2.0 V (interval t1), the potential is stepped to a value E2 within the range +0.1 V to +0.55 V and the current recorded as a function of time by sampling at 10 second intervals. After a known total duration (generally 1.5 hours) (interval t2), the potential is scanned back to E1 at 20 $mV.s^{-1}$ to

reduce any surface films formed at E = E2 (interval t3 in Figure 3.4). The procedure performed in interval t3 is a cathodic stripping voltammogram (CSV). After long oxidations at high potentials a current for the reduction of soluble UO_2^{2+} can also be observed in interval t3. In general, for small amounts of dissolution product, dissolved species are transported to the bulk solution, where they are diluted to a very small concentration in the large volume of solution used. A current for their electrochemical reduction is not then observed.

Alternatively, after potentiostatic oxidation at E2 and the recording of the CSV, the potential is swept from E1 to E2 and back again at 20 $mV.s^{-1}$ and the current recorded as a function of potential (intervals t4 and t5 in Figure 3.4). This final CV is used to look at the consequences of the long potentiostatic oxidation on the electrode reactivity.

The electrode was then reprepared and cathodically reduced at -2.0 V prior to repeating the experiment at a different value of E2.

3.4.4 Current Interrupt Method

Compensation for IR drop in the electric circuit was achieved using the current interrupt method. In this method, the current is interrupted periodically (for a period of 190 μs). The potential drop across any purely resistive component will be immediate, but discharge of the double layer capacitance by means of the faradaic reaction will occur with a relaxation time (τ) determined by the value of the double layer capacitance (C_{dl}) and the charge transfer resistance

(R_{ct}) of the faradaic reaction,

$$\tau = R_{ct}C_{dl} \qquad (3.2)$$

For UO_2 the major resistance in the circuit is that of the electrode (R_e) since the solutions used generally have a high conductivity, and the key circuit elements can be represented as shown in Figure 3.5A.

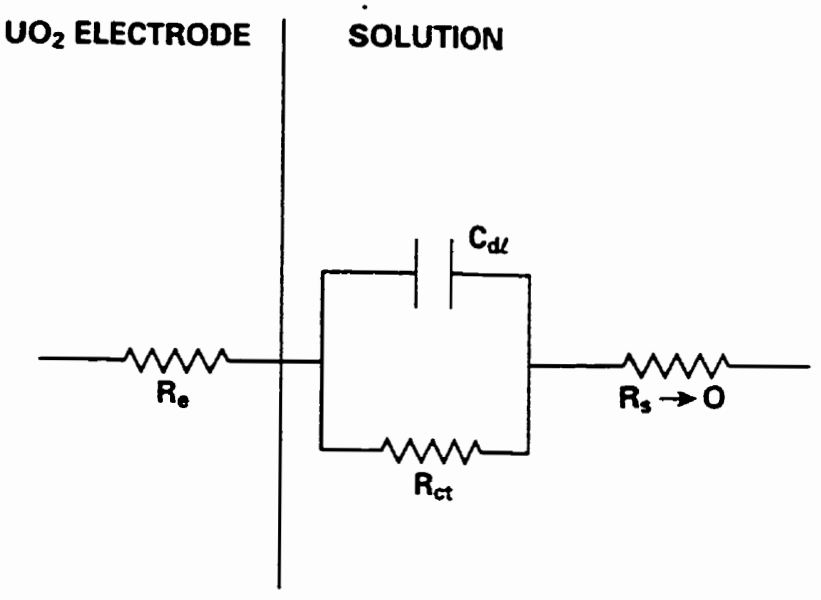

FIGURE 3.5A: Simple electrical equivalent circuit representing the UO_2 electrode / solution interface for a high conductivity solution.

The faradaic processes occurring on UO_2 under voltammetric conditions are slow (i.e. R_{ct} is large) and discharge of the double layer capacitance by means of the faradaic reaction is negligible within the 190 μs interrupt period.

Figure 3.5B shows a schematic of the potential recorded over an interrupt period with a fast oscilloscope.

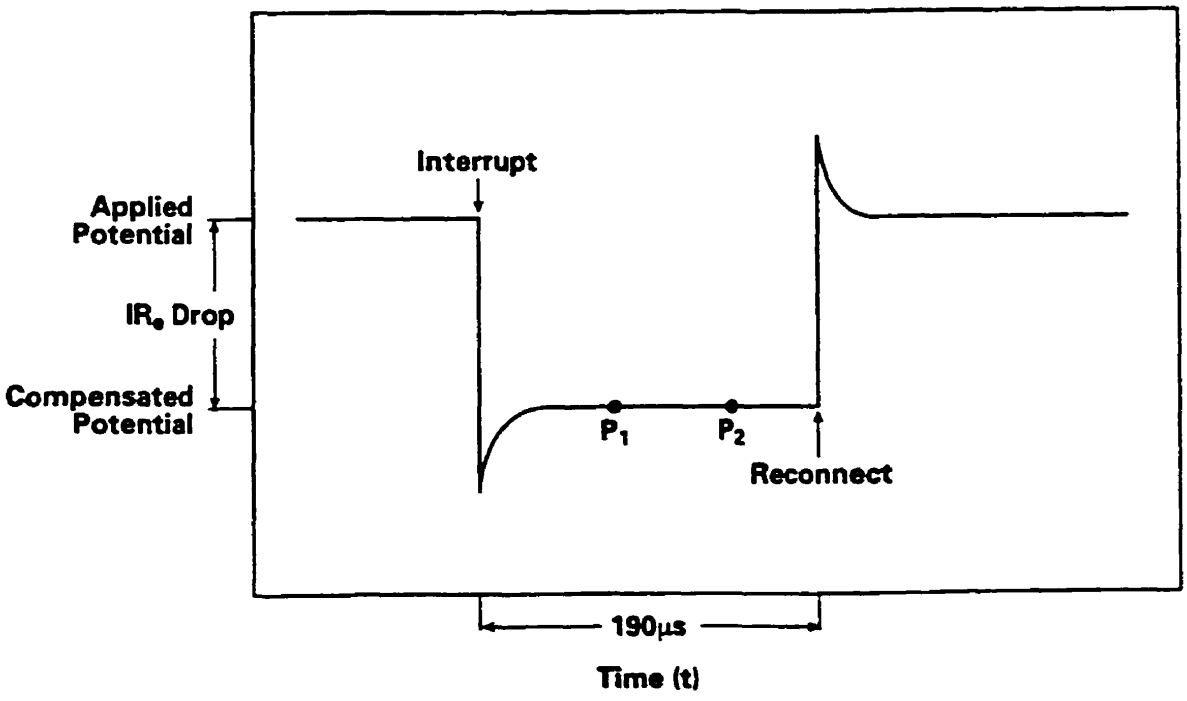

FIGURE 3.5B: Schematic representation of the measured electrode potential over one interrupt cycle.

Linear extrapolation through two points recorded at 75 μs and 150 μs yields an accurate determination of the IR_e drop and hence, if desired, a value of R_e. The transients that follow the interrupt and reconnect steps are due to the electronic switch used for the current interruption.

3.4.5 Information obtained from integrated voltammograms

Figure 3.6 is a schematic of a voltammogram in which the hatched areas illustrate the integrated areas.

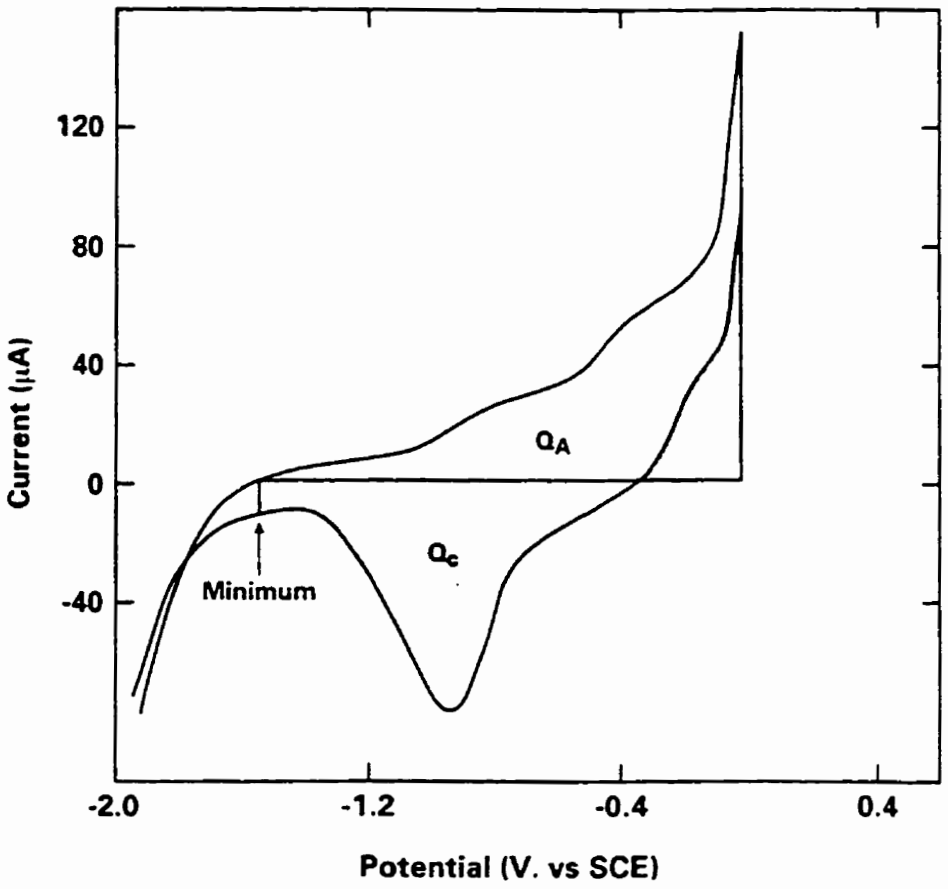

FIGURE 3.6: Schematic of a cyclic voltammogram showing the integrated areas for the charge (Q) consumed by oxidation (Qa) or reduction (Qc). The double hatched area was integrated twice and included with Qa to account for the anodic oxidation current which flows at the beginning of the reverse scan.

The current through the external circuit (i),

$$i = AI \qquad (3.3)$$

where A is the electrode surface area and I is the current density, is a measure of the rate of the electrode reaction. The integrated areas correspond to the charge (Q) consumed by oxidation or reduction and are measures of the total amount of electrochemical reaction which has occurred. The charge required to convert m moles of starting material to product in an electrochemical reaction involving the transfer of n electrons is calculated using Faraday's law,

$$Q = \int idt = mnF \qquad (3.4)$$

where the current is integrated as a function of time. Since the scan rate (ν) is defined as,

$$\nu = \frac{dE}{dt} \qquad (3.5)$$

(where dE is the change in potential and dt is the change in time),
the charge can be obtained by integration of the voltammetric curve, i.e.

$$Q = \nu^{-1} \int idE \qquad (3.6)$$

Integration of anodic currents yields the value Qa, the total amount of UO_2 oxidized, and the cathodic currents, Qc, the total amount of oxidized UO_2 subsequently reduced. Qa (the top hatched area) is the charge consumed in all electrochemical film formation and dissolution processes. The double hatched area was integrated twice to include continuing oxidation at the beginning of the reverse scan and was included in Qa. For experiments conducted with rotating electrodes in cells containing a large volume of solution, the products of oxidative

dissolution will be transported to the bulk of the solution and, hence, unavailable for cathodic reduction on the reverse scan. Consequently, Qc (the bottom hatched area) is generally the charge due to the reduction of oxidized films formed on the UO_2 surface on the forward scan. Also, it was necessary to approximate the separation of the oxide reduction from the water reduction area. This was achieved by arbitrarily selecting the cut off point at the cathodic current minimum indicated in Figure 3.6.

The difference,

$$Qd = Qa - Qc \qquad (3.7)$$

can be taken as the amount of oxidized material lost by dissolution and transported to the bulk of the solution.

3.5 OTHER METHODS

3.5.1 X-ray Photoelectron Spectroscopy (XPS)

XPS was used to characterize the surface films formed on UO_2 by electrochemical oxidation. On removal from the electrochemical cell, the UO_2 electrode was washed and put in the high vacuum chamber of the spectrometer . After pumping the chamber to a pressure of $< 10^{-9}$ torr, the electrode was bombarded with high energy monochromatic x-rays ($h\nu$ = 1253.6 eV). The XPS spectra were excited using magnesium K-α radiation filtered through an aluminum window. The energy scale of the spectrometer was calibrated using the following accurately known line positions of noble metals: Au $4f_{7/2}$, 84.0 eV,

Ag $3d_{5/2}$, 368.3 eV, and Cu $2p_{3/2}$, 932.56 eV [88]. The equation governing the energy of emitted electrons is,

$$h\nu = E_b + KE + E_R + \phi_{sp} \qquad (3.8)$$

where

E_b is the binding energy (ie. the energy required to remove an electron from a specific core level of the atom)

KE is the kinetic energy of an electron in the spectrometer

E_R is the recoil energy at the site of electron ejection

ϕ_{sp} is the spectrometer work function that must be applied.

XPS spectra yield chemical information on the composition of the top 2 to 3 nm of the electrode surface. Information on oxidation states can be obtained because the binding energy of an electron in a given orbital is slightly affected by its electronic environment.

For a UO_2 electrode, the two oxidation states U^{4+} and U^{6+} can be considered present in UO_{2+x}. Two bands in the XPS spectrum of uranium dioxide are useful for determining the oxidation state in the electrode surface, the valence band and the U4f band [24]. Spectra were recorded for the U4f, C-1s and O-1s bands and the valence region of UO_2 electrodes. The C-1s spectra are due to carbon impurities and were recorded to monitor for surface charging effects [24]. Figure 3.7 shows the XPS spectrum of the valence band region for a UO_2 electrode after cathodic reduction at -2.0 V for 5 minutes and corresponds

closely to the literature spectra for $UO_{2.00}$ [24].

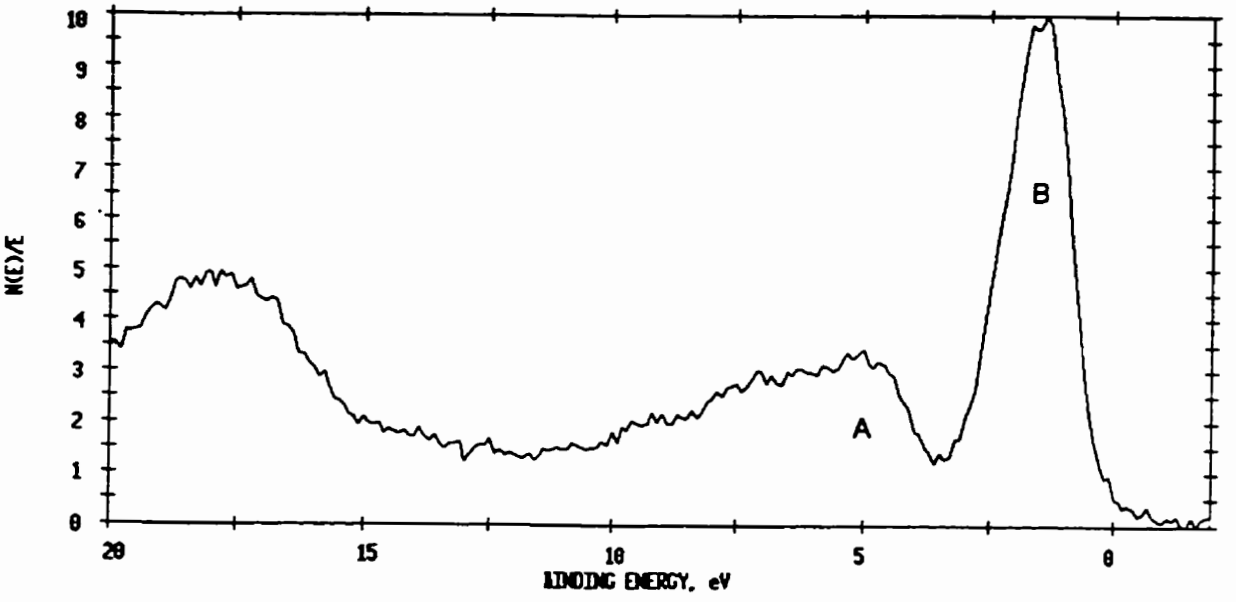

FIGURE 3.7: XPS spectrum of the valence band region after cathodic reduction at -2.0V for 5 minutes. Area A corresponds to the O 2p region and Area B to the U 5f region.

After oxidation at more positive potentials, the peak at ~1.8 eV which is due to the non-bonding 5f valence electrons, decreases in intensity. In pure U(VI) samples, this peak is absent.

Uranium forms a large number of oxides with intermediate stoichiometries between UO_2 and UO_3 containing both U(IV) and U(VI) [24]. The band at ~380 eV, resulting from the $4f_{7/2}$ electrons, is used to monitor the chemical state

of uranium atoms [24]. In mixed uranium oxides this band can be resolved into the U(IV) and U(VI) components because the U(IV) and U(VI) bands are fixed at specific energies which are 1.3 ± 0.2 eV apart [24]. Therefore, quantitative information about the relative amounts of U(IV) and U(VI) in the UO_2 electrode surfaces can be determined.

This information is obtained using a least squares curve fitting routine, illustrated in Figure 3.8, which shows the spectrum for a UO_2 electrode after cathodic reduction at -2.0 V (vs. SCE) for 5 minutes.

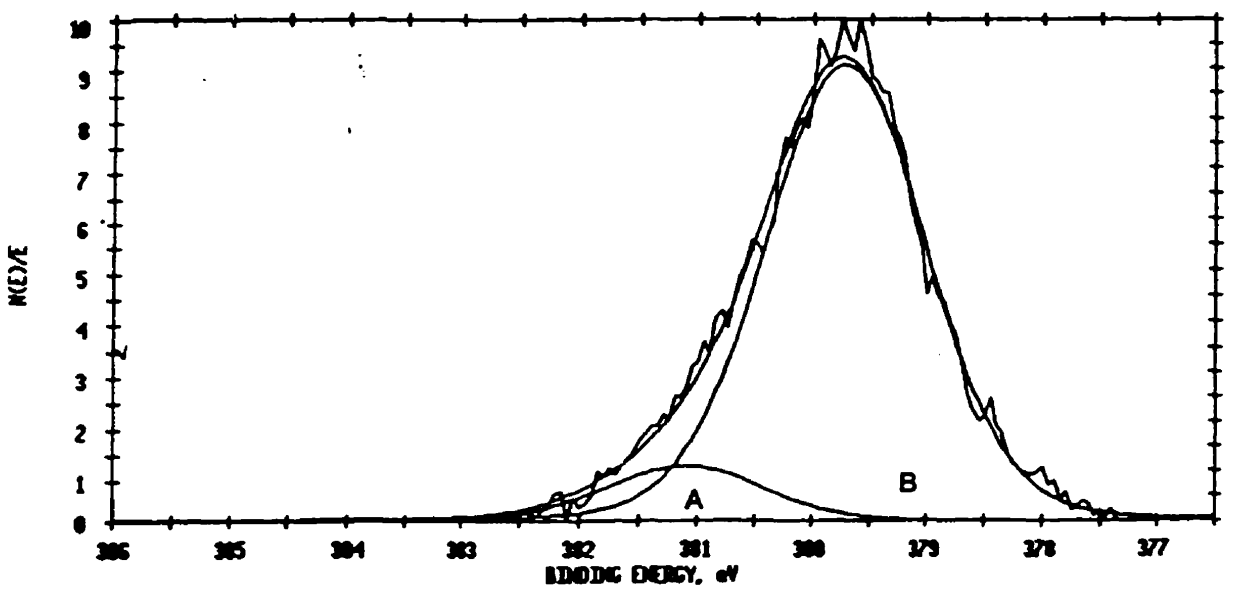

FIGURE 3.8: XPS spectrum for a UO_2 electrode (ZR3) after cathodic reduction at -2.0V for 5 minutes. Area A is the U(VI) component and Area B is the U(IV) component.

The peak is fitted with one band which has a maximum at 380.2 eV and full width at half maxima (FWHM) of ~2.2 eV, and a second much weaker band at 381.5

eV that is used to account for the tailing of the $U4f_{7/2}$ band [24]. Further reduction of the UO_2 surface did not alter the spectrum and this spectrum compares favourably with literature spectra for fully reduced UO_2 [24]. However, further anodic oxidation of the UO_2 electrode resulted in a mixed oxide spectra, an example of which is shown in Figure 3.9. This spectrum can be resolved into U(IV) and U(VI) spectra by constraining the line positions and widths to those for pure UO_2 and UO_3 [24]. The relative peak areas, after correcting for the UO_2 tailing component, give the relative amounts of U(IV) and U(VI) in the electrode surface.

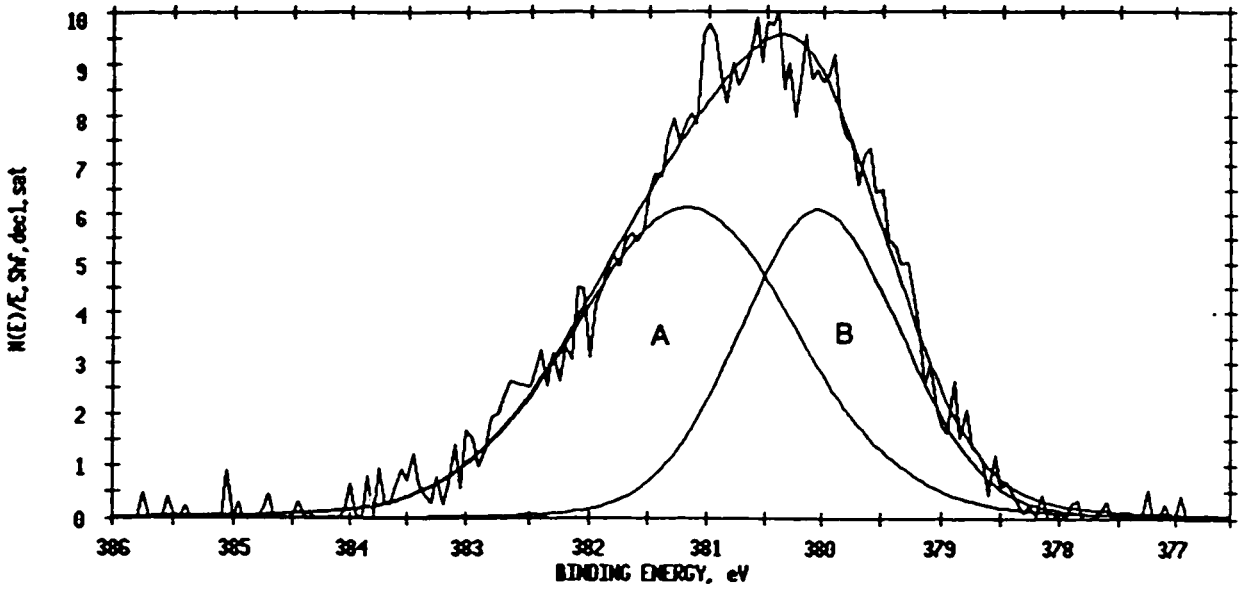

FIGURE 3.9: XPS spectrum for a UO_2 electrode (ZR3) after anodic oxidation at 0.5V for 90 minutes in SCSSS. Area A is the U(VI) component and Area B is the U(IV) component.

3.5.2 SEM

SEM was used to characterize the surface topography of the UO_2 electrode after potentiostatic oxidation experiments. Micro-optical pictures were recorded at different magnifications (100, 500, 1000, 2500, 5000X).

3.5.3 Uranium analysis

Analytical measurements of the concentration of the dissolution product (UO_2^{2+}) were made using a UA-3 SCINTREX uranium analyser. This technique measures the fluorescence of a uranyl complex using a nitrogen laser. The addition of a buffered inorganic complexing reagent, FLURAN, converts the various uranyl species present in the solution sample into a single complex with a high luminescent yield. A detailed procedure is given in the UA-3 Uranium Analyser Operators Instructions.

4.0 CYCLIC VOLTAMMETRY IN PERCHLORATE SOLUTIONS

4.1 RESULTS

4.1.1 Cyclic Voltammetry in Perchlorate Solutions

Figures 4.1and 4. 2 show IR compensated CV's in 0.1 mol.L^{-1} $NaClO_4$ recorded at a scan rate of 10 mV.s^{-1} from an initial potential of -2.0 V to an anodic limit of +0.3 V, for the L6 and ZR1 electrodes, respectively. For both electrodes the CV's were similar in appearance and the current interrupt method yielded electrode resistances of 433 and 348 ohms, respectively. Similar CV experiments were performed on the other four electrodes and a range of resistance values obtained (Table 3.1). These four electrodes generally showed similar features to L6 and ZR1 for the first scan performed on a freshly polished surface, irrespective of their different resistance values. Some electrodes had a slightly higher peak current than others for peaks I and V indicated in Figure 4.1.

4.1.2 Repetitive Voltammetric Cycling

Figures 4.3 to 4.6 show repetitive voltammetric scans (scan rate = 10 mV.s^{-1}) recorded without IR compensation on the L6 and J2 electrodes to two different anodic limits, 0.3 V (Figures 4.3 and 4.5) and 0.5 V (Figures 4.4 and 4.6) in 0.1 mol.L^{-1} $NaClO_4$.

For scans to 0.3 V on both L6 and J2 (Figures 4.3 and 4.4), peak I increases on consecutive cycles, while peak II remains unchanged. For scans to a limit of 0.5 V (Figures 4.5 and 4.6), peaks I, II and V remain unchanged for L6,

but increase with each cycle for J2. The current in region III is the same for L6 and for J2 at the anodic limit of 0.5 V.

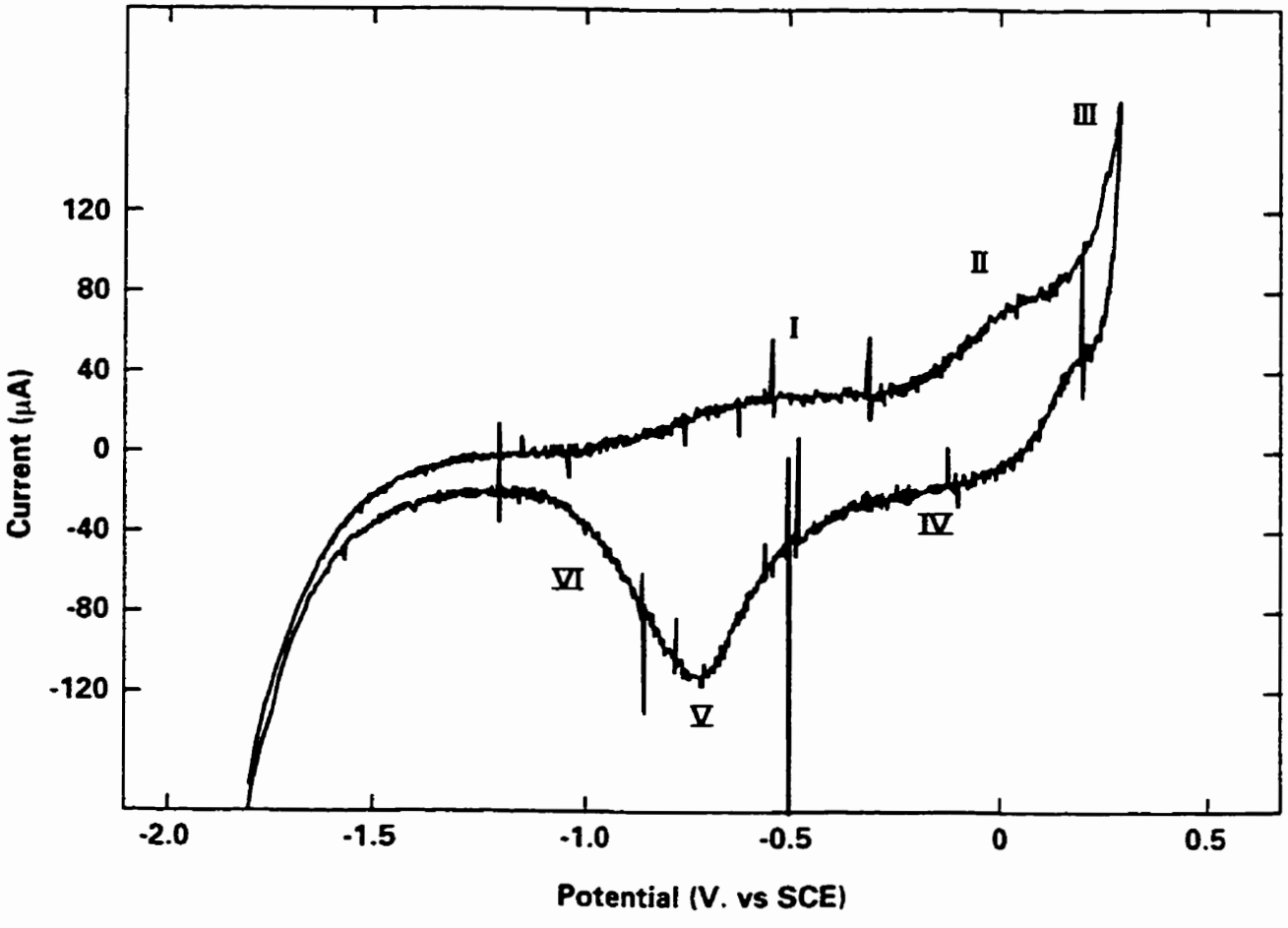

FIGURE 4.1: IR compensated CV recorded at a scan rate of 10 $mV.s^{-1}$ to an anodic limit of 0.3 V in 0.1 $mol.L^{-1}$ $NaClO_4$ for the L6 electrode.

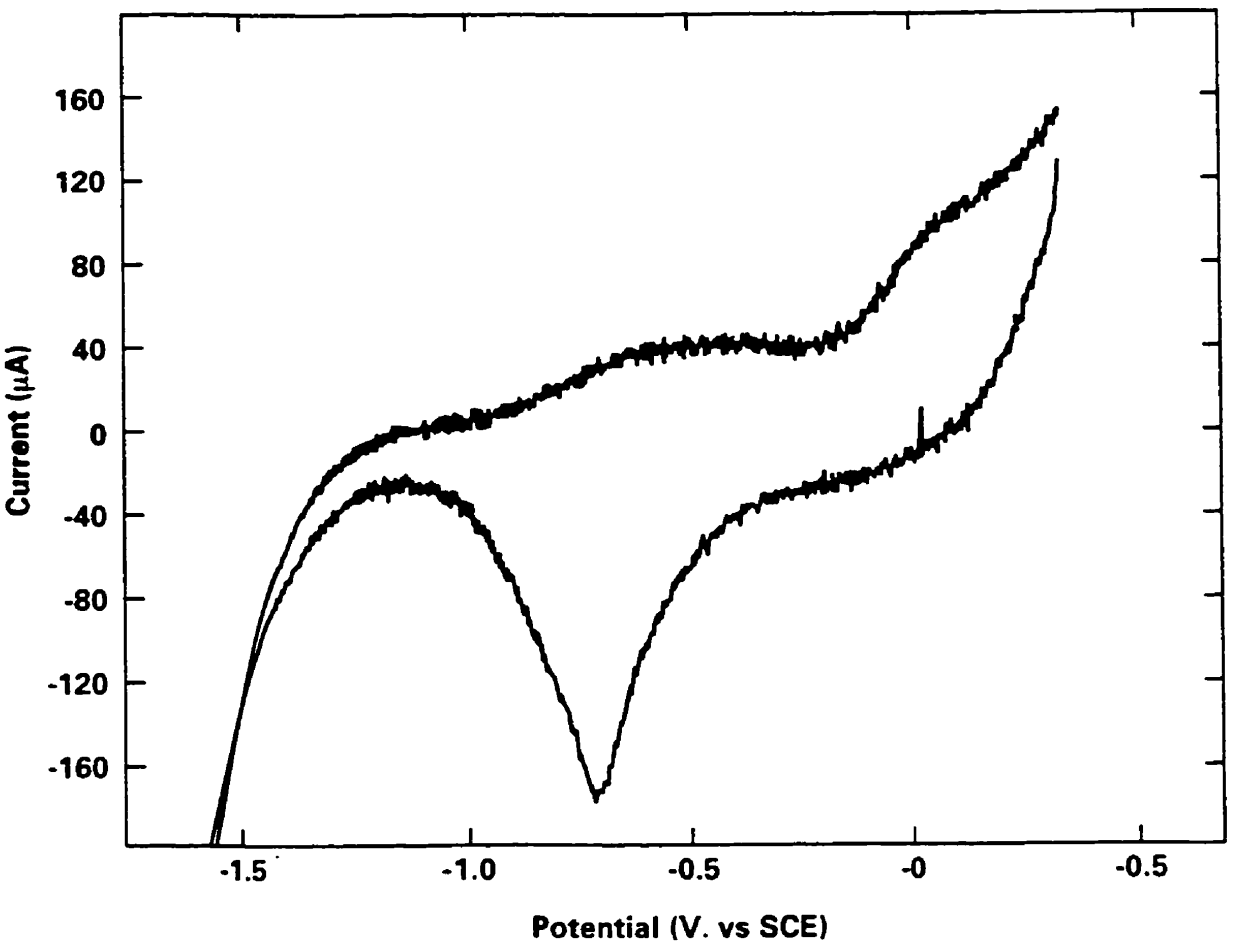

FIGURE 4.2: IR compensated CV recorded at a scan rate of 10 $mV.s^{-1}$ to an anodic limit of 0.3 V in 0.1 $mol.L^{-1}$ $NaClO_4$ for the ZR1 electrode.

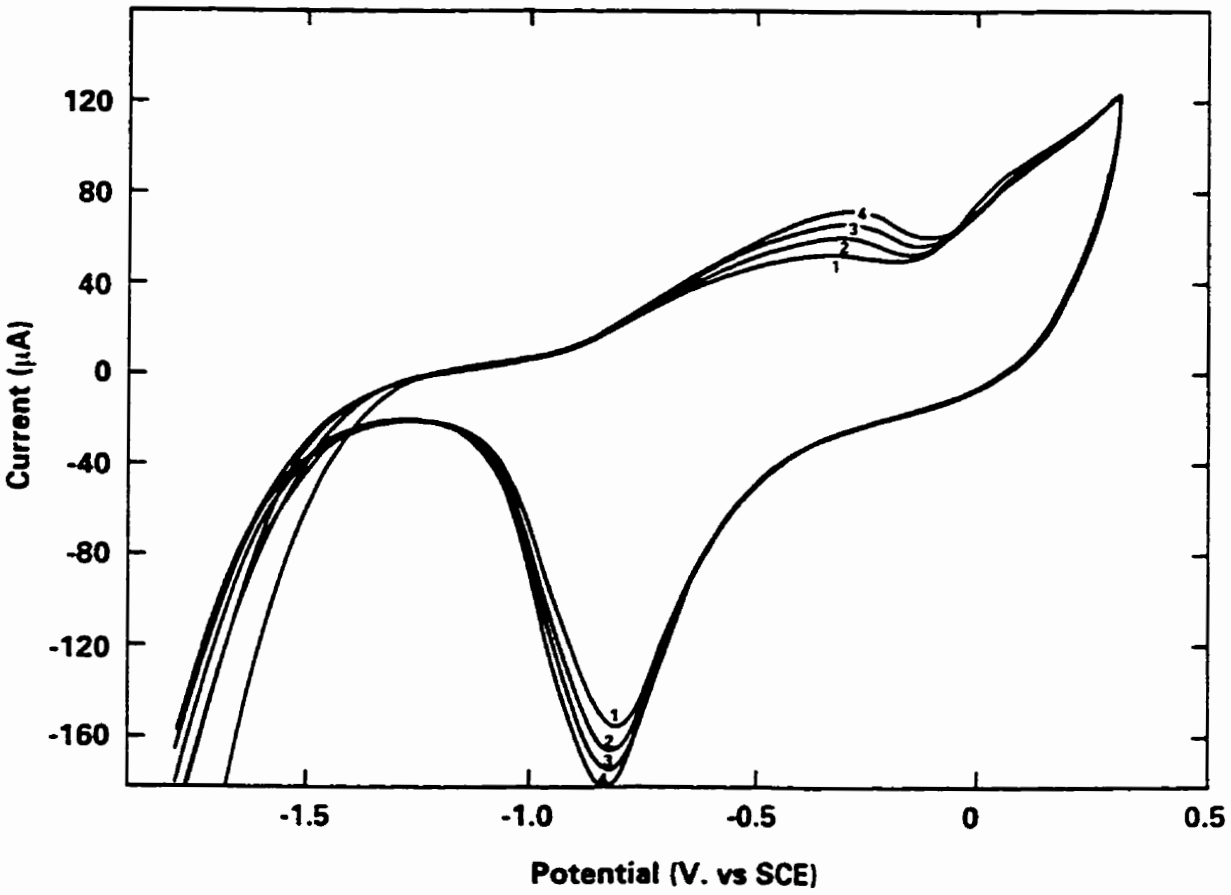

FIGURE 4.3: Repetitive CV's recorded at a scan rate of 10 $mV.s^{-1}$ to an anodic limit of 0.3 V in 0.1 $mol.L^{-1}$ $NaClO_4$ for the L6 electrode.

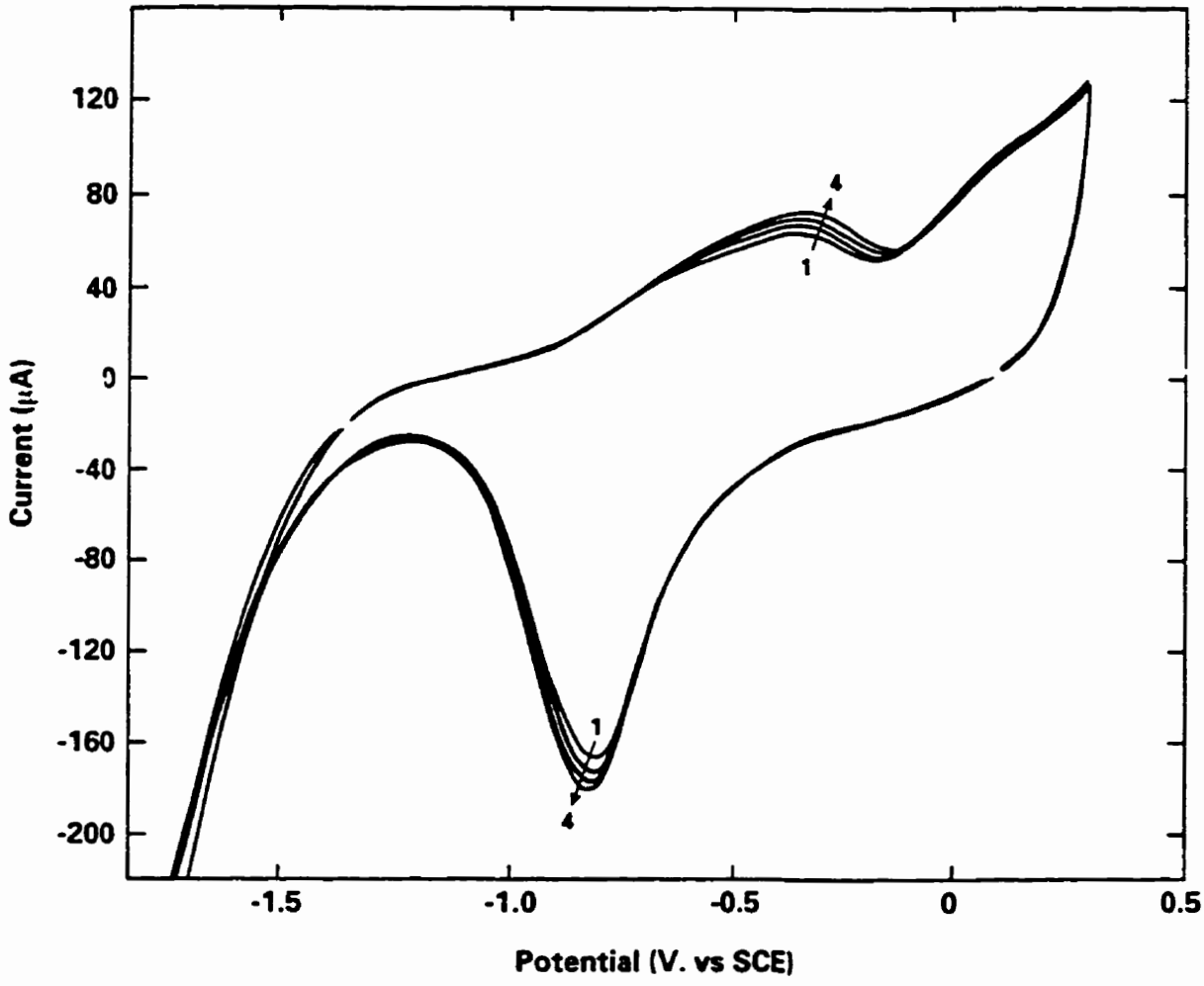

FIGURE 4.4: Repetitive CV's recorded at a scan rate of 10 $mV.s^{-1}$ to an anodic limit of 0.3 V in 0.1 $mol.L^{-1}$ $NaClO_4$ for the J2 electrode.

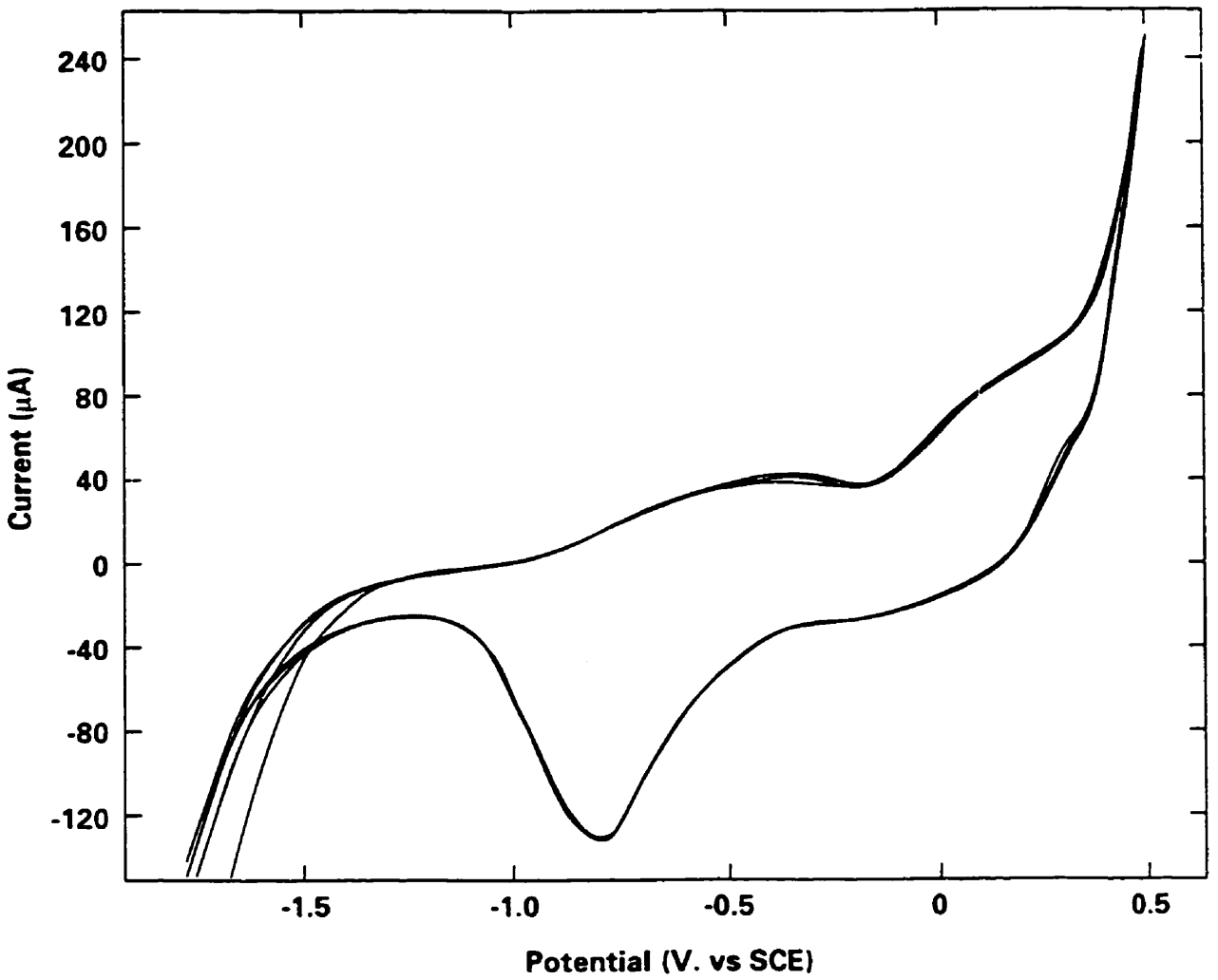

FIGURE 4.5: Repetitive CV's recorded at a scan rate of 10 $mV.s^{-1}$ to an anodic limit of 0.5 V in 0.1 $mol.L^{-1}$ $NaClO_4$ for the L6 electrode.

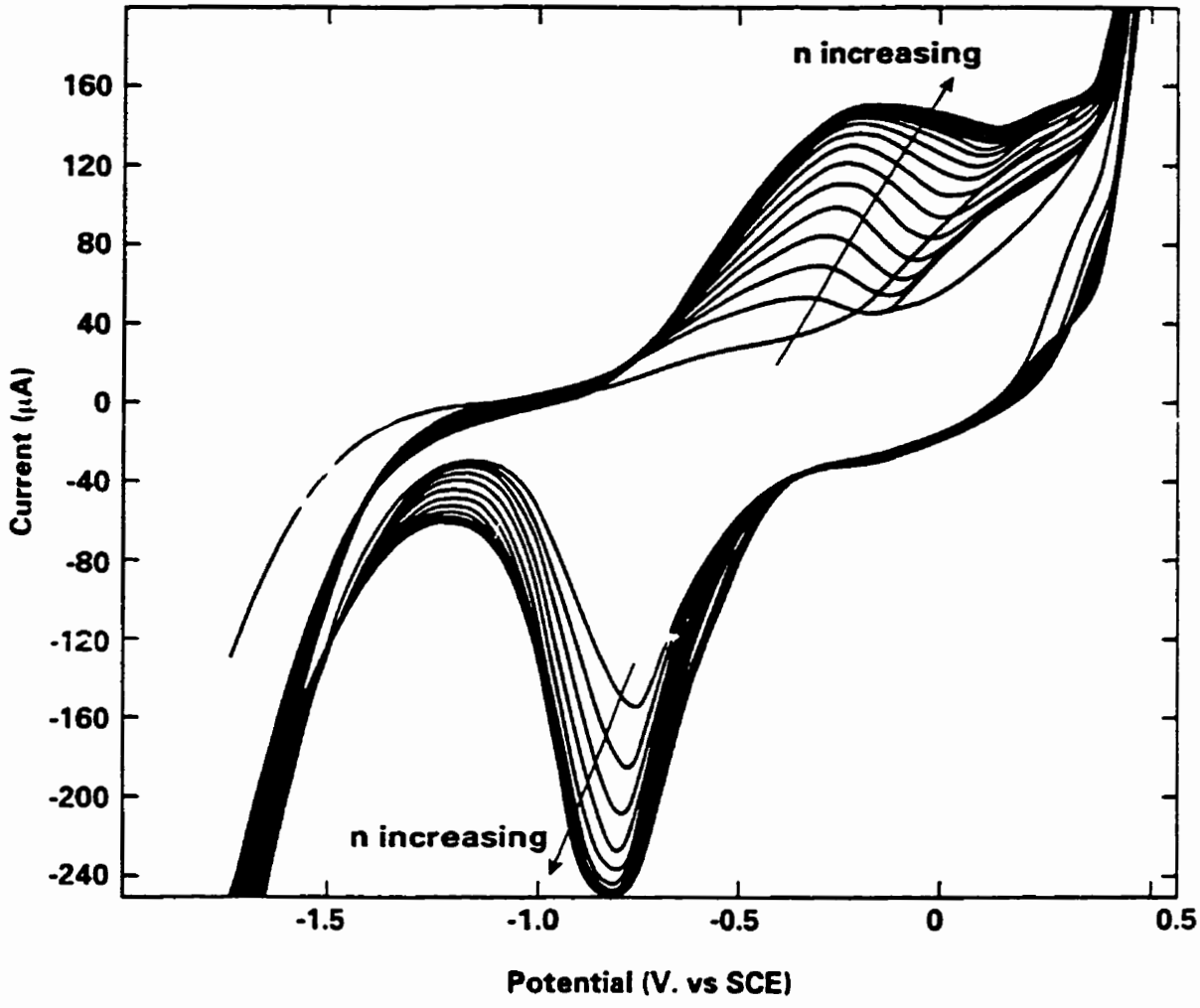

FIGURE 4.6: Repetitive CV's recorded at a scan rate of 10 $mV.s^{-1}$ to an anodic limit of 0.5 V in 0.1 $mol.L^{-1}$ $NaClO_4$ for the J2 electrode.

4.2 DISCUSSION

The CV behaviour on the first scan, for all six electrodes tested, is consistent with previously published information (Section 2.4.3). The current at peak I has been attributed to the preferential oxidation of material at reactive surface sites possibly located in grain boundaries [16]. A possibility is that the slight differences in currents at peaks I and V in the CV's for different electrodes may be attributed to a variation in reactivity over the UO_2 surface. This could arise during the fuel fabrication process. An alternative possibility could be that the polishing procedure used in electrode preparation is not reproducible. While this irreproducibility might explain the variation, and similarities, observed on the first voltammetric scans, it does not explain the behaviour observed on repetitive scanning (see below).

The reductive sintering process used could leave the grain boundaries slightly hyperstoichiometric and more reactive (Section 2.1). If this is the case then the oxidation of hyperstoichiometric material occurs at much lower potentials than the oxidation of stoichiometric material. Evidence to support this is given by Betteridge et al. [76] who compared CV's for a number of hyperstoichiometric UO_{2+x} standards, two of which are shown in Figure 4.7.

The UOX1 ($UO_{2.001}$) electrode is a nearly stoichiometric UO_2 fuel and shows behaviour very similar to the fuel specimens used in this study. The UOX5 ($UO_{2.113}$) is much more readily oxidizable (ie. more reactive) at lower anodic potentials. Also, visible roughening and discoloration were observed on the UOX5 surface after cycling repeatedly.

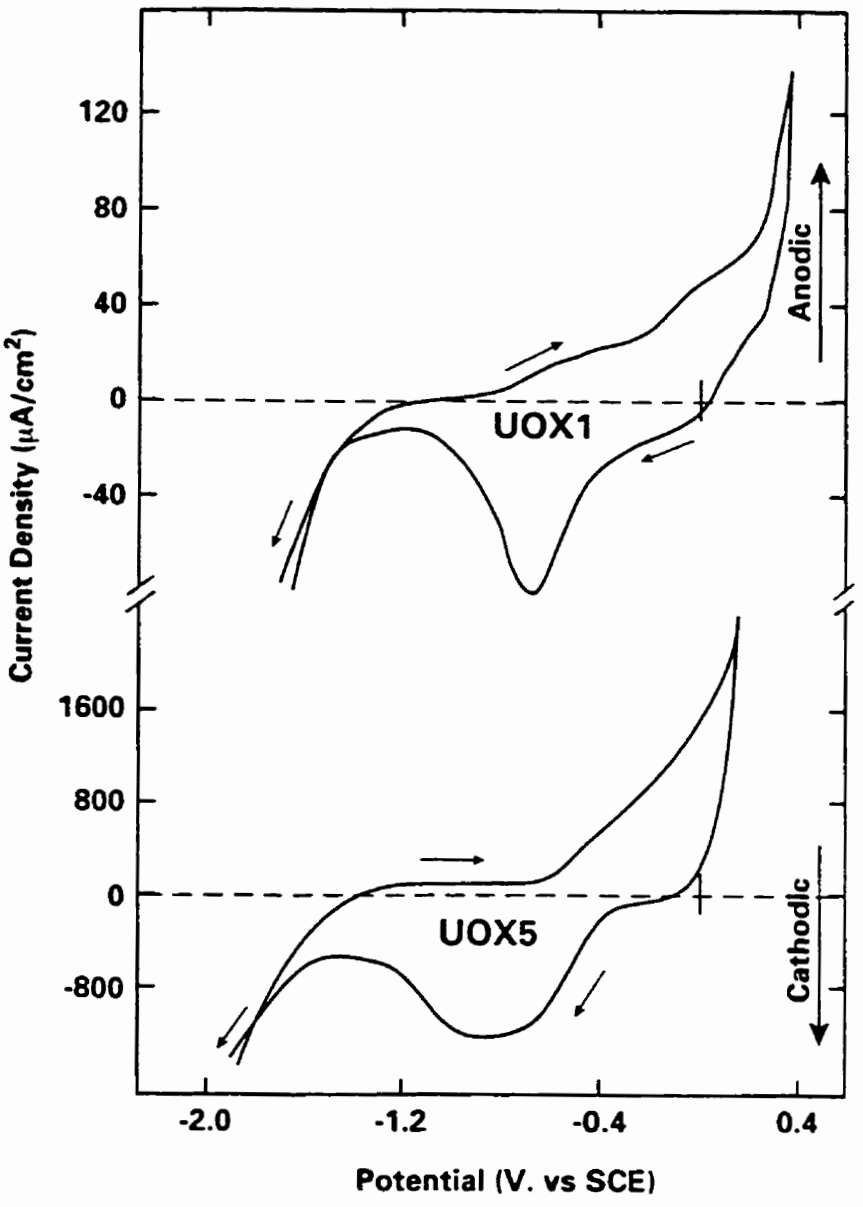

FIGURE 4.7: IR compensated CV's recorded to an anodic limit of 0.3 V in 0.1 mol.L^{-1} $NaClO_4$ for hyperstoichiometric UO_2 electrodes (A) UOX1 ($UO_{2.001}$) and (B) UOX5 ($UO_{2.113}$) [76].

This indicates localized attack, possibly at grain boundaries. In view of this we can attribute the process at peak I to the oxidation reaction,

$$UO_{2+x} \rightarrow UO_{2.33} \qquad (4.1)$$

occurring to a depth of only a few monolayers or at specific areas of the surface, and the process at peak II to the reaction,

$$UO_2 \rightarrow UO_{2.33} \qquad (4.2)$$

occurring more generally on the electrode surface. As discussed in section 2.4.3, peak V can be attributed to the reduction process,

$$UO_{2.33} \rightarrow UO_{2+x} \qquad (4.3)$$

Peak V first appears when the potential is scanned to an anodic potential limit of -0.8 V, where the oxidation of UO_{2+x} to $UO_{2.33}$ (peak I) begins. Peak V increases in size as the potential is scanned through the range where both peaks I and II occur. Therefore, peaks I and II are thought to yield the same oxidation product, $UO_{2.33}$, which is reduced on the reverse scan at peak V. XPS has shown that the reduction process at peak V does not produce stoichiometric UO_2, but UO_{2+x} with $x \cong 0.1$ [25]. The increase in size of peak I on each successive cycle suggests that the amount of non-stoichiometric UO_2 (UO_{2+x}) available for oxidation increases with each anodic potential scan through the potential range up to +0.3 V. It is possible that this process is associated with grain boundaries and that oxidation extends slightly further across the electrode surface and deeper into grain boundaries with each cycle. An attempt to illustrate this schematically is shown in Figure 4.8.

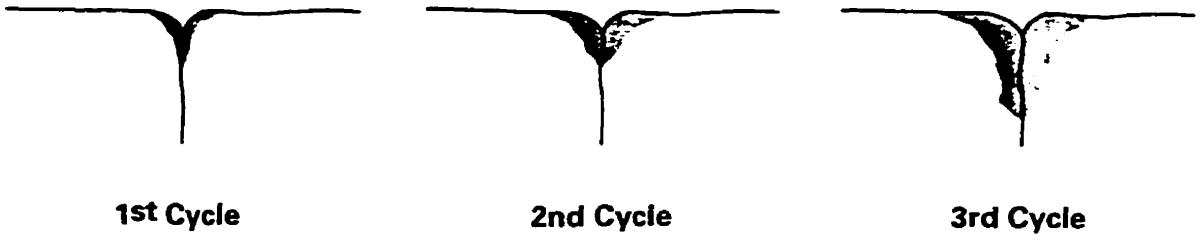

FIGURE 4.8: Schematic illustration to show the possible effect of oxidation on the electrode surface and at grain boundaries after (A) 1 cyclic scan (B) 2 cyclic scans and (C) 3 cyclic scans.

The J2 electrode showed the same behavior as L6 when scanned to an anodic limit of 0.3 V.

When L6 is scanned to an anodic potential limit of 0.5 V, peaks I, II and V remain unchanged on consecutive scans. This implies that the UO_2 surface is the same composition at the beginning of each successive scan. In region III, the $UO_{2.33}$ formed at peaks I and II begins to dissolve electrochemically as UO_2^{2+} (Section 2.4.3),

$$UO_2 \rightarrow UO_{2.33} \rightarrow UO_2^{2+}$$

For potentials > 0.3 V, dissolution occurs from the surface of a $UO_{2.33}$ layer of constant thickness. This $UO_{2.33}$ is available for reduction on the reverse scan but peak V does not increase in size since its electrochemical (oxidative) dissolution has maintained the layer at a steady state thickness. Also, since no extra UO_{2+x} is formed at peak V, peak I is not enhanced on the next scan. In effect this would lead to an etching of the surface with successive scans as illustrated schematically in Figure 4.9.

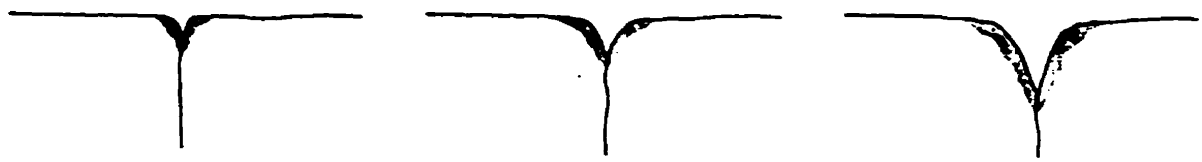

FIGURE 4.9: Schematic illustration to show the possible effect of oxidation on the electrode surface and at grain boundaries after (A) 1 cyclic scan, (B) 2 cyclic scans and (C) 3 cyclic scans.

For J2 however, scanning to an anodic potential limit of 0.5 V, leads to an increase in the size of peaks I, II and V. In contrast to the behaviour observed for L6, the oxidation product, $UO_{2.33}$ accumulates on the electrode surface (possibly in the grain boundaries) and does not dissolve. The majority of the $UO_{2.33}$ formed is available to be reduced at peak V and the UO_{2+x} formed by its reduction is then reoxidized at peak I on the next scan. This activation process becomes much more extensive when the anodic limit is extended from 0.3 to 0.5 V.

However, if the scan on J2 is IR compensated (Figure 4.10) a very large, and apparently reversible current for dissolution is observed for $E > 0.3$ V, and the cathodic peak V for the reduction of $UO_{2.33}$ has a small charge associated with it compared to the charge consumed anodically.

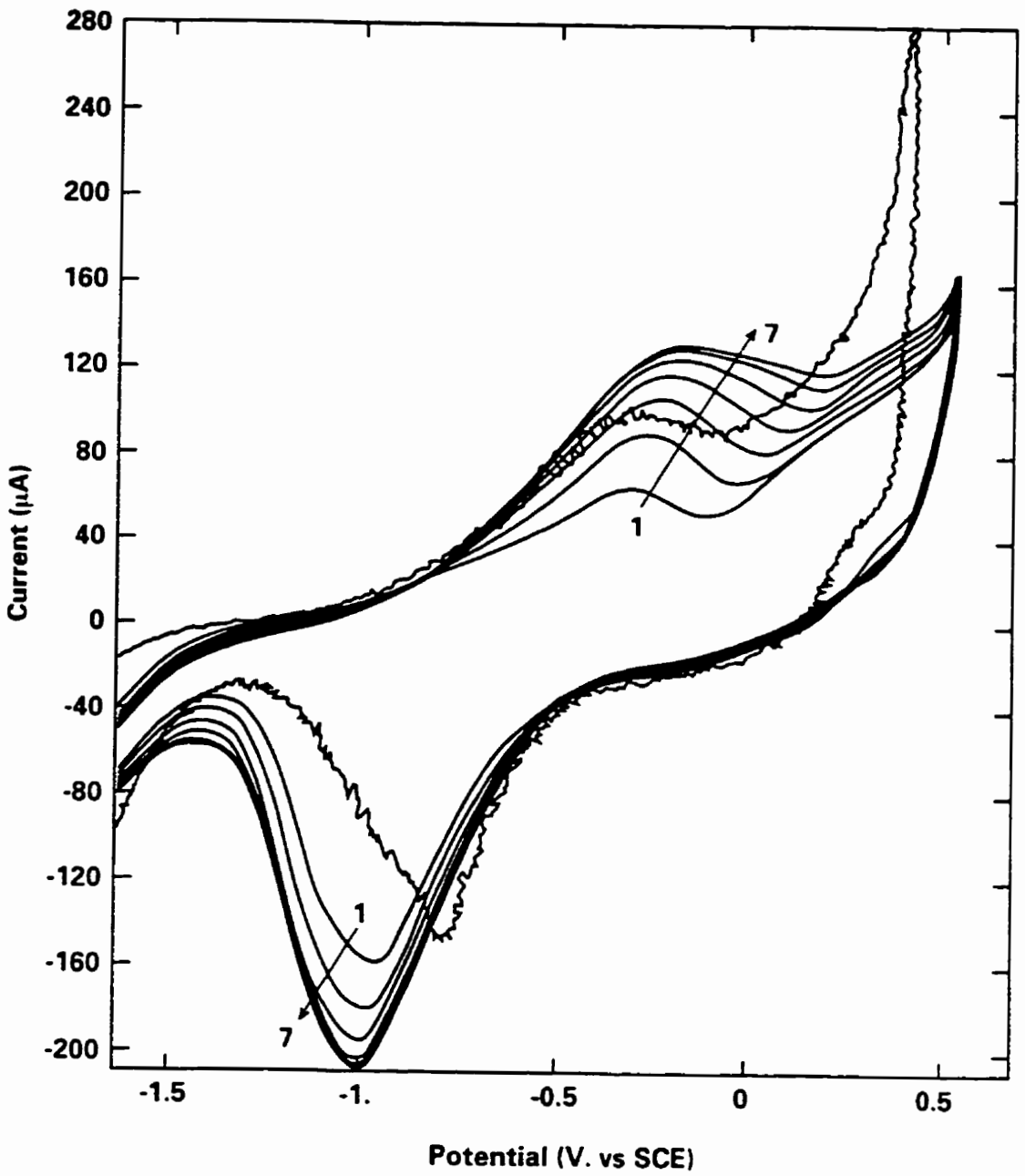

FIGURE 4.10: Comparison of CV's recorded at a scan rate of 10 $mV.s^{-1}$ to an anodic limit of 0.5 V in 0.1 $mol.L^{-1}$ $NaClO_4$ for (A) an IR compensated CV and (B) a non- IR compensated CV.

This provides clear evidence for the build up of resistive material at oxidized sites thought to be within grain boundaries. Consequently, a large portion of the applied potential is lost as IR drop across this material and only a small increase in potential occurs across the electrode/solution interface to drive the dissolution process. For such a resistance to build up it is likely that the depth of oxidation at reactive sites must be substantial. For this to be concentrated at grain boundaries, material at the grain boundary must be more readily oxidizable than observed for the L6 electrode.

The higher reactivity of J2 suggests a higher degree of non-stoichiometry within the grain boundaries compared to L6 (i.e. UO_{2+x} where x is larger for J2 than for L6). This could be a consequence of the difference in completeness of the reductive sintering process during fabrication.

Generally, for small degrees of non-stoichiometry, UO_{2+x} exhibits p-type conductivity (Section 2.2), but for a sufficiently large value of x, n-type behaviour is possible. Evidence to support this was observed by Hocking et al. [25]. They observed that the electronic properties of UO_{2+x} can accommodate cathodic and anodic photocurrents by changing the degree of hyperstoichiometry. While it is possible that the J2 electrode could possess n-type conductivity in the grain boundaries, a more extensive investigation, possibly involving photoelectrochemical measurements, is required to demonstrate this.

5.0 CYCLIC VOLTAMMETRY IN DIFFERENT SOLUTIONS

5.1 RESULTS

Figures 5.1 to 5.6 show CV's to eight different anodic potential limits (-0.8, -0.6, -0.4, -0.2, 0, 0.2, 0.3, 0.5 V) at a scan rate of 10 $mV.s^{-1}$ in six different solutions; 0.1 $mol.L^{-1}$ $NaClO_4$, SCSSS, 0.97 $mol.L^{-1}$ NaCl, 0.97 $mol.L^{-1}$ $CaCl_2$, 0.1 $mol.L^{-1}$ $NaClO_4$ + $5x10^{-4}$ $mol.L^{-1}$ SiO_4^{4-} and SCSSS + 10^{-2} $mol.L^{-1}$ HCO_3^-.

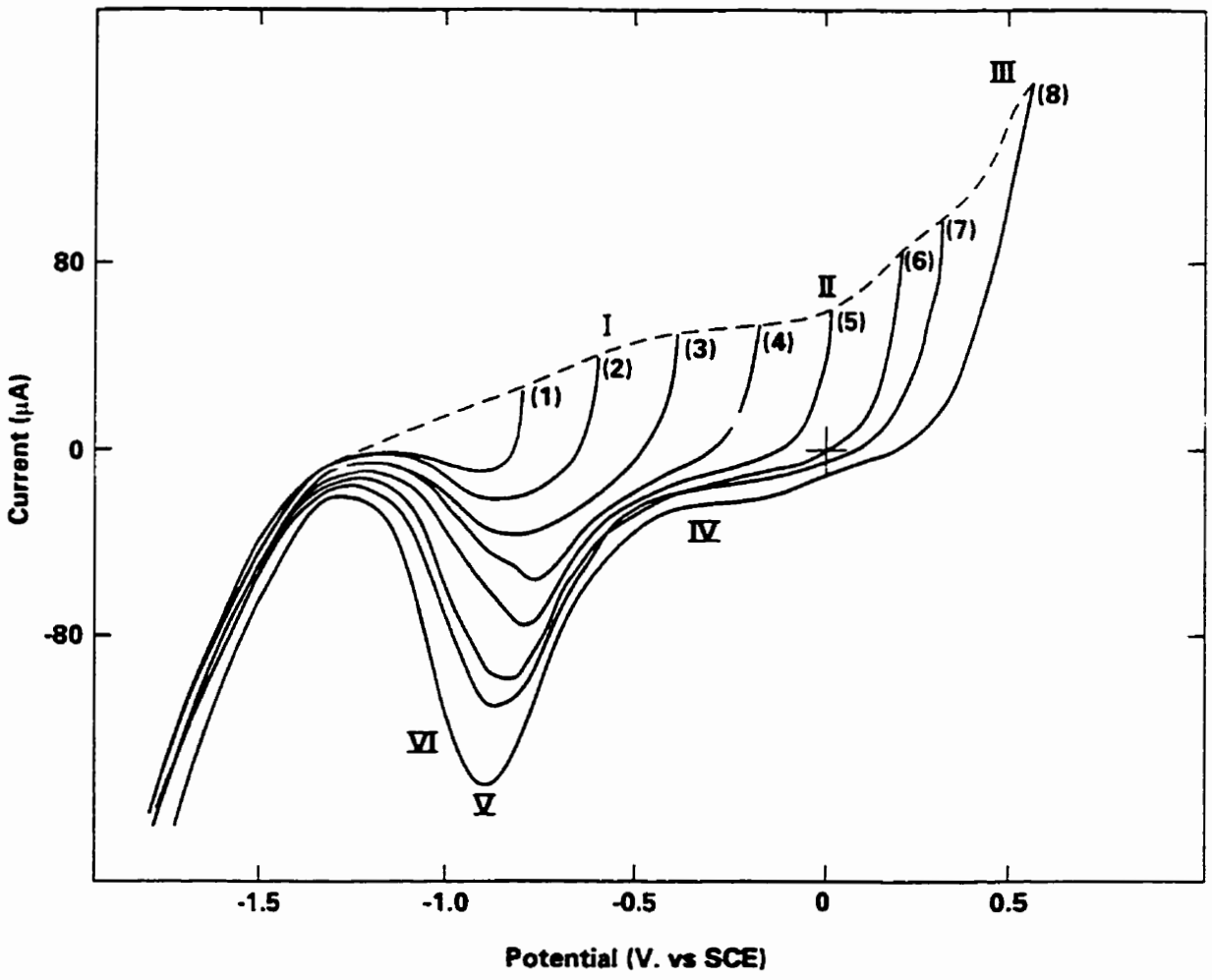

Figure 5.1: CV recorded at a scan rate of 10 $mV.s^{-1}$ to anodic potential limits of (1) -0.8V, (2) -0.6V, (3) -0.4V, (4) -0.2V, (5) 0V, (6) +0.2V, (7) +0.3V and (8) +0.5V in $NaClO_4$.

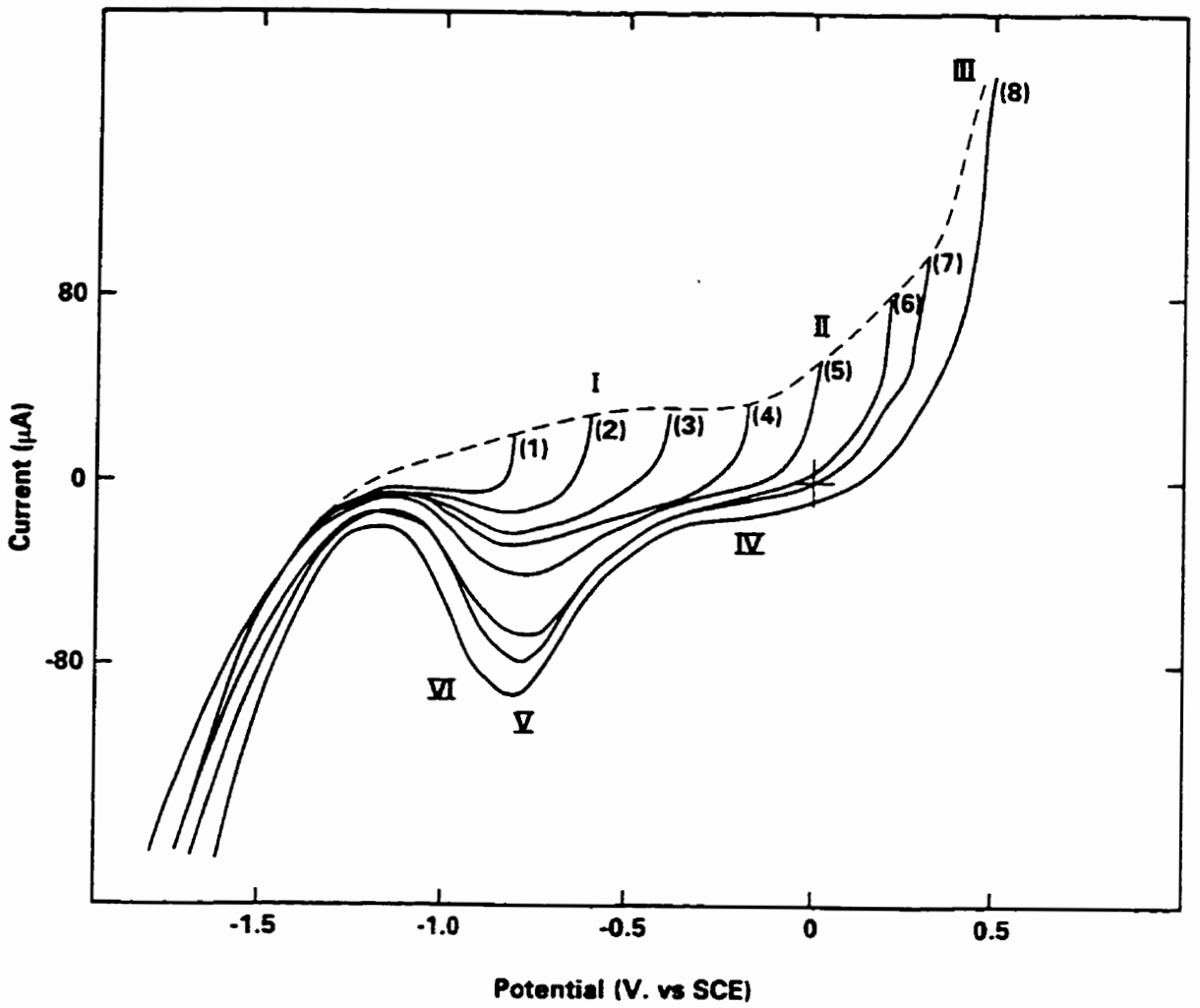

Figure 5.2: CV recorded at a scan rate of 10 $mV.s^{-1}$ to anodic potential limits of (1) -0.8 V, (2) -0.6 V, (3) -0.4 V, (4) -0.2 V, (5) 0 V, (6) +0.2 V, (7) +0.3 V and (8) +0.5 V in NaCl.

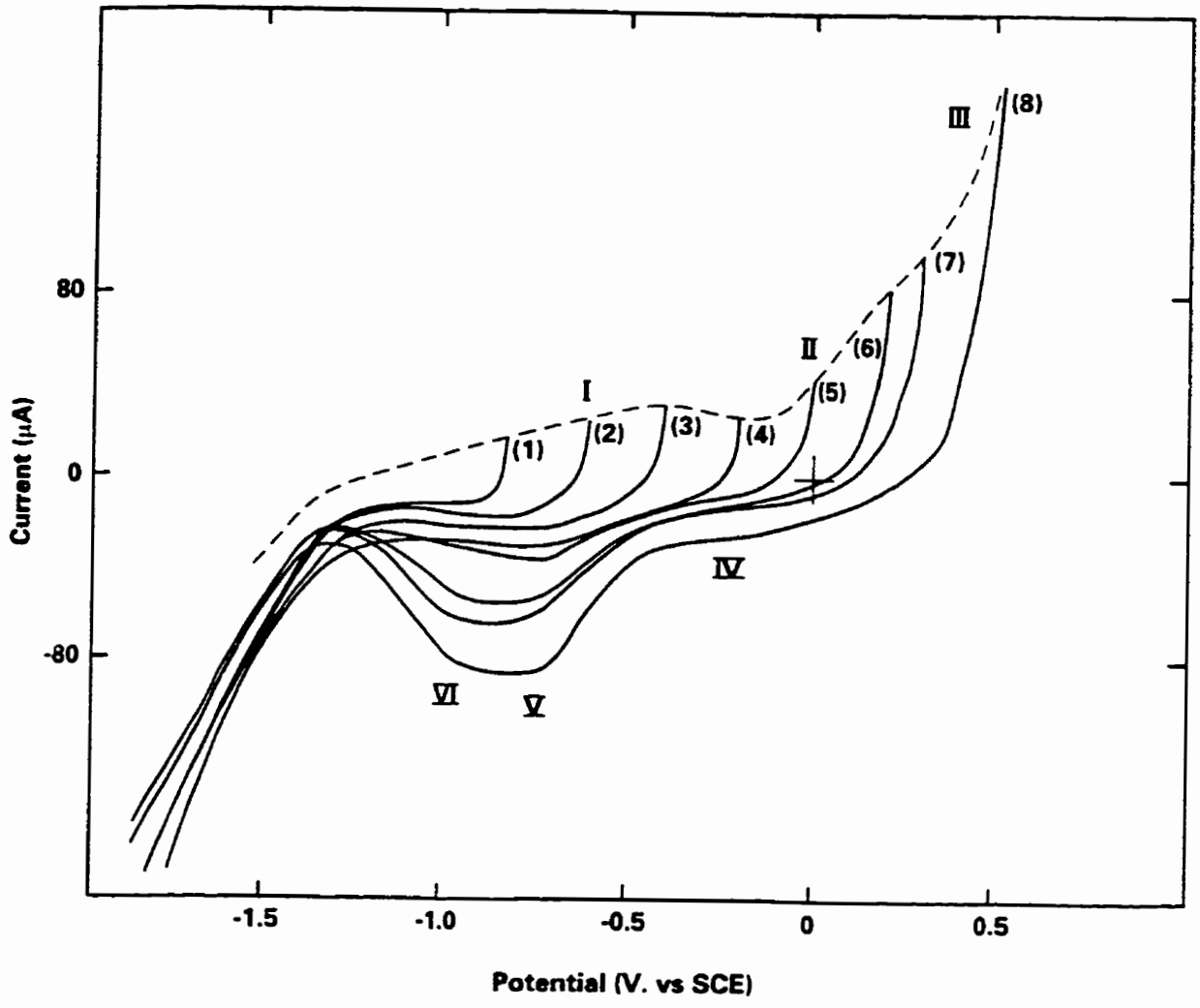

Figure 5.3: CV recorded at a scan rate of 10 $mV.s^{-1}$ to anodic potential limits of (1) -0.8 V, (2) -0.6 V, (3) -0.4 V, (4) -0.2 V, (5) 0 V, (6) +0.2 V, (7) +0.3 V and (8) +0.5 V in SCSSS.

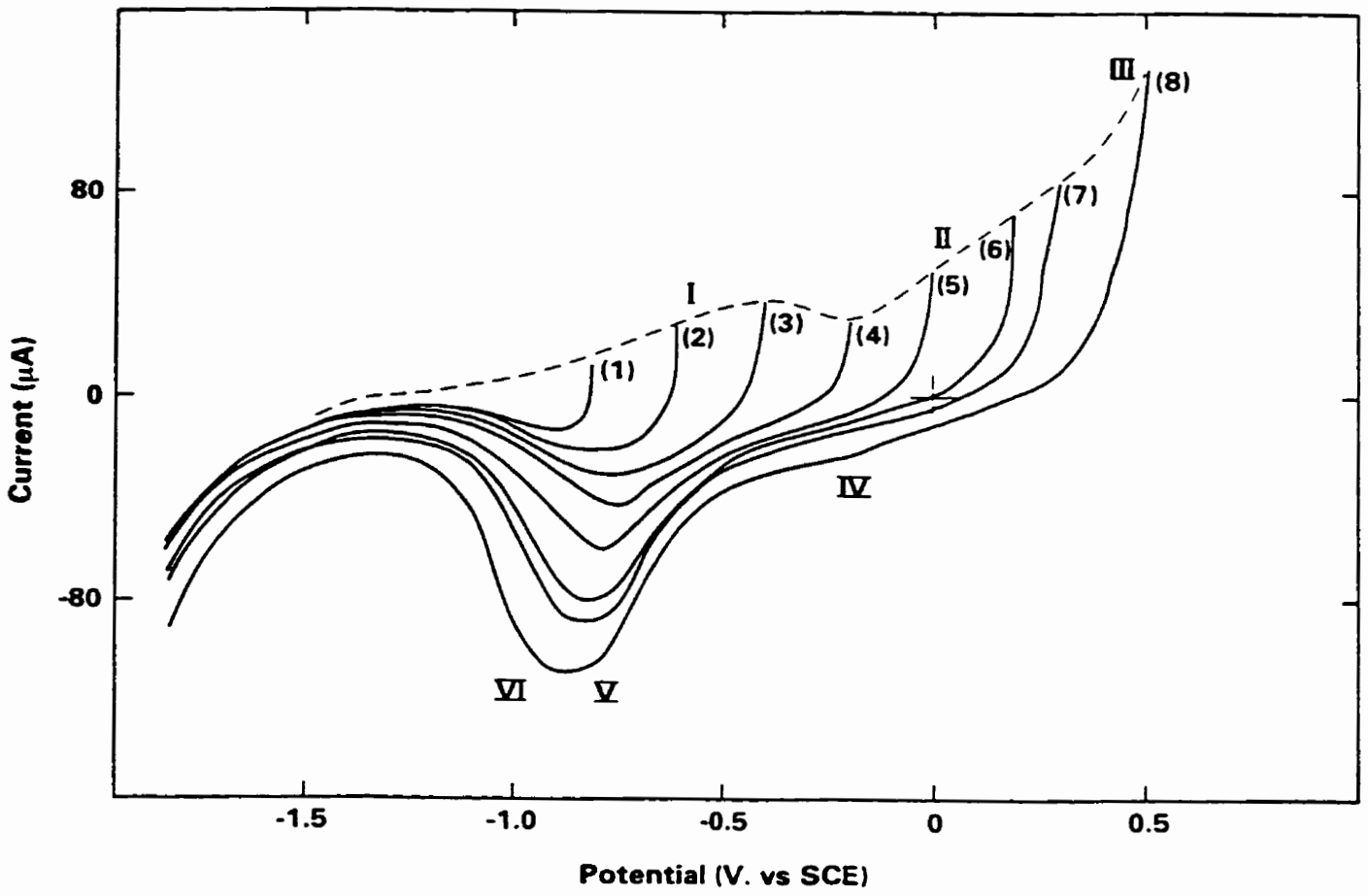

Figure 5.4: CV recorded at a scan rate of 10 $mV.s^{-1}$ to anodic potential limits of (1) -0.8 V, (2) -0.6 V, (3) -0.4 V, (4) -0.2 V, (5) 0 V, (6) +0.2 V, (7) +0.3 V and (8) +0.5 V in $NaClO_4$ + SiO_4^{4-}.

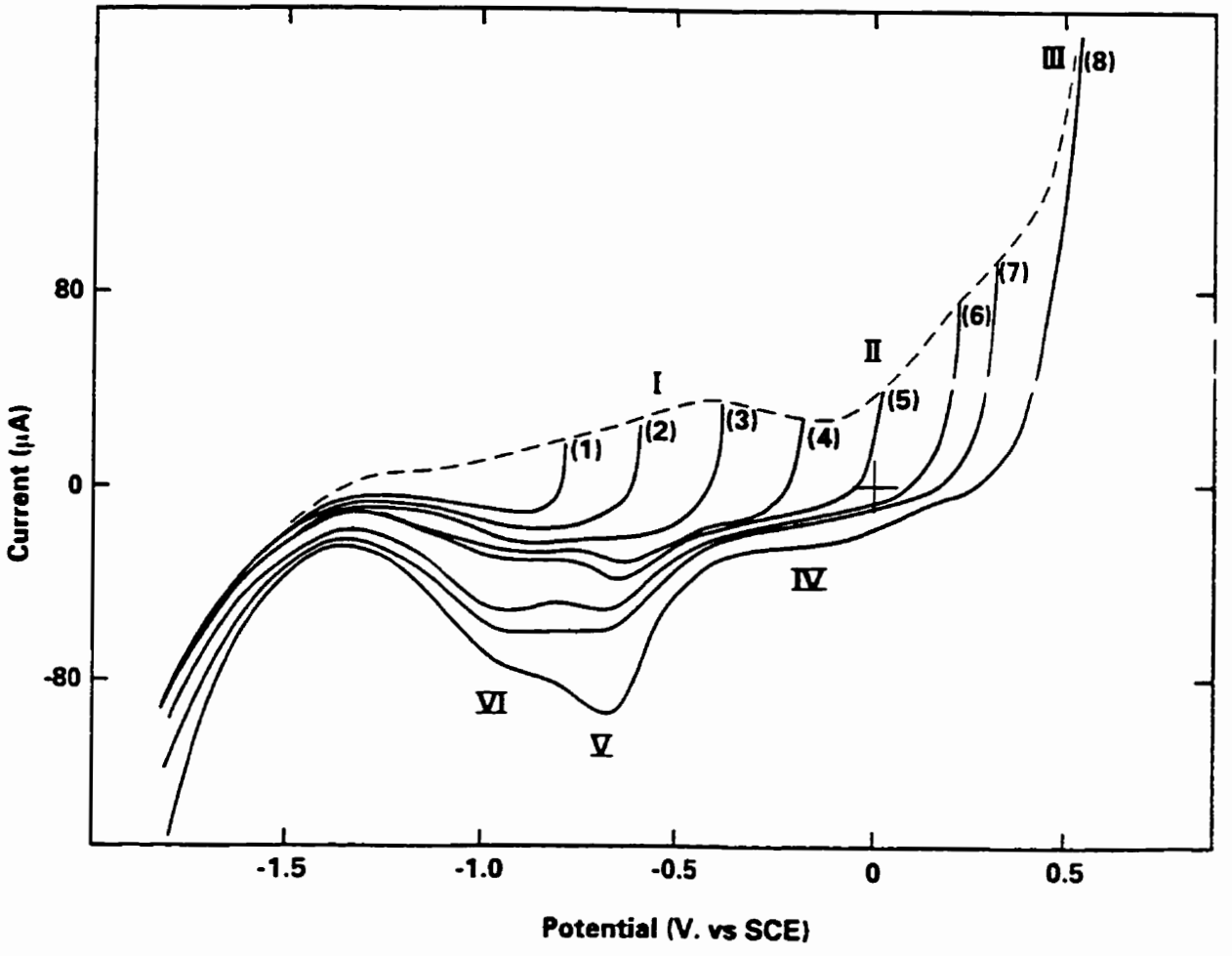

Figure 5.5: CV recorded at a scan rate of 10 $mV.s^{-1}$ to anodic potential limits of (1) -0.8 V, (2) -0.6 V, (3) -0.4 V, (4) -0.2 V, (5) 0 V, (6) +0.2 V, (7) +0.3 V and (8) +0.5 V in $CaCl_2$.

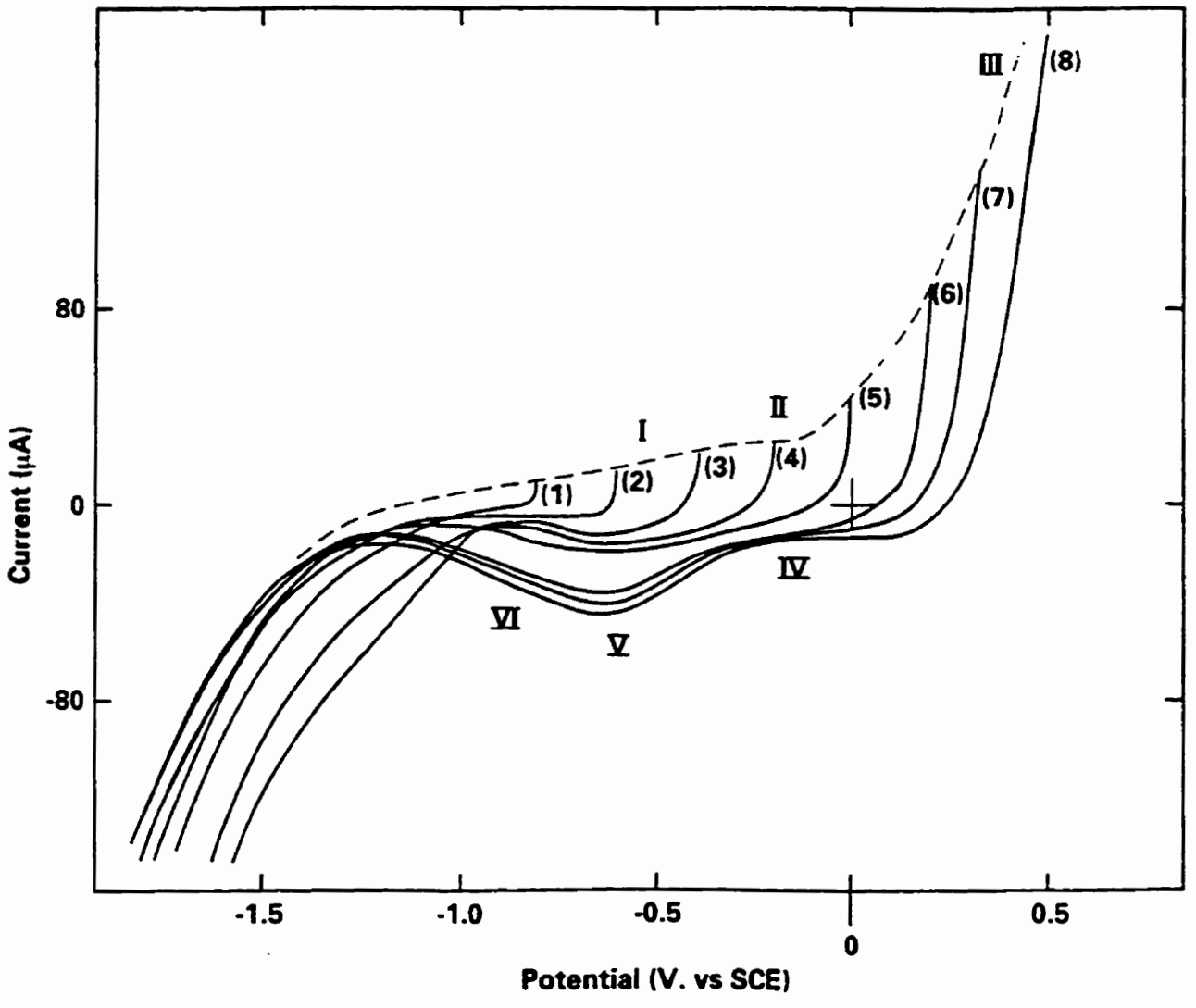

Figure 5.6: CV recorded at a scan rate of 10 $mV.s^{-1}$ to anodic potential limits of (1) -0.8 V, (2) -0.6 V, (3) -0.4 V, (4) -0.2 V, (5) 0 V, (6) +0.2 V, (7) +0.3 V and (8) +0.5 V in SCSSS + HCO_3^-.

For scans to the anodic limits of -0.8 and -0.6 V and back, except for the SCSSS + HCO_3^- solution, there is very little difference between all six solutions. In SCSSS + HCO_3^-, the oxidation and reduction peaks are suppressed.

For scans to -0.4V, the oxidation which occurs at peak I (Figure 2.8) has similar current values in the range of 25 to 30 μA for all solutions tested with the exception of the SCSSS + HCO_3^- solution which has a current of only 20 μA. There is only a single reduction peak between the potential range of -0.75 to -0.8 V observed for $NaClO_4$, NaCl and SiO_4^{4-}, with a current of ~-33 μA. For $CaCl_2$, two reduction peaks are visible (at ~ -0.65 V and ~ -0.85 V, Figure 5.5) with currents of -25 and -28 μA respectively. For SCSSS, no clearly defined peaks are visible, but the current is ~-25 μA over the potential range from -0.65 to -0.9 V. The reduction peak at -0.75 V (peak V) is suppressed in SCSSS + HCO_3^- with a current of 18 μA. For scans to -0.2 V, similar behaviour is observed and the separation into two peaks is even more clearly defined in $CaCl_2$.

For the scans to 0.2 V, the behaviour of $NaClO_4$, NaCl and SiO_4^{4-} is effectively the same, except the reduction peak in NaCl is slightly smaller (-85 μA) than that in $NaClO_4$ (-100 μA) and in SiO_4^{4-} (-95 μA). Apart from the separation of the reduction process into two peaks, the behaviour in $CaCl_2$ is the same as observed for $NaClO_4$. The reduction peak in SCSSS is smeared and not clearly separated into two peaks. In the SCSSS + HCO_3^- solution the oxidation and reduction peaks are suppressed, but are observed at roughly the same peak potentials as for $NaClO_4$.

At potentials > 0.2 V, the cathodic reduction peak V grows more rapidly

with increasing potential than peak VI in $CaCl_2$. For SCSSS two reduction peaks are now visible in the cathodic scan. Peak V appears to be growing more rapidly with increasing anodic limit than peak VI, but not as markedly as in $CaCl_2$. This compares to $NaClO_4$ in which peak V (at ~-0.7 V) is the only peak clearly discernible. For SiO_4^{4-} and NaCl, this peak is wider than for $NaClO_4$, but two distinct peaks are not visible in either solution. However, the shift in position of the reduction peak from ~-0.75 V to -0.85 V in SiO_4^{4-} indicates that a composite peak may be present rather than a single peak. For NaCl a slight shoulder is observed at ~-0.9 V on the backside of peak V. For SCSSS + HCO_3^-, there is only one peak at ~-0.7 V and it does not increase significantly in size with increasing anodic limit.

The rise in anodic current for potentials >0.4 V (ie. for potentials at which dissolution is expected to dominate) is in the order,

SCSSS + HCO_3^- > $NaClO_4$ ~ NaCl > SCSSS ~ $CaCl_2$ > SiO_4^{4-}

and the current values for area III at +0.5 V are given in Figure 5.7.

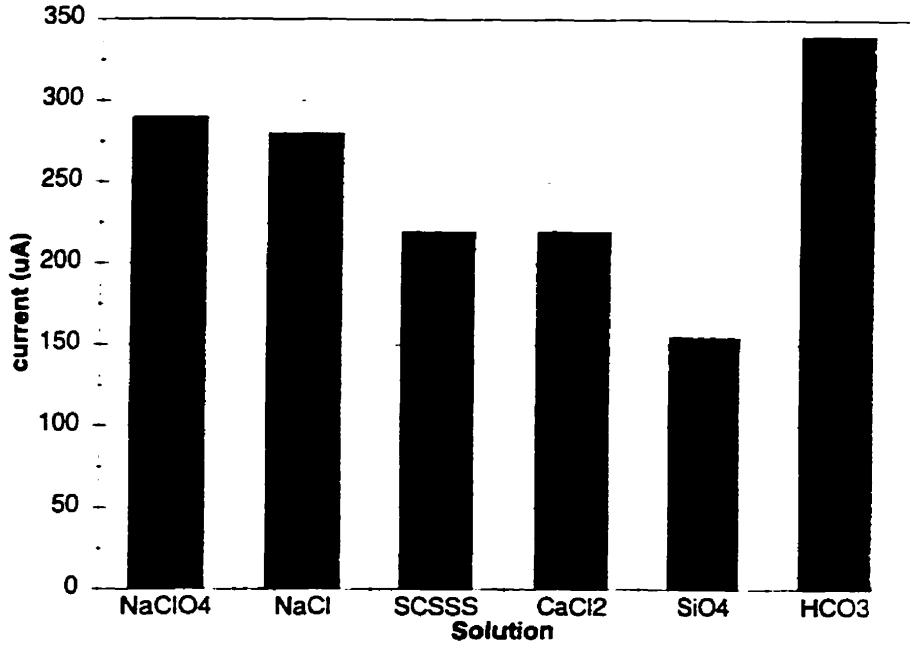

Figure 5.7: Peak current measured at an anodic potential limit of 0.5 V obtained in the CV's recorded in Figures 5.1 to 5.6.

The integrated areas under the reduction peaks (Qc) are shown in Figure 5.8 for all anodic potential limits. The amounts of dissolution (Qd), calculated using equation (3.3), are shown in Figure 5.9 for the anodic potential limits of 0.3 and 0.5 V, the only two limits for which these data were recorded.

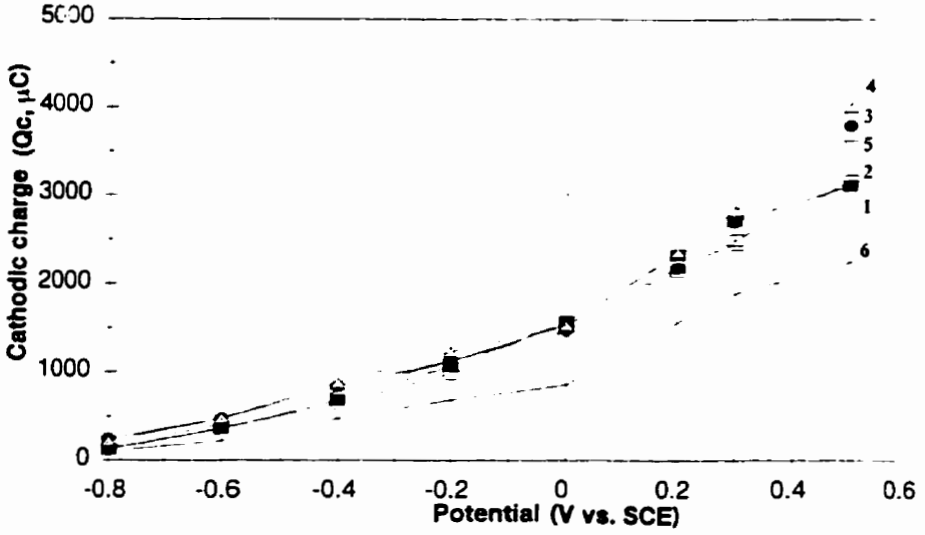

Figure 5.8: Cathodic charge (Qc) measured as a function of anodic potential limits recorded in the CV's for (1) $NaClO_4$ (2) NaCl (3) SCSSS (4) $CaCl_2$ (5) $NaClO_4$ + SiO_4^{4-} and (6) SCSSS + HCO_3^-.

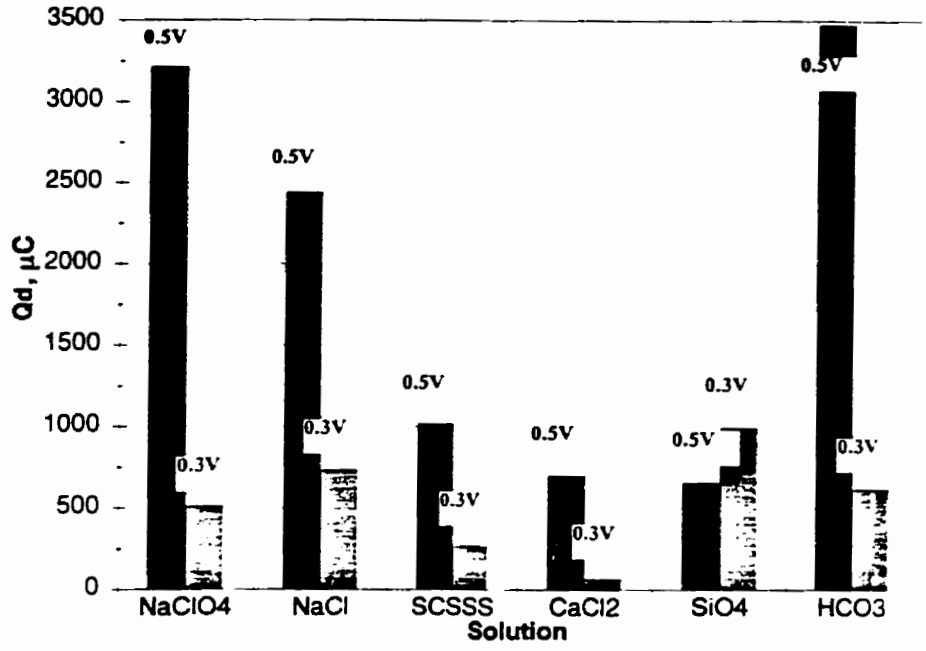

Figure 5.9: Comparison of the amount of dissolution (Qd) achieved after recording the CV's to anodic potential limits of 0.3 V and 0.5 V for the six solutions.

The Qd values for an anodic limit of 0.5 V are in the order,

$SCSSS + HCO_3^- > NaClO_4 > NaCl > SCSSS > CaCl_2 > SiO_4^{4-}$.

The Qd values for an anodic limit of 0.3 V are in the order,

$SiO_4^{4-} > NaCl > HCO_3^- > NaClO_4 > SCSSS > CaCl_2$.

The Qd values at 0.3 V are not as reliable as the Qd values at 0.5 V because the values at 0.3 V represent a small difference between two large numbers, Qa and Qc, whereas, at 0.5 V this difference is much larger.

For anodic limits, Ea, up to 0.3 V (Figure 5. 8) similar Qc values are obtained in all solutions except for the SCSSS + HCO_3^- solution. For a limit of 0.5 V there is similar behaviour for SCSSS, $CaCl_2$ and SiO_4^{4-} and lower, but similar values for $NaClO_4$ and NaCl. The value for SCSSS + HCO_3^- is much lower than the other solutions.

5.2 DISCUSSION

There is little apparent difference between all the solutions based on the anodic scans, except over the potential range from 0.3 to 0.5 V. From Figure 5.7, the currents in region III indicate that the behaviour is the same in $NaClO_4$ and NaCl solutions. In SCSSS, $CaCl_2$ and SiO_4^{4-} the currents in this region are lower while in SCSSS + HCO_3^- the current is higher than in $NaClO_4$ and NaCl.

All the solutions show the same basic behaviour in terms of anodic film growth. Three different stages of film growth can be observed by consideration of the plot of Qc versus Ea (Figure 5.8) and correlated with the stages observed on the anodic scan.

1. For scans to Ea $\leq$ 0.0 V, the value of Qc increases approximately linearly with the potential of the anodic limit (Ea). This corresponds to the anodic potential range (I) in which oxidation is thought to be at surface sites and/or in grain boundaries (i.e. $UO_{2+x} \rightarrow UO_{2.33}$ in Figure 2.7).

2. For 0.0 V < Ea < 0.3 V , Qc starts to increase more rapidly in all solutions. This increase correlates with the anodic potential range (II) where oxidation starts to penetrate more deeply into the UO_2 surface (i.e. $UO_2 \rightarrow UO_{2.33}$ in Figure 2.7).

3. For Ea > 0.3 V, Qc increases markedly in SCSSS, $CaCl_2$ and SiO_4^{4-}, increases much less for $NaClO_4$ and NaCl, and increases only slightly for SCSSS + HCO_3^-. This corresponds to the potential region (III) where dissolution as UO_2^{2+} is expected to dominate (Section 2.4.2).

The respective dissolution charges are consistent with this behaviour. The values of Qd for an anodic limit of 0.3 V are difficult to compare since they are relatively small differences between large quantities (Qa and Qc) and are likely to be affected by the inaccuracies and assumptions made in measuring Qa and Qc. The Qd values for Ea = 0.5 V are comparable to the Qc values and therefore, likely to be much more significant.

A more detailed discussion of the voltammetric behaviour for each solution is given below.

<u>$NaClO_4$</u>

The voltammetric behaviour in $NaClO_4$ (Figure 5.1) to all eight anodic limits is consistent with previously published observations [63] and will be treated as the standard behaviour for non-complexing solutions against which the behaviour of all other solutions can be compared.

For Ea ≤ 0.0 V (region I), the reduction peak increases in size with increasing Ea in the same linear fashion that Qc increases (Figures 5.1 and 5.8).

The reduction peak recorded after scans to anodic potential limits of -0.2 and 0.0 V occurs at ~-0.65 V and has previously been designated peak V and attributed to the reduction of, $UO_{2.33} \rightarrow UO_{2+x}$ (Figure 2.7). Thus, in this region, Qc is a measure of the increase in extent of oxidation to $UO_{2.33}$ with increasing anodic limit.

For the potential range 0.0 V < Ea < 0.3 V (region II) oxidation starts to penetrate more deeply into the surface of the UO_2 matrix. The reduction peak V continues to increase and starts to shift from -0.65 V to -0.7 V which may be attributed to thickening of the film of $UO_{2.33}$ with increasing Ea. This coincides with the increase in slope in the Qc versus Ea plot (Figure 5.8) which confirms that the extent of film growth increases with increasing Ea.

For Ea ≥ 0.3 V (region III), dissolution as UO_2^{2+} becomes the predominant oxidation process, as indicated by the increase in current in this region, and the Qc versus Ea plot which has a shallower slope than at lower potentials. However, the slope is still positive confirming that film growth is still occurring, thereby accounting for the increase in height of the reduction peak V at ~ -0.7 V.

NaCl

Anions, such as Cl^-, are expected to have a minimal effect on complexation of UO_2^{2+} (Section 2.4.6.2) and hence are not expected to affect dissolution. As observed, the CV's in NaCl (Figure 5.2) are expected to behave in a similar manner to those for $NaClO_4$ (Figure 5.1)

The plot of Qc versus Ea in NaCl (Figure 5.8) is very similar to that for

$NaClO_4$ over the entire potential range indicating that the amount of film growth as $UO_{2.33}$ is approximately the same. However, the voltammetric reduction behaviour for Ea ≥ 0.2 V, in which the current at peak V is lower and wider in NaCl than in $NaClO_4$ is evidence that the film formation process is affected slightly by Cl^-.

From the proposed mechanism for oxidative dissolution of UO_2 (Section 2.4.5) there are two reaction pathways that may be followed. The first pathway would follow equations 2.2 and 2.3 in which uranyl ions are incorporated into a precipitated phase

$$UO_{2.33} \rightarrow (UO_2^{2+})_{ads} \rightarrow UO_3.2H_2O \qquad (5.1)$$

while the second path involves the rapid production of UO_2^{2+} followed by extensive dissolution,

$$UO_{2.33} \rightarrow (UO_2^{2+})_{ads} \rightarrow UO_2^{2+}{}_{(bulk\ solution)} \qquad (5.2)$$

If the second pathway predominated in NaCl, the Qd value at +0.5 V, would be larger in NaCl than in $NaClO_4$. Since it is lower in NaCl than in $NaClO_4$ (Figure 5.9) the second pathway is less prominent.

Alternatively, the first pathway results in the formation of $UO_3.2H_2O$, which could suppress dissolution and, hence, lead to an increase in Qc, but a decrease in Qd. However, Qc remains the same, which indicates that the amount of film growth does not increase in NaCl compared to $NaClO_4$. The broadening of the reduction peak and the appearance of a shoulder on the negative side of the peak at ~-0.65 V (Figure 5.2) suggests less $UO_{2.33}$ and more $UO_3.2H_2O$ forms in NaCl than in $NaClO_4$. However, the effect is not large. While this may suggest

that the oxidation /dissolution/ reprecipitation process is more extensive in NaCl, the effect is minor.

SCSSS, $CaCl_2$, SiO_4^{4-}

The UO_2 surface can be thought of as composed of two kinds of sites. The first are UO_{2+x} sites which are either distributed generally across the surface, possibly as a consequence of the polishing process, or located in grain boundaries as a consequence of the reductive sintering process. The second are UO_2 sites which are unaffected by preparation or fully reduced in the sintering process.

When oxidation of the surface occurs, U^{4+} sites are converted to U^{6+} and, in regions I and II become incorporated into the UO_{2+x} layer as it thickens with increasingly positive potential.

In SCSSS (Figure 5.3), or solutions containing species expected to stabilize U^{VI} solids (i.e. SiO_4^{4-}, Ca^{2+} in Figures 5.4 and 5.5), the formation of UO_{2+x} (on its way to $UO_{2.33}$) may not occur, but the U^{VI} species would be extracted and incorporated into a more stable U^{VI} solid. This could account for the dual reduction peaks formed in $CaCl_2$ after scanning across the low potential region ($Ea \leq 0.0$ V), Figure 5.5. To a less obvious degree, similar behaviour is observed in SCSSS.

By comparison to $NaClO_4$, the growth of $UO_{2.33}$ is retarded in SCSSS. This is clear from the reduction in size of peak V at ~-0.7 V (compare Figures 5.1and 5.3). However, for $Ea \leq 0.2$ V, Qc as a function of Ea is approximately

the same in both solutions, Figure 5.8, indicating that, while the amount of $UO_{2.33}$ formed may be lower, the amount of reprecipitated U^{VI} solid (reduced at peak VI) is higher. The increase in Qc at Ea = 0.5 V (Figure 5.8) can be attributed predominantly to an increase in the amount of the U^{VI} phase reduced at -0.9 V (peak VI) in Figure 5.3.

Both the inhibition of $UO_{2.33}$ formation and the enhancement of the U^{VI} phase formation are accompanied by a decrease in Qd (Figure 5.9), the amount of dissolution. This suggests that the U^{VI} phase is responsible for blocking both $UO_{2.33}$ formation and UO_2^{2+} dissolution.

All three solutions (SCSSS, $CaCl_2$, SiO_4^{4-}) which show a large increase in Qc for Ea = 0.5 V (Figure 5.8), also show a suppression of Qd (Figure 5.9). This suppression is more distinct for the SCSSS constituents (Ca and Si) than it is for SCSSS itself. Also, the current values in the potential region III are similar for all three solutions, and significantly lower than for $NaClO_4$, Figure 5.7.

The relative sizes of the two reduction peaks (V and VI) are similar for SCSSS and $CaCl_2$. By comparison, the reduction peak present in SiO_4^{4-} is more like the single peak observed in $NaClO_4$. However, the peak is wider and is observed at a more negative potential for SiO_4^{4-} than that for $NaClO_4$ (compare Figure 5.1 and 5.4) indicating that a composite peak due to the reduction of both $UO_{2.33}$ and a U^{VI} precipitated phase may be present.

Previous experiments by Wilson and Gray [85] demonstrated that Ca and Si ions in solution decreased the dissolution rate of UO_2. Auger analysis of the UO_2 surface showed a 5 to 10 μm layer which contained Ca and Si, which was

assumed to block the dissolution. This layer appeared to be strongly adsorbed on the UO_2 surface since subsequent leaching in distilled deionized water did not remove the blocking effect.

The above observations and the results of this thesis, suggest both silicate and calcium can suppress dissolution by incorporation into an insoluble U^{VI} phase. While this phase can be electrochemically reduced at sufficiently negative potentials, its chemical dissolution is extremely slow. The possible solid phases are shown in Figure 2.10.

The Effect of HCO_3^-

For the SCSSS + $NaHCO_3$ solution, the overall suppression of the CV (Figure 5.6) is partly due to a difference in pH, and care should be taken in making a direct comparison with the other solutions.

Previous studies (Section 2.4.6.2) have observed that carbonate accelerates the dissolution of UO_2 , but that the early stages of oxidation, up to $UO_{2.33}$, are not affected in neutral to alkaline solutions. The acceleration of the dissolution by carbonate solutions is due partly to a thermodynamic effect in which the dissolution product, UO_2^{2+} is stabilized by complexation with the carbonate or the bicarbonate anion (Section 2.4.6.2).

The behaviour of Qc as a function of Ea is similar in the presence of bicarbonate as it is in $NaClO_4$, except that the values are lower over the entire potential range (Figure 5.8). Also, when the anodic scans in SCSSS + HCO_3^- (Figure 5.6) and $NaClO_4$ (Figure 5.1) are compared, SCSSS + HCO_3^- appears to

suppress anodic oxidation in the low potential range, region I (Ea ≤ 0.0 V). However, previous results indicate that this suppression is due predominantly to the lower pH not the presence of HCO_3^- (Figure 5.10).

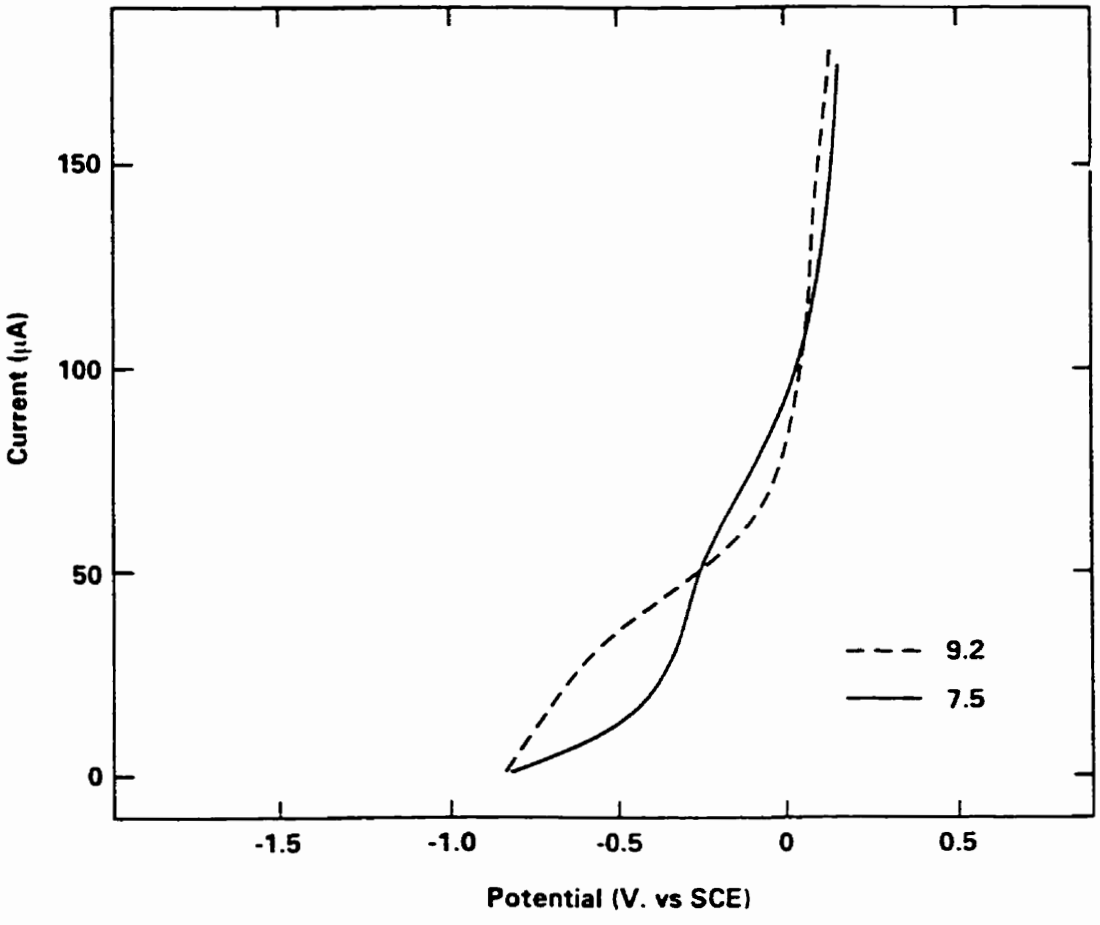

Figure 5.10: Anodic currents recorded after scanning to an anodic potential limit of 0.3 V in pH 7.5 in HCO_3^- and pH 9.2 in HCO_3^-.

The increase in the current in region III (Figure 5.6) for Ea > 0.2 V is a clear indication that dissolution as UO_2^{2+} is accelerated by the presence of HCO_3^-. This is confirmed by a high value of Qd in Figure 5. 9 (i.e. more dissolution) and a low value of Qc in Figure 5.8 (i.e. less film growth). The fact that $(Qd)_{HCO3-}$ is not that much > $(Qd)_{ClO4-}$ is due to the limited time that Ea ≥ 0.3 V. This difference is much more noticeable after longer potentiostatic oxidations and will be discussed below in Chapter 7.

The position of the reduction peak at -0.7V in Figure 5.6 on the reverse cathodic scan is consistent with the reduction of $UO_{2.33}$ to UO_{2+x}. The absence of a significant reduction peak for U^{VI} solids supports the claim that all the UO_2^{2+} produced is dissolved into the solution by complexation with HCO_3^-. Consequently, the presence of bicarbonate in SCSSS prevents the blocking of oxidative dissolution of UO_2 observed in SCSSS alone.

6.0 X-RAY PHOTOELECTRON SPECTROSCOPY (XPS)

6.1 RESULTS

6.1.1 Logarithmic Current - time plots

Figures 6.1and 6.2 show the current - time plots recorded at the anodic potentials of 0.1 V and 0.5 V for the ZR3 electrode in the $NaClO_4$, NaCl and SCSSS solutions. The final current after 20 hours at the potential value of 0.1 V, is a factor of 10 lower in SCSSS and a factor of 2 higher in NaCl compared to that for $NaClO_4$. At the anodic potential of 0.5 V, the currents are similar for all three solutions.

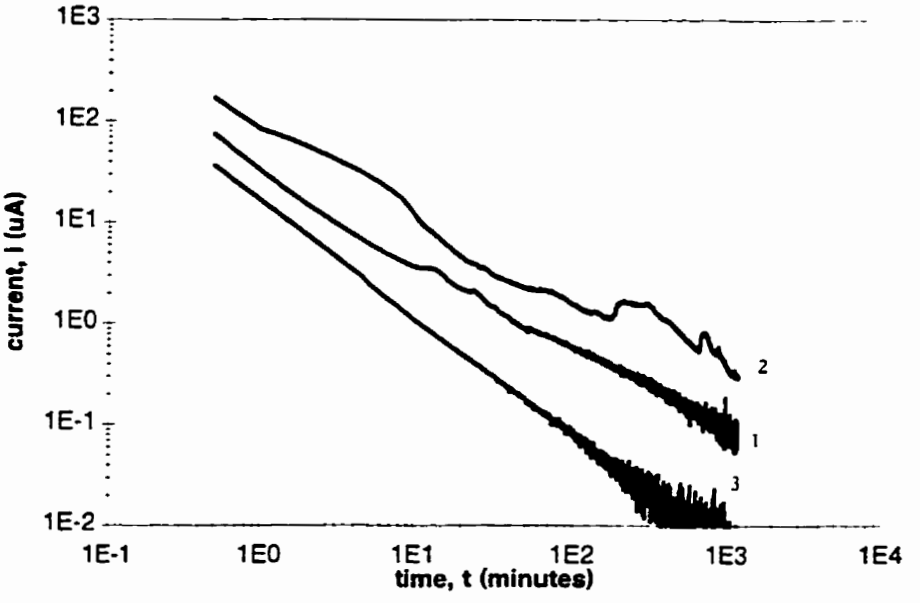

FIGURE 6.1: Plot of current as a function of time for anodic oxidation at 0.1 V for 20 hours in (1) $NaClO_4$, (2) NaCl and (3) SCSSS.

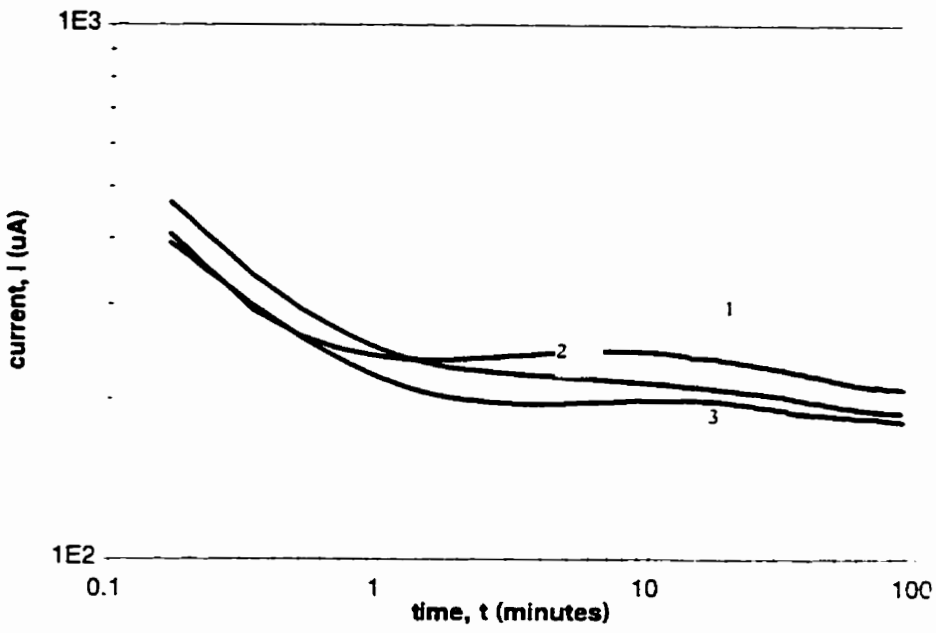

FIGURE 6.2: Plot of the current as a function of time for anodic oxidation at 0.5 V for 1.5 hours in (1) $NaClO_4$, (2) NaCl and (3) SCSSS.

6.1.2 XPS

Examination of the ZR3 electrode by XPS was performed following the anodic oxidations described above. The XPS survey spectrum for the number of electrons ejected as a function of the electron binding energy recorded after anodic oxidation at 0.5 V in SCSSS is shown in Figure 6.3. As discussed in Section 3.5.1, uranium forms a large number of oxides with intermediate stoichiometries between UO_2 and UO_3 containing both U(IV) and U(VI). The band at ~380 eV, due to the $4f_{7/2}$ electrons, was used to monitor the chemical state of uranium atoms. In mixed uranium oxides this band can be resolved into

the U(IV) and U(VI) components to obtain quantitative information about the relative amounts of each oxidation state present in the UO_2 electrode surface (Section 3.5.1).

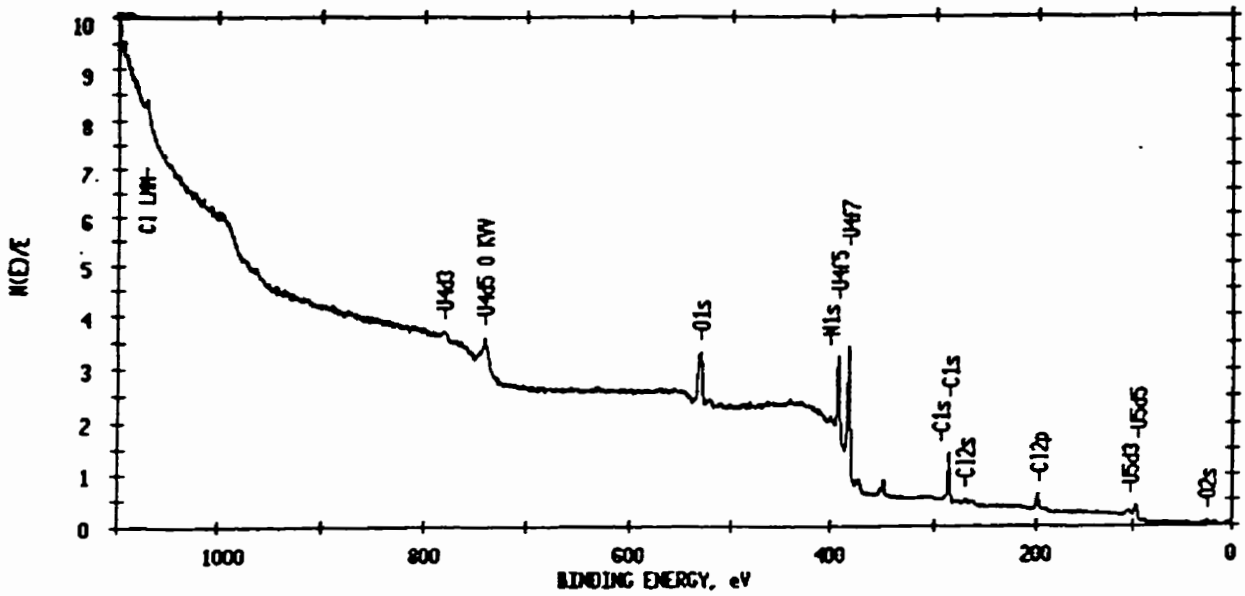

FIGURE 6.3: XPS survey spectrum recorded on the ZR3 electrode after anodic oxidation at 0.5 V for 1.5 hours in SCSSS.

As discussed in Section 2.4.6.2, the two species present in SCSSS that could stabilize U^{VI} solids are Ca^{2+} and SiO_4^{4-}. The Ca 2p and Si 2s binding energies are 346 eV for calcium and 154 eV for silicon. Therefore, Figures 6.4 and 6.5 show the XPS spectra from Figure 6.3 (i.e. 0.5 V for 1.5 hours) in more detail, for binding energies in the range from 360 to 340 eV for calcium and from 170 to 140 eV for silicon to quantify the relative amounts of each species present. The % concentrations of Ca and Si ions present were estimated from

the peak areas and were 3. 8 % and 0.46 %, respectively. Figures 6.6 and 6.7 show the XPS spectra recorded after anodic oxidation for 20 hours at a potential of 0.1 V in SCSSS. The % concentration of calcium and silicon ions were 2.4 % and 10.2 %, respectively.

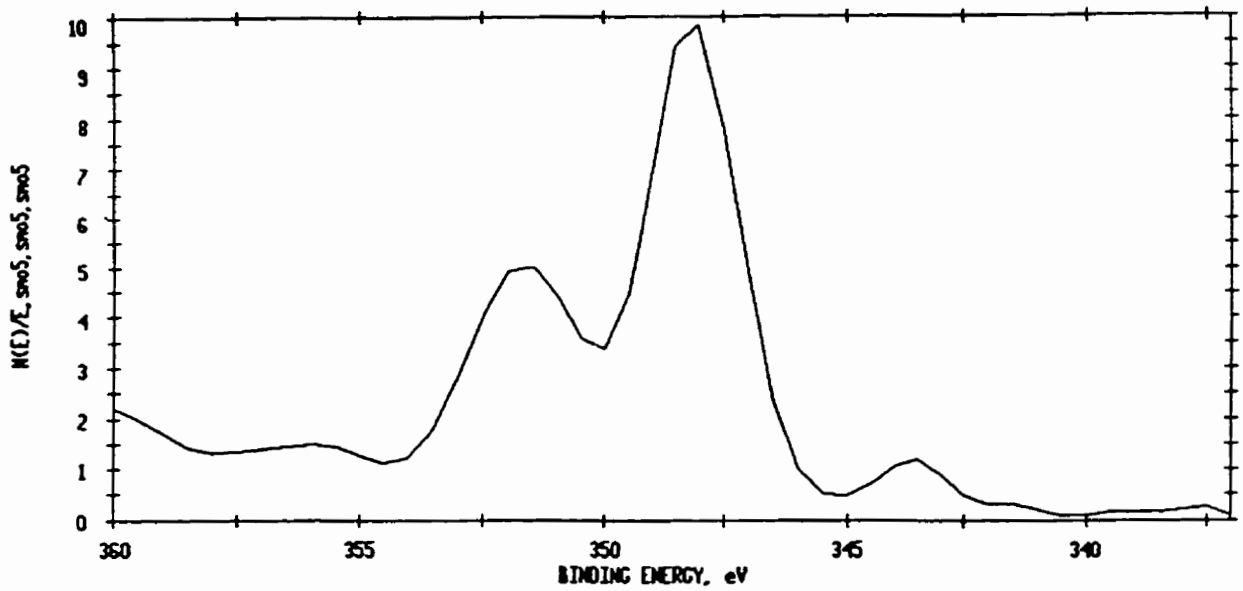

FIGURE 6.4: A section of the XPS spectrum recorded on the ZR3 electrode after anodic oxidation at 0.5 V for 1.5 hours in SCSSS. The peak at 348 eV is the Ca 2p peak.

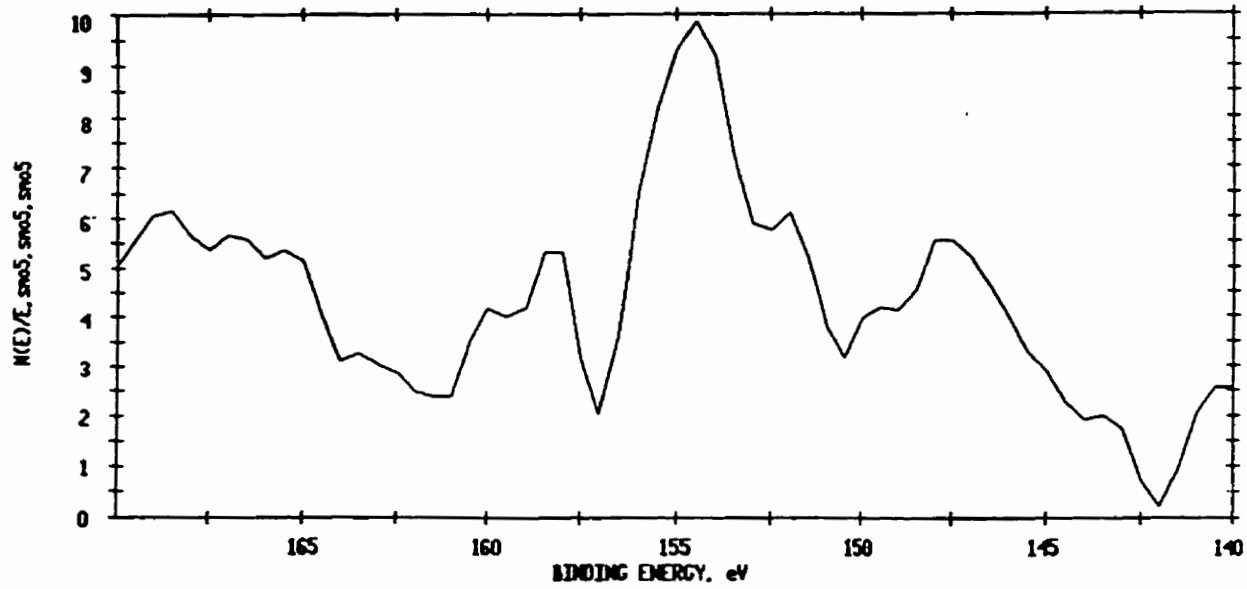

FIGURE 6.5: A section of the XPS spectrum recorded on the ZR3 electrode after anodic oxidation at 0.5 V for 1.5 hours in SCSSS. The peak at 154 eV is the Si 2s peak.

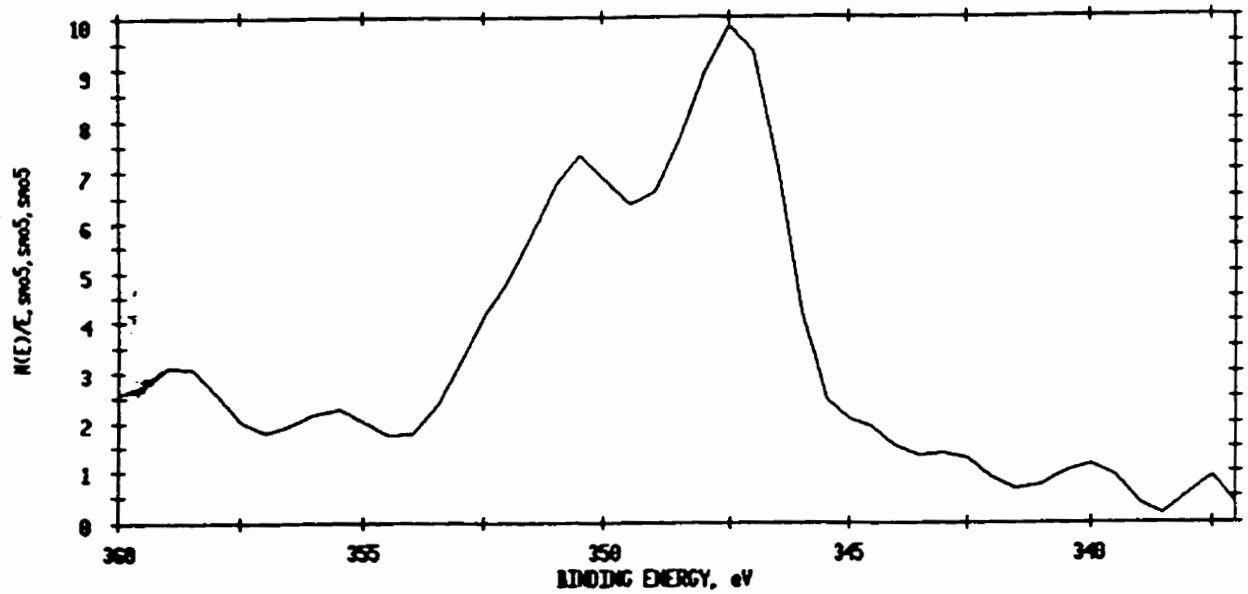

FIGURE 6.6: A section of the XPS spectrum recorded on the ZR3 electrode after anodic oxidation at 0.1 V for 20 hours in SCSSS. The peak at 348 eV is the Ca 2p peak.

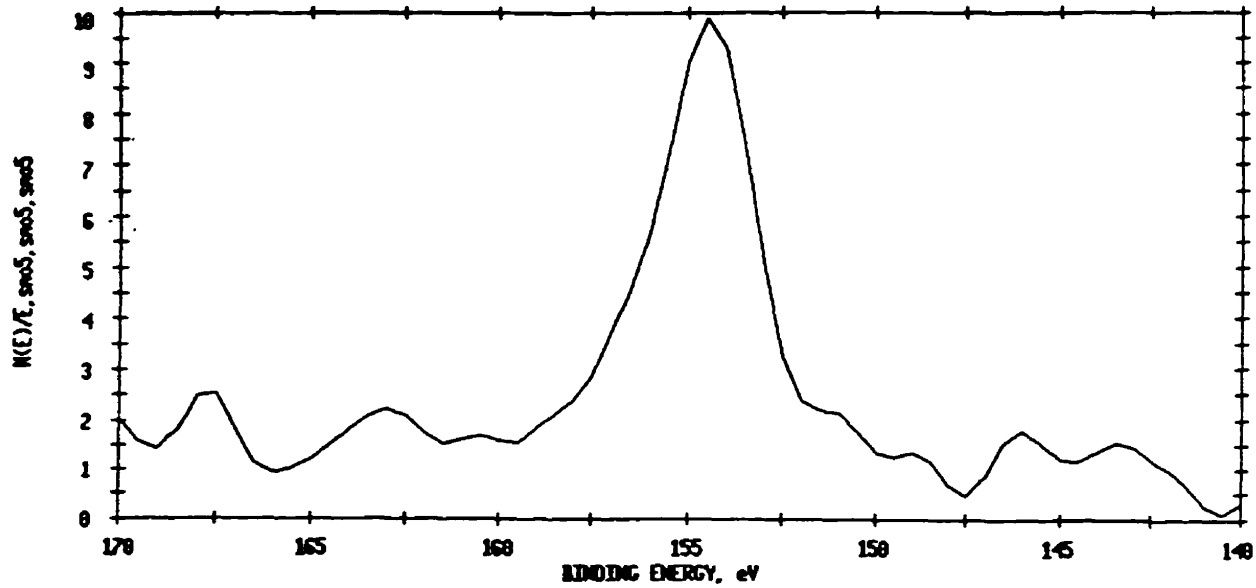

FIGURE 6.7: A section of the XPS spectrum recorded on the ZR3 electrode after anodic oxidation at 0.1 V for 20 hours in SCSSS. The peak at 154 eV is the Si 2s peak.

A valence band (VB) spectrum for the number of electrons ejected as a function of electron binding energy for a UO_2 surface after anodic oxidation at 0.5 V for 1.5 hours in SCSSS is shown in Figure 6.8. This spectrum is sensitive to the degree of oxidation. Area A corresponds to the O 2p region and Area B to the U 5f region. The relative sizes of the U 5f and O 2p peaks are used as qualitative indicators to show that the surface has undergone oxidation, since U 5f decreases and O 2p increases with oxidation (Section 3.5.1).

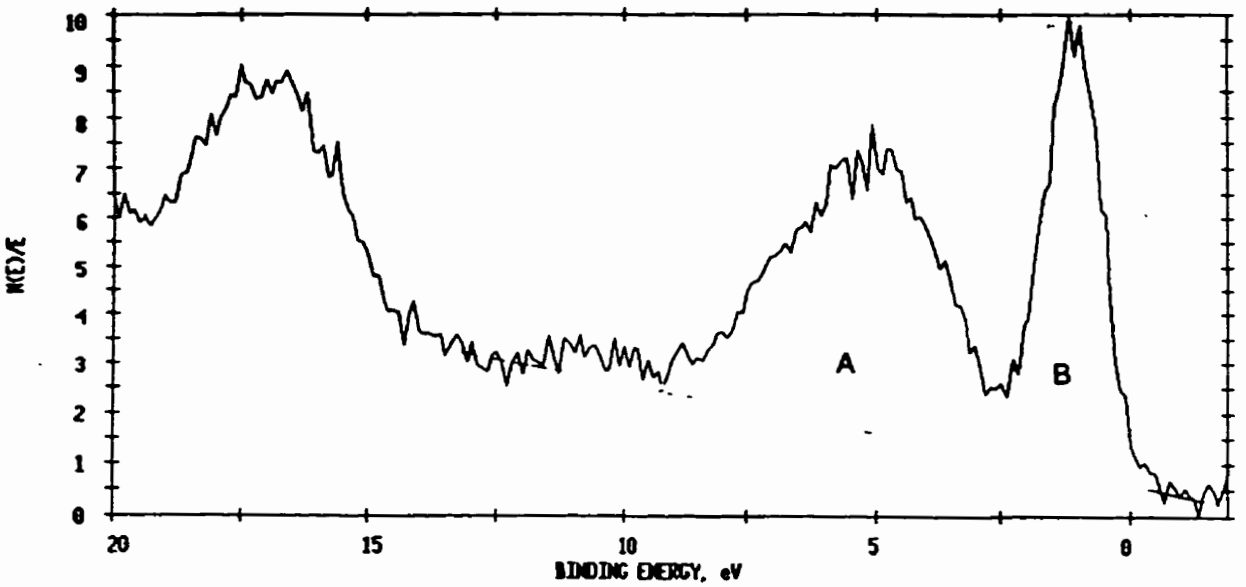

FIGURE 6.8: The valence band spectrum for UO_2 recorded for the ZR3 electrode after anodic oxidation at 0.5 V for 1.5 hours in SCSSS.

The $U4f_{7/2}$ spectrum for a UO_2 surface after reduction at -2.0 V for 5 minutes is shown in Figure 6.9 and can be compared with the spectrum recorded after anodic oxidation at 0.5 V for 1.5 hours in SCSSS shown in Figure 6.10. By using a least squares curve fitting routine, as described in Section 3.5.1, the two peaks can be separated into contributions from U^{6+} and U^{4+}. The area under Peak A shows the amount of U^{VI} present compared to the amount of U^{IV} present determined from the area under Peak B. As the surface becomes more oxidized, the area under Peak A increases in proportion to the decrease in the area under Peak B.

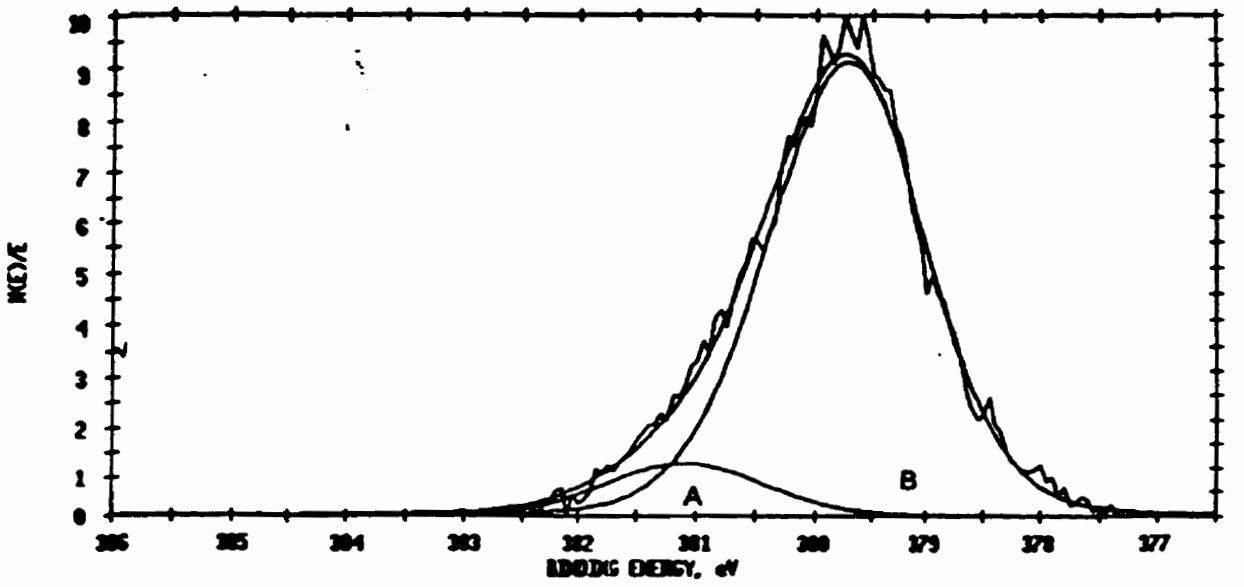

FIGURE 6.9: Resolution of the $U4f_{7/2}$ band used to determine the relative amounts of U(VI) (peak A) and U(IV) (peak B) in the surface of the ZR3 electrode after reduction at -2.0 V for 5 minutes in SCSSS.

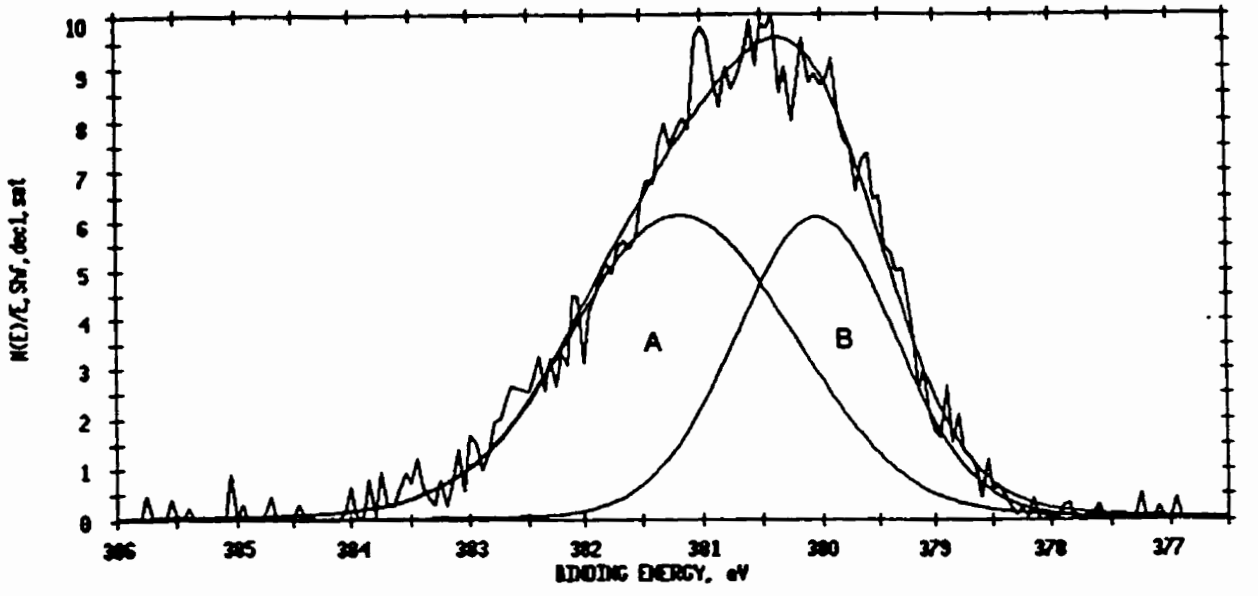

FIGURE 6.10: Resolution of the $U4_{7/2}$ band used to determine the relative amounts of U(VI) (peak A) and U(IV) (peak B) in the surface of the ZR3 electrode after anodic oxidation at 0.5 V for 1.5 hours in SCSSS.

Table 6.1 gives the values of U^{VI}:U^{IV} ratio and the amounts of Ca and Si obtained after oxidation in $NaClO_4$, NaCl and SCSSS solutions at the two anodic potentials (0.1 V and 0.5 V) over the two time intervals (20 hours and 1.5 hours).

Table 6.1

U^{VI}:U^{IV} ratio and the amounts of Ca and Si present after oxidation at 0.1 V and 0.5 V in $NaClO_4$, NaCl and SCSSS

Experiment	U6/4 ratio	Calcium %	Silicon %
0.1 V for 20 h			
$NaClO_4$	3.07		
NaCl	4.16		
SCSSS	0.56	2.4	10.2
0.5 V for 1.5 h			
$NaClO_4$	1.25		
NaCl	1.35		
SCSSS	1.36	3.8	0.46

6.2 DISCUSSION

After anodic oxidation in $NaClO_4$ at a potential of 0.1 V for a duration of 20 hours, the U^{VI}:U^{IV} ratio indicates that the surface layer has a high U^{VI} content, suggesting the presence of $UO_3.2H_2O$ [86]. The $UO_3.2H_2O$ may be localized with a $UO_{2.33}$ layer underneath. Evidence to support this is observed in the CSV after anodic oxidation for 18.5 hours (Figure 6.11) [87]. Figure 6.11 has a broad reduction peak incorporating both Peaks V and VI (defined in Figure 2.8) which have been attributed to the reduction of $UO_{2.33}$ to UO_{2+x} and $UO_3.2H_2O$ to UO_{2+x} respectively (Section 2.4.3).

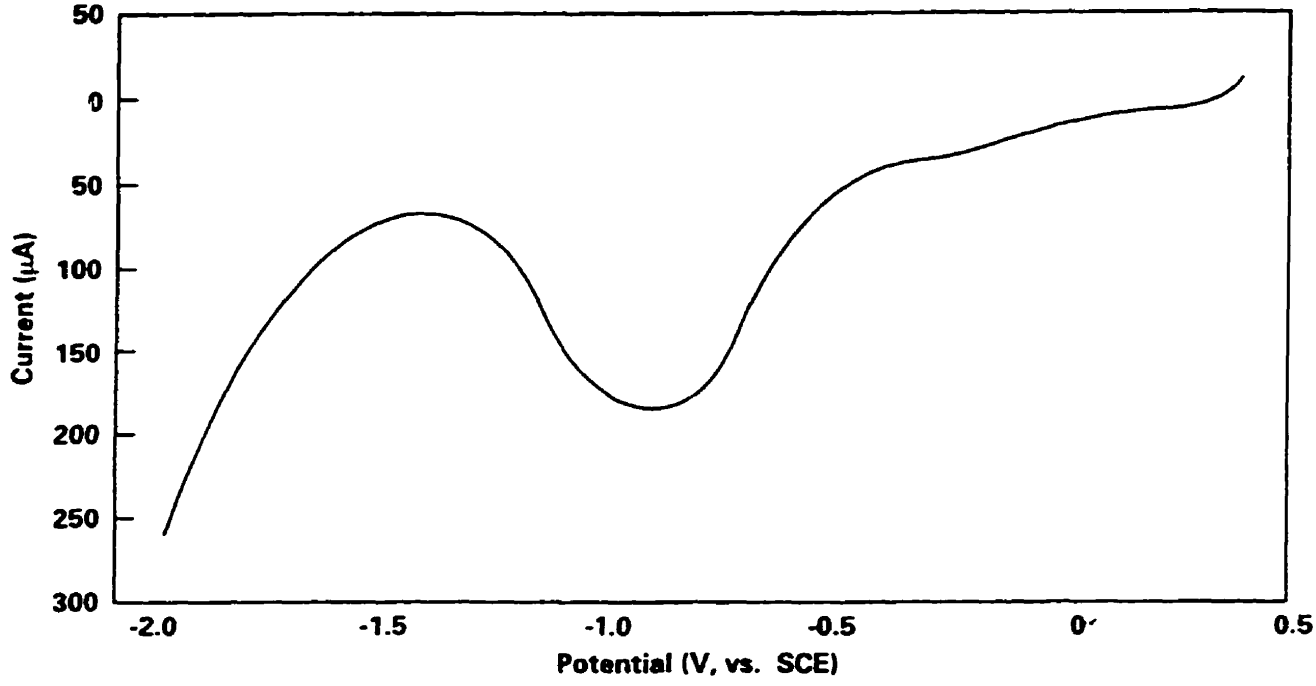

FIGURE 6.11: CSV recorded after anodic oxidation at 0.1 V for 18.5 hours in $NaClO_4$.

After anodic oxidation at a potential of 0.1 V for 20 hours in NaCl, the measured U^{VI}:U^{IV} ratio (4.156) (Table 6.1) is similar to that obtained in $NaClO_4$ (3.073). indicating that the surface layer in the NaCl solution also consists

primarily of U^{VI}, i.e. $UO_3.2H_2O$. The current -time plot recorded for anodic oxidation at 0.1 V in NaCl is similar in form, but approximately a factor of 2 higher than in $NaClO_4$. It is possible that this accounts for the larger U(VI):U(IV) ratio obtained after oxidation in NaCl. Whether this is due to the presence of a thicker film of $UO_3.2H_2O$ cannot be confirmed on the basis of the available information.

After anodic oxidation at a potential of 0.1 V for 20 hours in SCSSS, the U^{VI}:U^{IV} ratio is close to that expected for a layer of $UO_{2.33}$ (U^{VI}:U^{IV} = 0.5) [86]. This ratio would suggest that no $UO_3.2H_2O$ film is present to block the dissolution. However, the anodic oxidation current - time plot (Figure 6.1) is much lower than observed for $NaClO_4$ and NaCl, thus clearly indicating that the oxidation process is suppressed. The XPS spectrum also verifies that substantial amounts of calcium and silicon are present (Table 6.1). A possible explanation of these results is that the oxidation / dissolution / corrosion product film formation process is suppressed by the formation of a thin film of a U^{VI} phase which is highly insulating due to the incorporation of Ca and Si. This highly insulating film will prevent the electron transfer reactions required to sustain the electrochemical conversion process. The presence of such a thin insulating film would allow the escape of electrons from the substrate UO_2 leading to the distortion of the XPS results; i.e. the U^{VI}:U^{IV} ratio would be lower than expected for an insulating U^{VI} film due to the contribution to the spectrum of electrons from U^{IV} atoms in the underlying UO_2.

Evidence to support this was observed by Lahalle et al. [88]. They studied the surface composition of single crystals of UO_2 dissolving in groundwaters

containing calcium, magnesium and silicon. On the basis of XPS analyses, they concluded that dissolution was reduced by a factor of 10 to 100, compared to that occurring in deionized water, and attributed this to the formation of Mg/Si hydrous oxides which overlayed a layer of $UO_3.2H_2O$ on the surface.

A second piece of evidence was obtained by Tait et al. [89]. They observed a decrease in dissolution rate of UO_2 by a factor of 100 in a 0.02 $mol.L^{-1}$ HCO_3^- solution containing 0.1 to 50 $mg.L^{-1}$ SiO_4^{4-} and a decrease by a factor of 50 in a HCO_3^- solution containing 4 to 40 $mg.L^{-1}$ Ca^{2+}. Both ions were strongly adsorbed, or incorporated into a precipitated phase on the UO_2 surface since it required several weeks to restore the dissolution rate in a freshly prepared HCO_3^- solution.

For both $NaClO_4$ and NaCl oxidized at an anodic potential of 0.5 V for 1.5 hours, the U^{VI}:U^{IV} ratio is lower than at the anodic potential of 0.1 V (Table 6.1). The values obtained indicate that the surface consists primarily of $UO_{2.33}$ with a lesser amount of the U^{VI} phase (i.e. $UO_3.2H_2O$ in $NaClO_4$) [63]. This is consistent with a higher degree of UO_2^{2+} dissolving at higher potentials.

For SCSSS oxidized to an anodic potential of 0.5 V for 1.5 hours, the U^{VI}:U^{IV} ratio is greater than at 0.1 V, but is similar to the values obtained for $NaClO_4$ and NaCl at a potential of 0.5 V. This is supported by the similar current - time curves obtained for all three solutions (Figure 6.2). Furthermore, only minor amounts of silicon (Table 6.1) are incorporated into the surface compared to the behaviour at 0.1 V.

Consequently, at 0.5 V, the general uniform behaviour shows that solution

composition is not the most important factor dictating current-time behaviour. Also, the presence of silicon in SCSSS does not lead to the formation of insulating deposits, which block anodic dissolution.

7.0 SCANNING ELECTRON MICROSCOPY (SEM)

7.1 RESULTS

7.1.1 Logarithmic Current (I) - time (t) plots

Figure 7.1 shows the current-time plots for four solutions recorded over 3.5 hours of anodic oxidation at a potential of 0.425 V. The four solutions were $NaClO_4$, SCSSS, NaCl and SCSSS + HCO_3^-. The current recorded for oxidation in SCSSS was a factor of 3 lower than for NaCl, while the currents recorded for oxidation in SCSSS + HCO_3^- and $NaClO_4$ were a factor of 100 higher than in SCSSS. The currents in the last two solutions achieved steady state values in ~ 1 minute, whereas, for the first two solutions, steady state was approached, but not totally achieved after ~ 20 minutes.

Figure 7.2 shows the current-time transients recorded after anodic oxidation at a potential of 0.55 V for 90 minutes in $NaClO_4$, SCSSS and NaCl. All three solutions had similar plots that tended rapidly to steady-state.

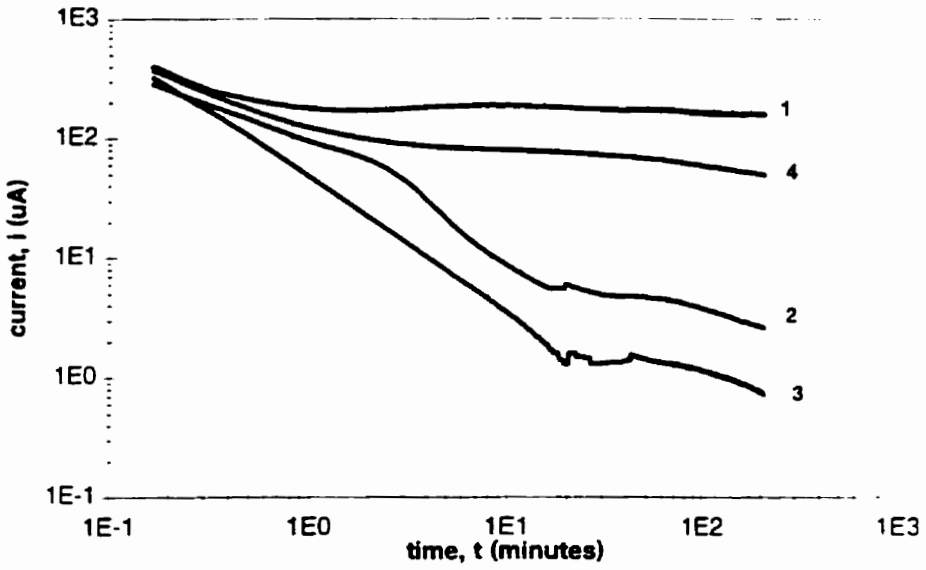

FIGURE 7.1: Plot of current as a function of time after anodic oxidation at 0.425 V for 3.5 hours in (1) $NaClO_4$ (2) NaCl (3) SCSSS and (4) SCSSS $+HCO_3^-$.

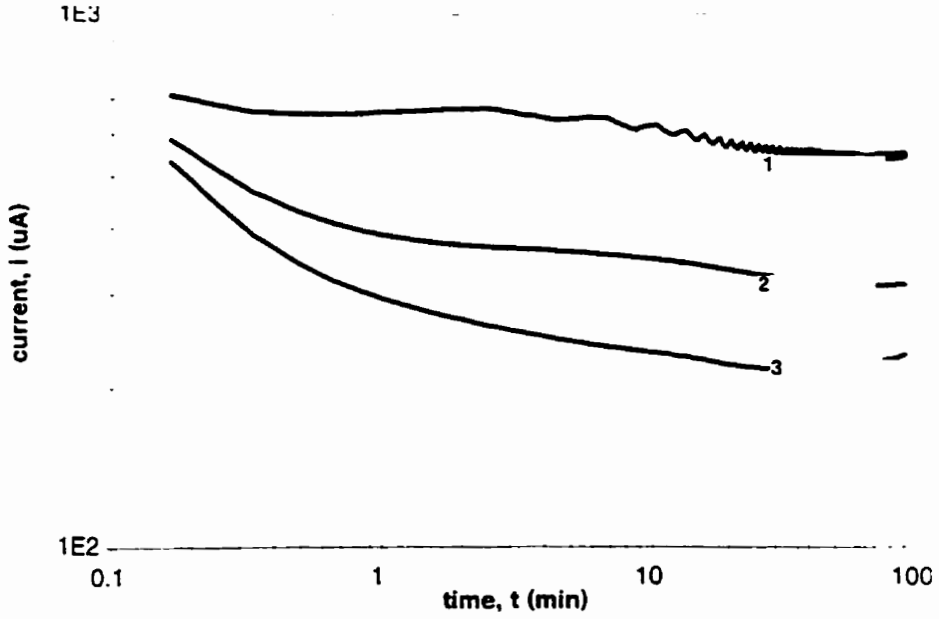

FIGURE 7.2: Plot of current as a function of time after anodic oxidation at 0.5 V for 1.5 hours in (1) $NaClO_4$ (2) NaCl and (3) SCSSS.

7.1.2 SEM Photomicrographs

SEM photomicrographs were taken after potentiostatic oxidation at 0.425 and 0.55 V to observe the extent and location of oxidation and how it relates to the current decay as a function of time. These photomicrographs were also compared to a freshly re-polished surface (Figure 7.3).

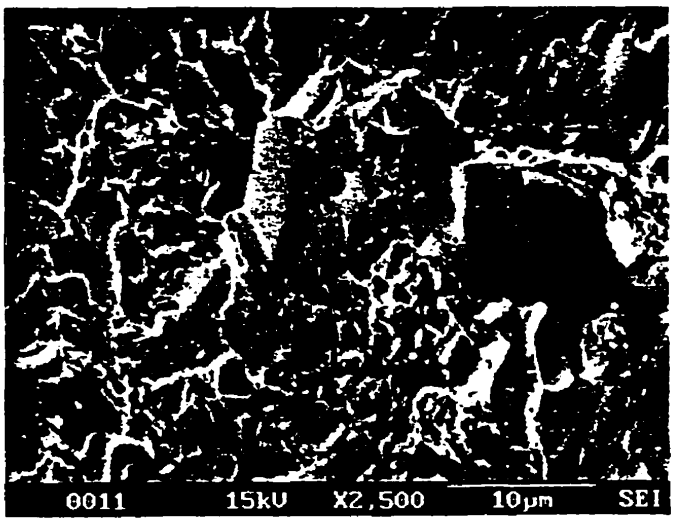

FIGURE 7.3: SEM photomicrograph at a magnification of 2500X on the ZR2 electrode after polishing to a 600 grit surface.

Figure 7.3 shows that the polishing process has smoothed many of the edges on the grain faces. Large amounts of polishing debris are present and are found mainly in the holes from which grains have fallen out. Also, the residual sintering porosity is evident as small holes and depressed areas on the crystal faces. These holes are probably predominantly at grain boundaries, even though it is not obvious from the photomicrograph.

Figures 7.4 to 7.7 show the SEM photomicrographs recorded on the ZR2 UO_2 electrode after anodic oxidation at 0.425 V for 3.5 hours in each of the four solutions.

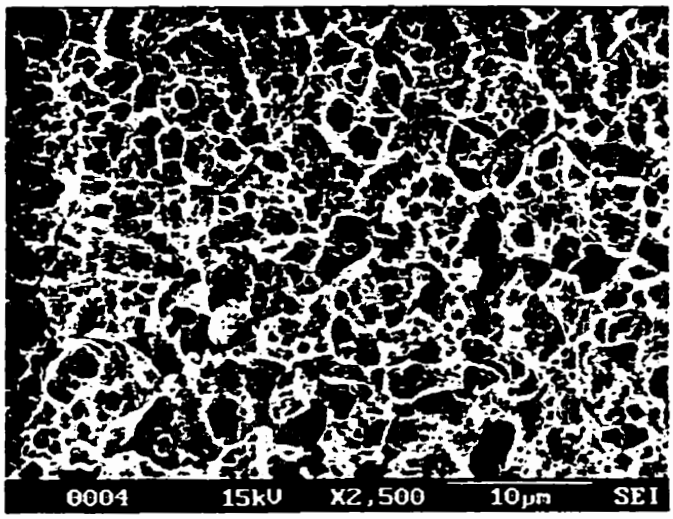

FIGURE 7.4: SEM photomicrograph at a magnification of 2500X on the ZR2 electrode after anodic oxidation at 0.425 V for 3.5 hours in $NaClO_4$.

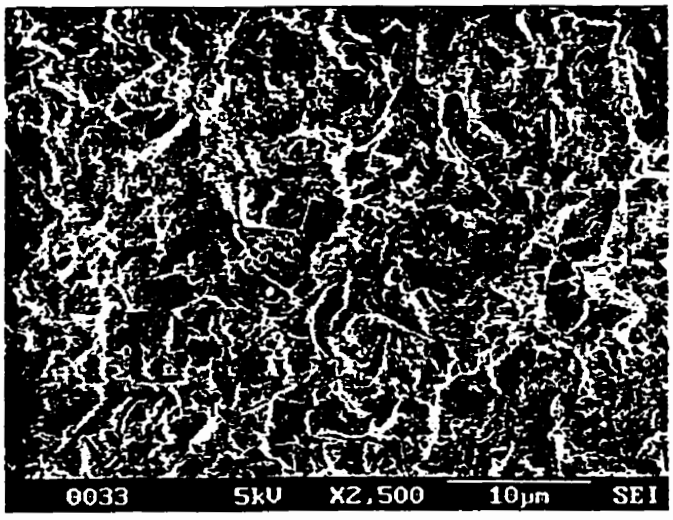

FIGURE 7.5: SEM photomicrograph at a magnification of 2500X on the ZR2 electrode after anodic oxidation at 0.425 V for 3.5 hours in SCSSS.

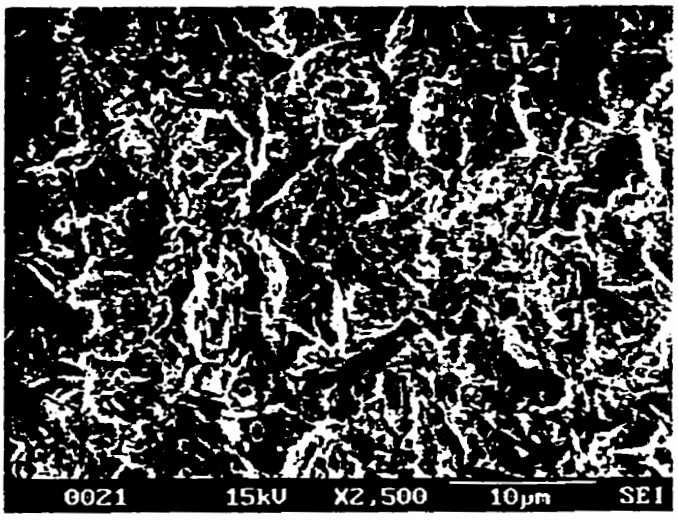

FIGURE 7.6: SEM photomicrograph at a magnification of 2500X on the ZR2 electrode after anodic oxidation at 0.425 V for 3.5 hours in NaCl.

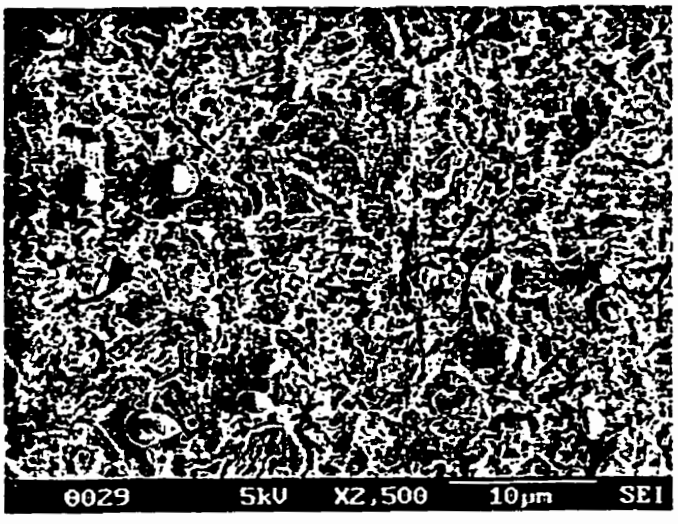

FIGURE 7.7: SEM photomicrograph at a magnification of 2500X on the ZR2 electrode after anodic oxidation at 0.425 V for 3.5 hours in SCSSS +HCO_3^-.

After treatment in the $NaClO_4$ solution, the SEM photomicrograph (Figure 7.4), compared to the re-polished surface (Figure 7.3), shows a uniformly etched surface free of polishing debris. There are many local pits, which suggest dissolution of local defects in the crystalline grains is occurring. There are some deep holes present; however they are not grain sized holes, and thus can not be attributed to grain loss. This suggests that if local dissolution starts to occur, deep penetrations are possible. From the above observations, there is no evidence for preferential grain boundary etching.

For anodic oxidation at 0.425 V in SCSSS (Figure 7.5), the photomicrograph shows no evidence for local etching of inter-grain defects. The grain edges, which are clearly visible on the re-polished electrode, are absent after treatment in SCSSS. The surface appears to be smoothed as if it had been electropolished. A comparison of the surface after treatment in $NaClO_4$ indicates that fewer large holes were present and the surface is not as cleanly etched.

After treatment in the NaCl solution (Figure 7.6), the surface has a similar matte finish as observed for SCSSS, but is not as even. This roughness suggests that oxidation of the surface is more aggressive compared to that for SCSSS. There are no large holes present and there is very minor evidence to suggest etching of the surface defects, as observed after treatment in the $NaClO_4$ solution.

In SCSSS + HCO_3^-, the SEM photomicrograph (Figure 7.7), shows some evidence that etched grains are still visible, while other areas have the matte finish of surfaces dissolved in SCSSS. The surface, when compared to that after

treatment in $NaClO_4$, has fewer and smaller local etched defects present, and fewer deeply pitted sites. However, there is a wider distribution of locally etched crevices. The spheres present on the surface contain Ca and U, which may possibly be attributed to the presence of a calcium uranate solid.

Figures 7.8 to 7.10 show the SEM photomicrographs of UO_2 surfaces after potentiostatic oxidation at 0.55 V for 90 minutes in $NaClO_4$, SCSSS and NaCl.

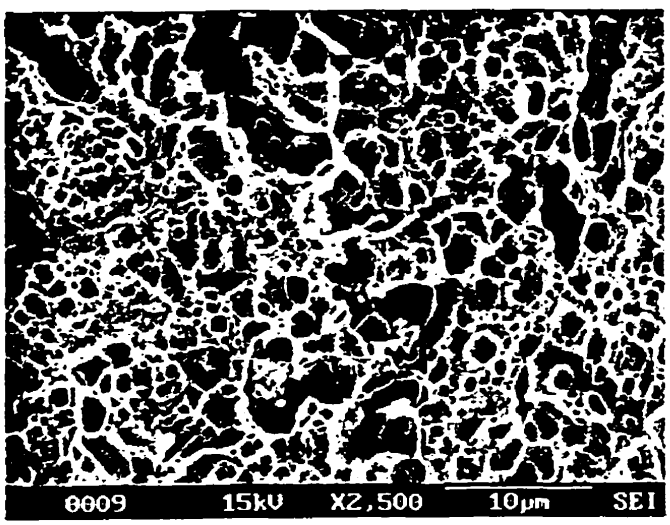

FIGURE 7.8: SEM photomicrograph at a magnification of 2500X on the ZR2 electrode after anodic oxidation at 0.55 V for 1.5 hours in $NaClO_4$.

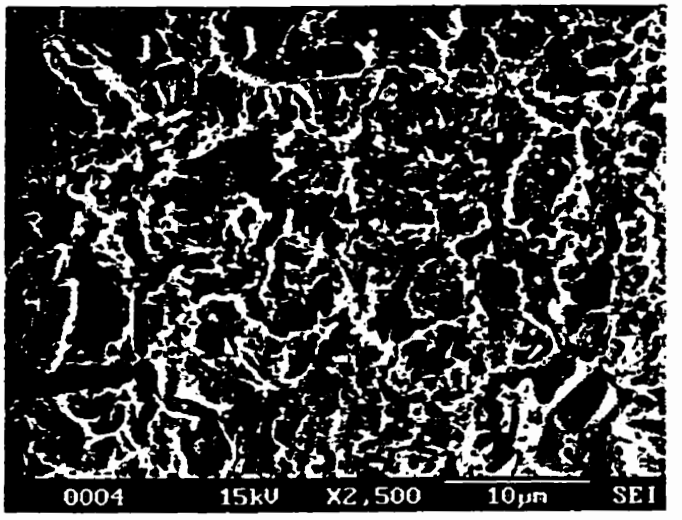

FIGURE 7.9: SEM photomicrograph at a magnification of 2500X on the ZR2 electrode after anodic oxidation at 0.55 V for 1.5 hours in SCSSS.

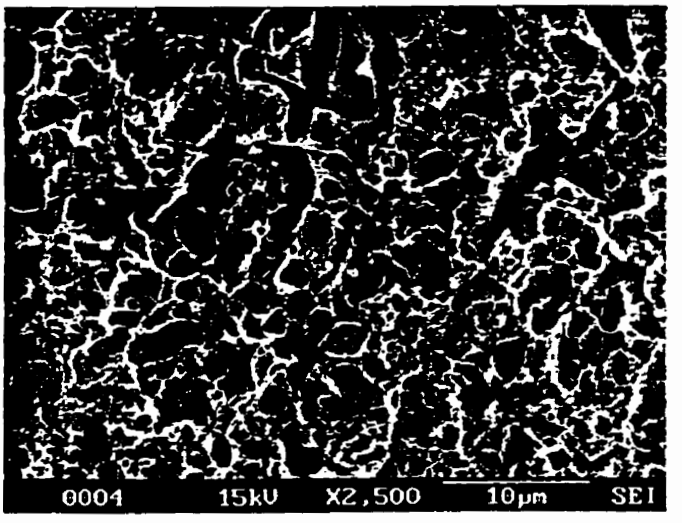

FIGURE 7.10: SEM photomicrograph at a magnification of 2500X on the ZR2 electrode after anodic oxidation at 0.55 V for 1.5 hours in NaCl.

The photomicrographs of the UO_2 surface are similar in all three solutions and show clean etching with pits scattered throughout. There is no evidence of preferential grain boundary etching.

7.2 DISCUSSION

As discussed in Section 2.4, the potential region in which dissolution as UO_2^{2+} is expected to dominate occurs at Ea > 0.35 V. This is the region where the UO_2 surface reaches steady-state dissolution conditions and the dissolution current follows a Tafel relationship. The uranyl ion production is rapid and dissolution is extensive leading to the development of local acidity according to reactions 2.5 and 2.6. The local acidity either prevents the precipitation of $UO_3.2H_2O$ (reaction 2. 4) or results in chemical dissolution of oxidized phases (reaction 2.7).

This effect is clearly shown in the current - time transient in the $NaClO_4$ solution after anodic oxidation at a potential of 0.425 V (Figure 7.1). The current is high and achieves a steady state indicating that a surface deposit ($UO_3.2H_2O$) is not present to block dissolution. The photomicrograph (Figure 7.4) clearly indicates that even though the defective grains are cleanly etched, the grain boundaries are not preferentially attacked. All of this evidence indicates that dissolution sites are widely distributed across the surface. Also, the presence of deep penetrations at a few sites can be taken as evidence of the aggressiveness of local chemistry (reactions 2.5 and 2.6) when dissolution is extensive.

In SCSSS, the etching of surface structural features is not observed

(Figure 7.5). Instead the visual evidence suggests that the surface features have been polished rather than etched as in $NaClO_4$. Also, the corresponding current (Figure 7.1) is much lower than in $NaClO_4$. Together, these observations indicate the presence of a surface deposit which blocks dissolution, thus avoiding the local etching and pitting. This would suggest that local acidity by reactions 2.5 and 2.6 does not occur, and therefore, would support the formation of a U^{VI} phase which blocks dissolution. However, the current does eventually tend to a steady-state value, although at a much lower value than for $NaClO_4$. This indicates that some dissolution is occurring, but in a different manner to that for $NaClO_4$. This evidence, along with the apparent polishing, could be attributed to a transport controlled dissolution through a surface deposit.

The current - time transient recorded over 3.5 hours (Figure 7.1) after treatment in NaCl shows that the current decays in the same manner as that for $NaClO_4$, except that it is a factor of 100 lower. This implies that the UO_2 surface is not dissolving as quickly as in $NaClO_4$. Therefore, precipitation by reaction 2.4 ($UO_3.2H_2O$ in $NaClO_4$) is more dominant than the dissolution of the uranyl ion by reactions 2.5 and 2.6. Evidence to support this is observed in the photomicrograph (Figure 7.6) in which there are no large holes, as in $NaClO_4$ indicating that local acidity has not yet developed. The U^{VI} phase formed is less protective than after treatment in SCSSS since the current is higher in NaCl. This is observed in the SEM photomicrograph (Figure 7.6) in which the matte finish on the surface is not as even as in SCSSS, suggesting a more aggressive attack. All of this evidence indicates that general supersaturation is occurring,

not local supersaturation at sites such as grain boundaries.

The presence of bicarbonate is known to accelerate the dissolution of UO_2 by stabilizing the uranyl ion by complexation with the bicarbonate anion (Section 2.4.6.2). Therefore, it is not surprising that after treatment in SCSSS + HCO_3^-, the current-time transient (Figure 7.1) achieves a steady state much more rapidly and at a higher current than in SCSSS. The higher current is evidence that the dissolution blocking process found in SCSSS is no longer evident, i.e., dissolution is occurring and local acidity is developing. However, the photomicrograph (Figure 7.7) indicates that the surface is partially blocked since the etching is less severe when compared to that for $NaClO_4$ (Figure 7.4). Also, the matte finish observed after anodic oxidation in SCSSS (Figure 7.5) is still visible in certain areas after anodic oxidation in SCSSS + HCO_3^-. Consequently, the SEM photomicrographs suggest that SCSSS has an effect on how bicarbonate behaves.

At high potentials (Ea = 0.55 V), the behaviour after treatment in $NaClO_4$, SCSSS and NaCl is the same since the current - time transients and SEM photomicrographs are similar. The high currents in the log i-t plots (Figure 7.2) achieve a steady-state rapidly indicating that dissolution is fast and extensive (reactions 2.5 and 2.6). The SEM photomicrographs (Figures 7.8 to 7.10) offers clear evidence that this acidity occurs locally as observed by the formation of pits. Furthermore, the SEM proves that this process does not occur preferentially at grain boundaries as previously thought.

8.0 ANODIC OXIDATION UNDER CONTROLLED POTENTIAL CONDITIONS

8.1 RESULTS

8.1.1 Logarithmic Current (i) - Time (t) Plots

Figures 8.1 to 8.4 show the logarithmic current (i) - time (t) plots recorded for four solutions over 90 minutes at potentials in the range from +0.1 to +0.55 V. The four solutions were $NaClO_4$, NaCl, SCSSS and SCSSS + $NaHCO_3$. The trend in all four solutions is that, at low potentials, the current decays as a function of time, while at high potentials the current reaches a steady state. The transition between non-steady state and steady state occurs at $E \geq 0.425$ V for $NaClO_4$, and NaCl, $E \geq 0.50$ V for SCSSS and $E \geq 0.35$ V for SCSSS + $NaHCO_3$.

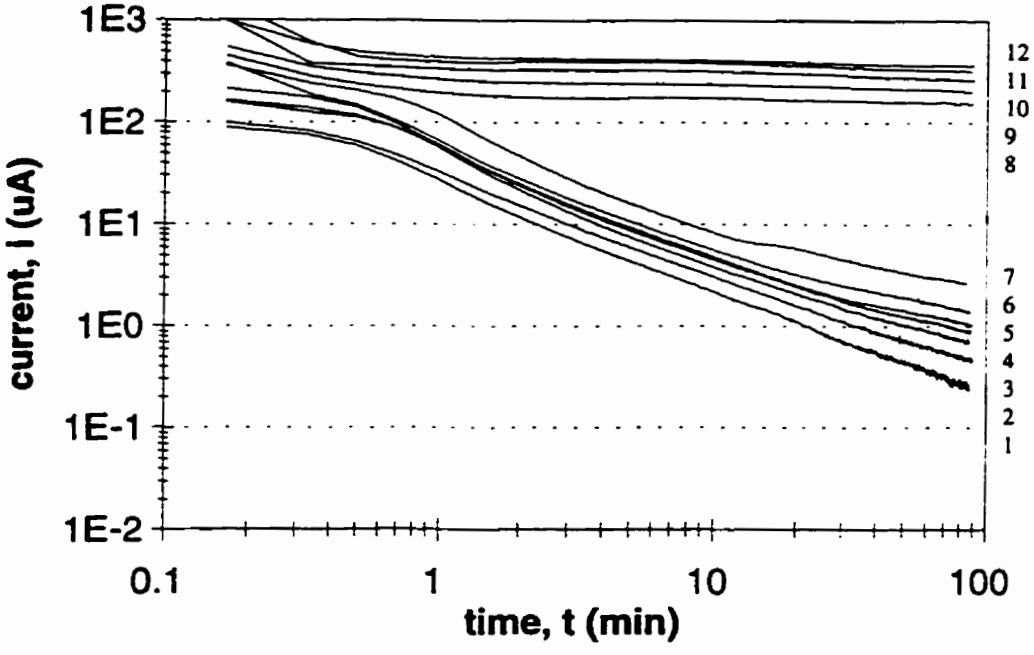

FIGURE 8.1: Plot of current as a function of time after anodic oxidation at (1) 0.1 V (2) 0.2 V (3) 0.3 V (4) 0.35 V (5) 0.375 V (6) 0.4 V (7) 0.425 V (8) 0.45 V (9) 0.475 V (10) 0.5 V (11) 0.525 V and (12) 0.55 V in $NaClO_4$.

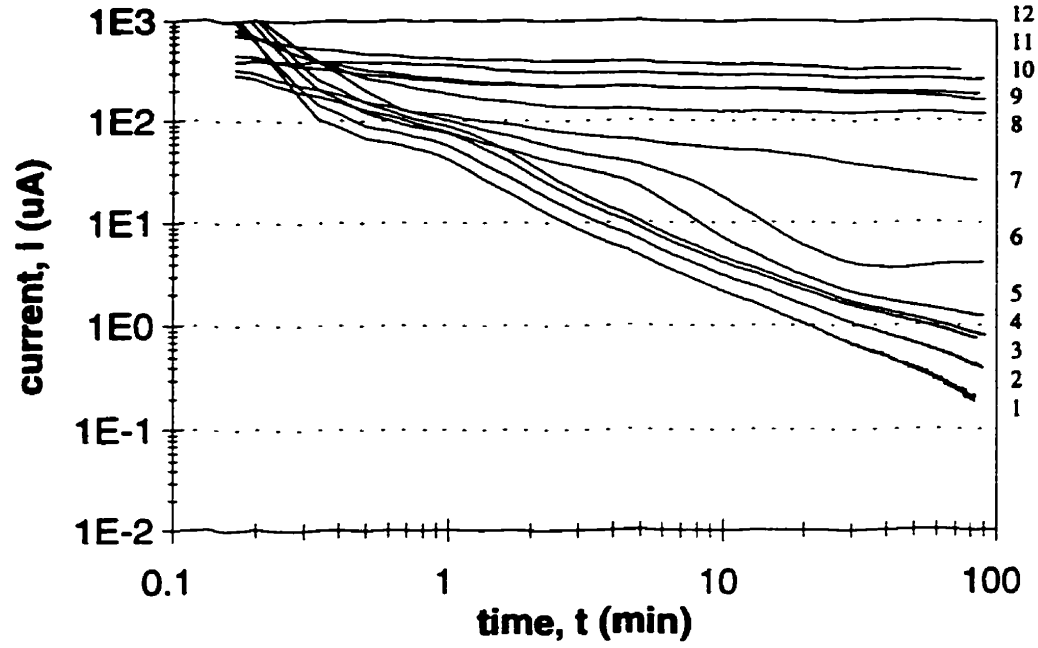

FIGURE 8..2: Plot of current as a function of time after anodic oxidation at (1) 0.1 V (2) 0.2 V (3) 0.3 V (4) 0.35 V (5) 0.375 V (6) 0.4 V (7) 0.425 V (8) 0.45 V (9) 0.475 V (10) 0.5 V (11) 0.525 V and (12) 0.55 V in NaCl.

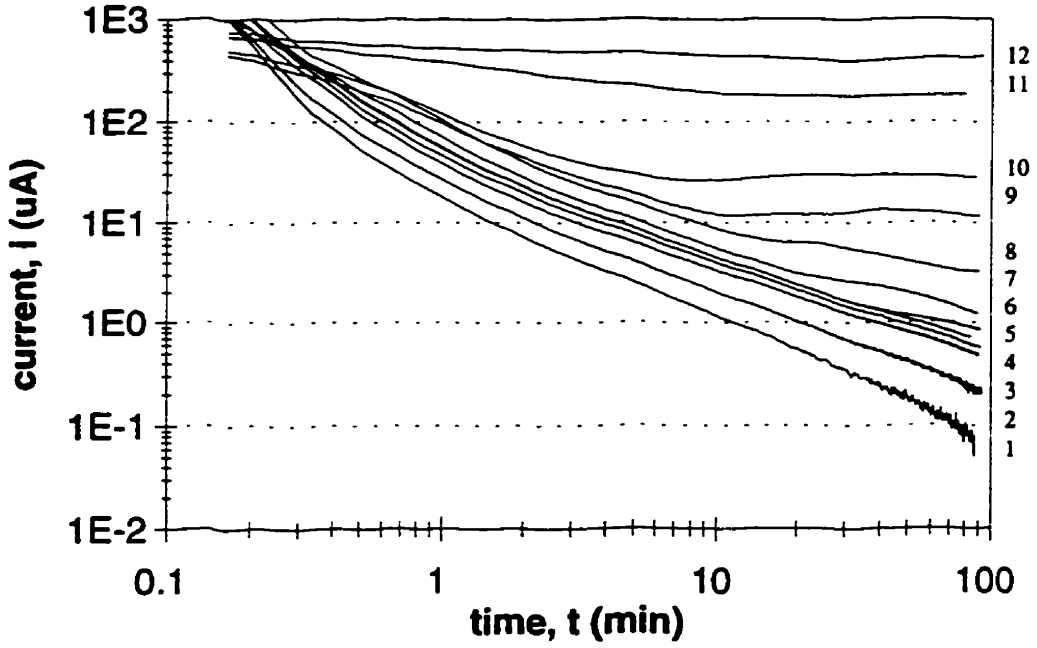

FIGURE 8.3: Plot of current as a function of time after anodic oxidation at (1) 0.1 V (2) 0.2 V (3) 0.3 V (4) 0.35 V (5) 0.375 V (6) 0.4 V (7) 0.425 V (8) 0.45 V (9) 0.475 V (10) 0.5 V (11) 0.525 V and (12) 0.55 V in SCSSS.

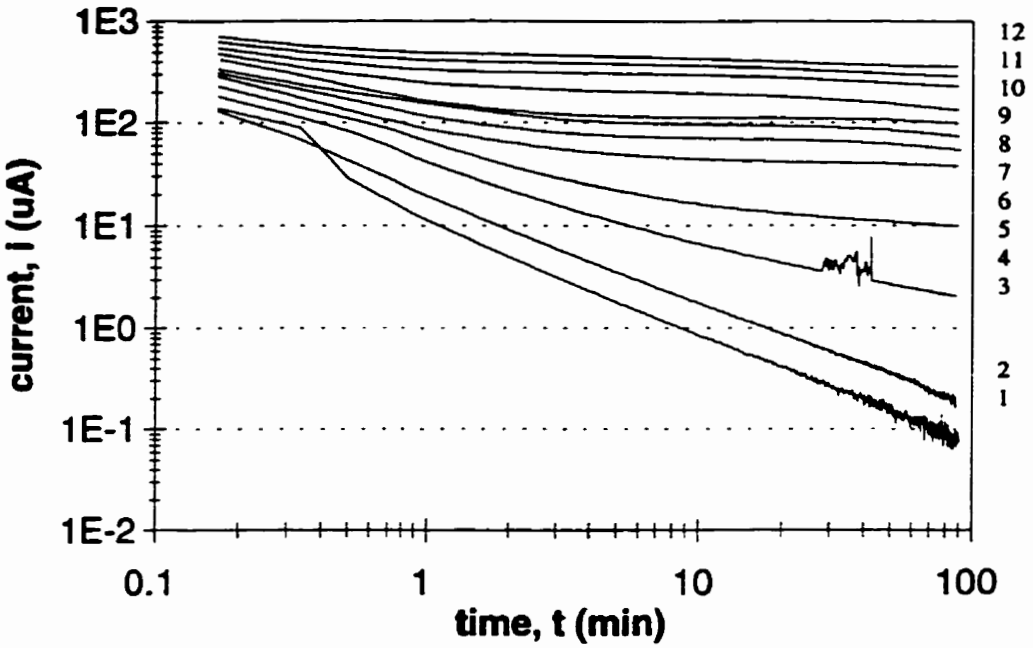

FIGURE 8.4: Plot of current as a function of time after anodic oxidation at (1) 0.1 V (2) 0.2 V (3) 0.3 V (4) 0.35 V (5) 0.375 V (6) 0.4 V (7) 0.425 V (8) 0.45 V (9) 0.475 V (10) 0.5 V (11) 0.525 V and (12) 0.55 V in SCSSS + HCO_3^-.

Comparisons of the logarithmic i-t plots are given in Figures 8.5, 8.6, and 8.7 at three potentials, which reflect the three areas where different behaviours are observed:

1) 0.1 V, the current decays as a function of time (i.e. non-steady state exists);
2) 0.425 V is a potential in the transition zone between the non-steady state and steady state regions;
3) 0.55 V is the highest anodic potential examined when a steady state is always achieved.

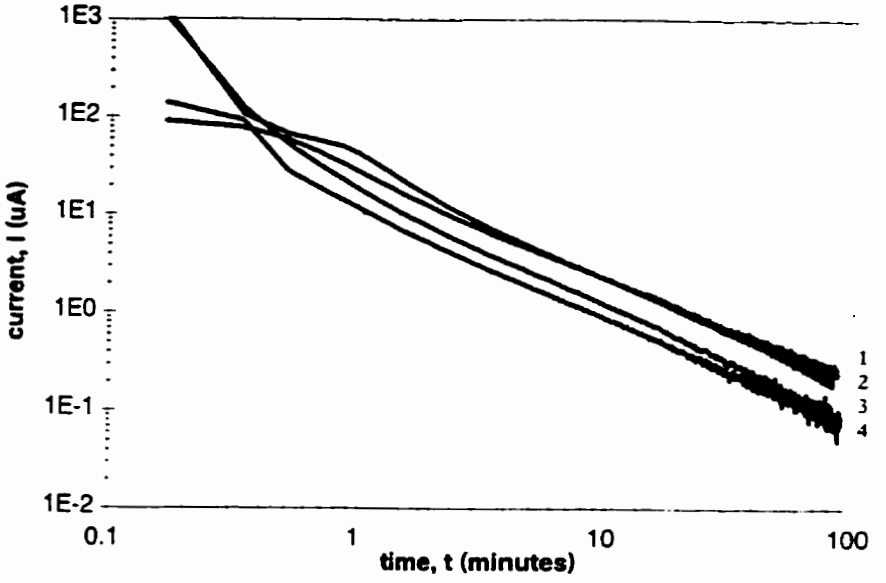

FIGURE 8.5: Plot of current as a function of time after anodic oxidation at 0.1 V in (1) $NaClO_4$ (2) NaCl (3) SCSSS and (4) SCSSS + HCO_3^-.

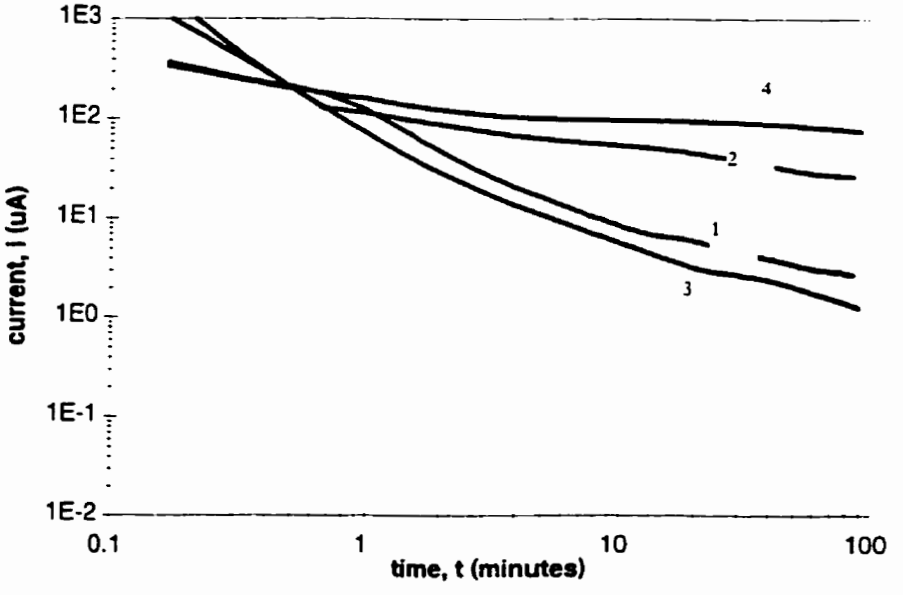

FIGURE 8.6: Plot of current as a function of time after anodic oxidation at 0.425 V in (1) $NaClO_4$ (2) NaCl (3) SCSSS and (4) SCSSS + HCO_3^-.

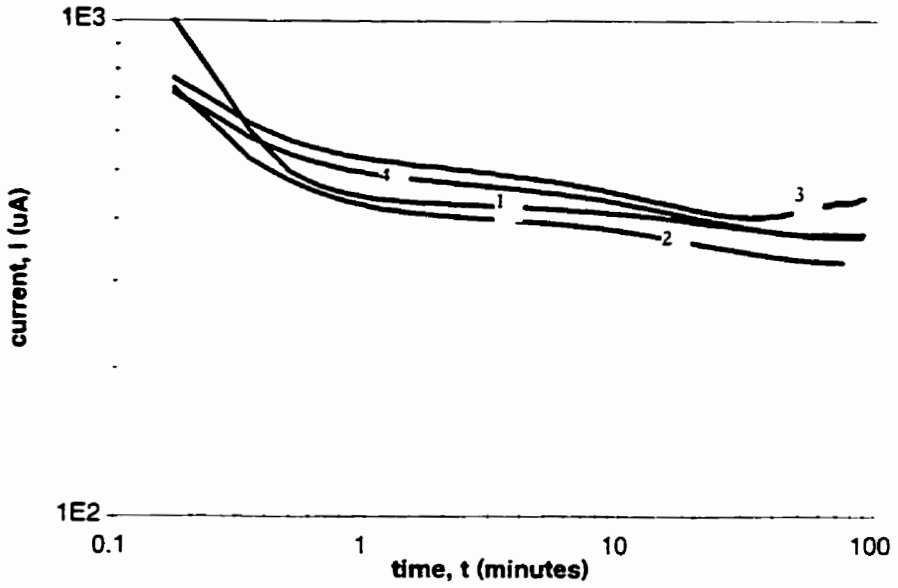

FIGURE 8.7: Plot of current as a function of time after anodic oxidation at 0.55 V in (1) $NaClO_4$ (2) NaCl (3) SCSSS and (4) SCSSS + HCO_3^-.

Except for the first 20 seconds or so, the log i - log t plots at 0.1 V (Figure 8.5) in $NaClO_4$ and NaCl are effectively identical, as are those recorded in SCSSS and SCSSS + $NaHCO_3$. However, the latter are slightly lower than the former. The log i-t plots at 0.55 V (Figure 8.7) are also the same within a factor of ~3. However, the currents measured at 0.425 V (Figure 8.6) show significant differences between the four solutions. The current recorded in the SCSSS solution is slightly lower than for $NaClO_4$,, while that recorded in NaCl is a factor of 10 higher, and in SCSSS + $NaHCO_3$ a factor of 100 higher (Figure 8.6).

8.1.2 Cathodic Stripping Voltammograms

Figures 8.8 to 8.11 show the CSV's for the four solutions recorded after measurement of the log i-t curves at 0.1, 0.425 and 0.55 V.

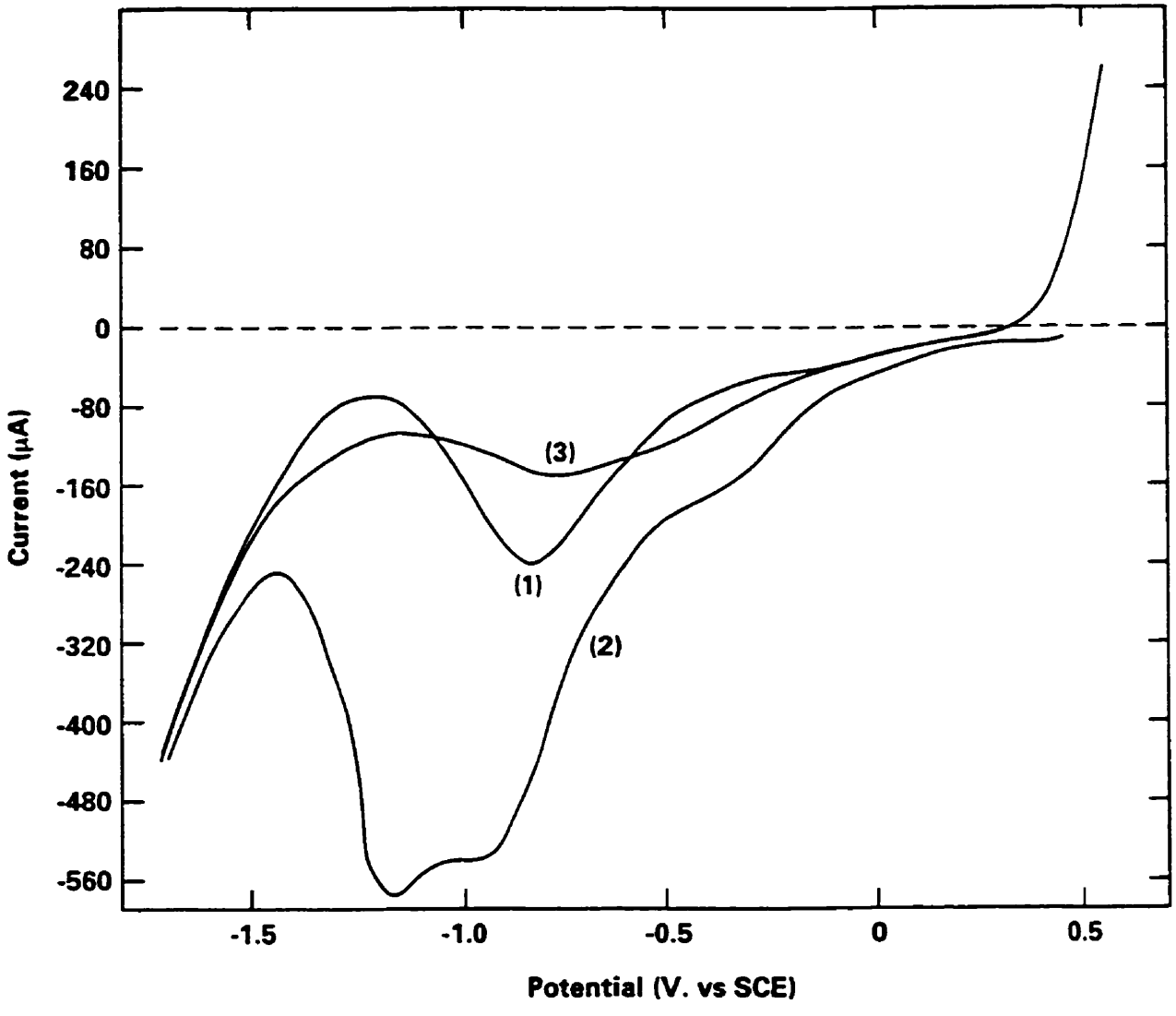

FIGURE 8.8: CSV's recorded after anodic oxidation for 90 minutes at (1) 0.1 V (2) 0.425 V and (3) 0.55 V in $NaClO_4$.

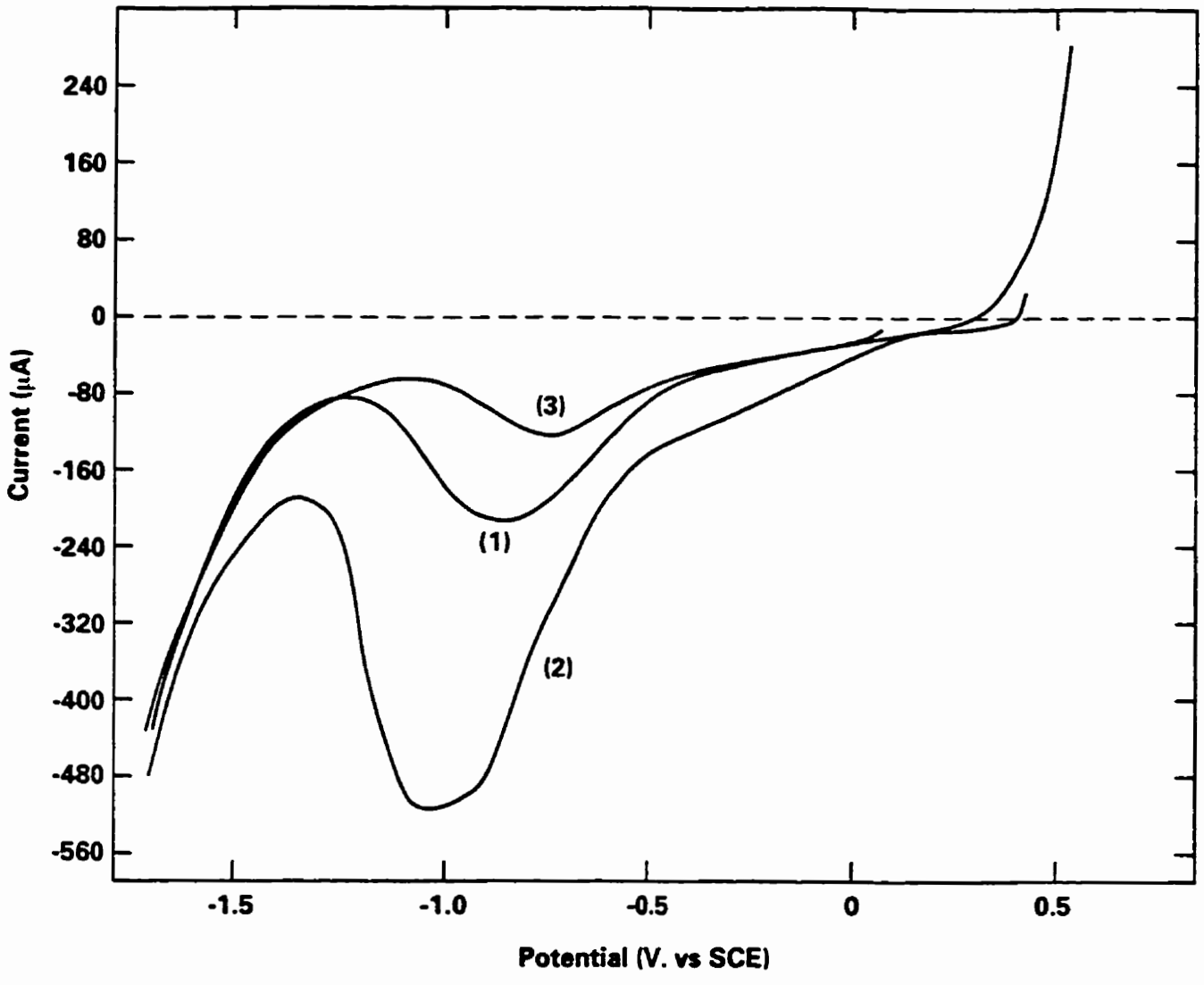

FIGURE 8.9: CSV's recorded after anodic oxidation for 90 minutes at (1) 0.1 V (2) 0.425 V and (3) 0.55 V in NaCl.

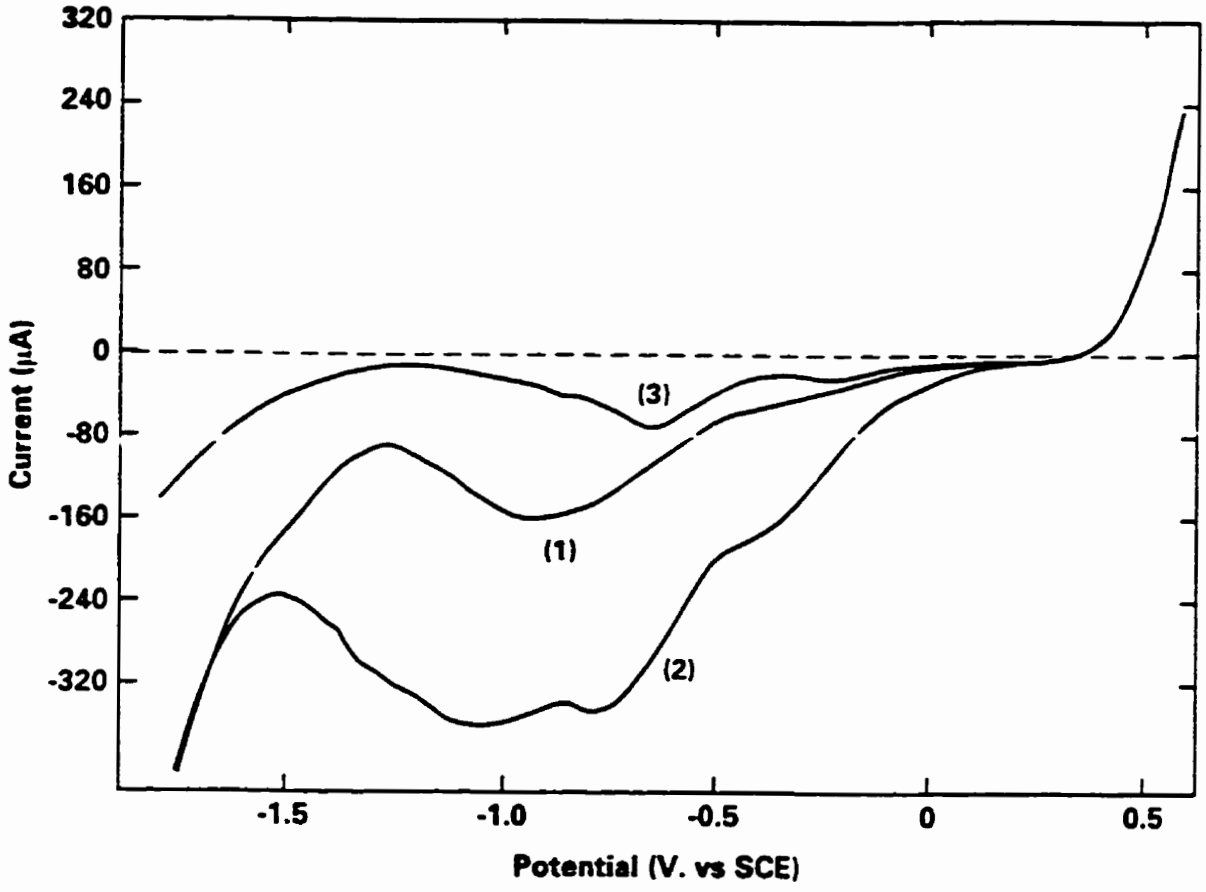

FIGURE 8.10: CSV's recorded after anodic oxidation for 90 minutes at (1) 0.1 V (2) 0.425 V and (3) 0.55 V in SCSSS.

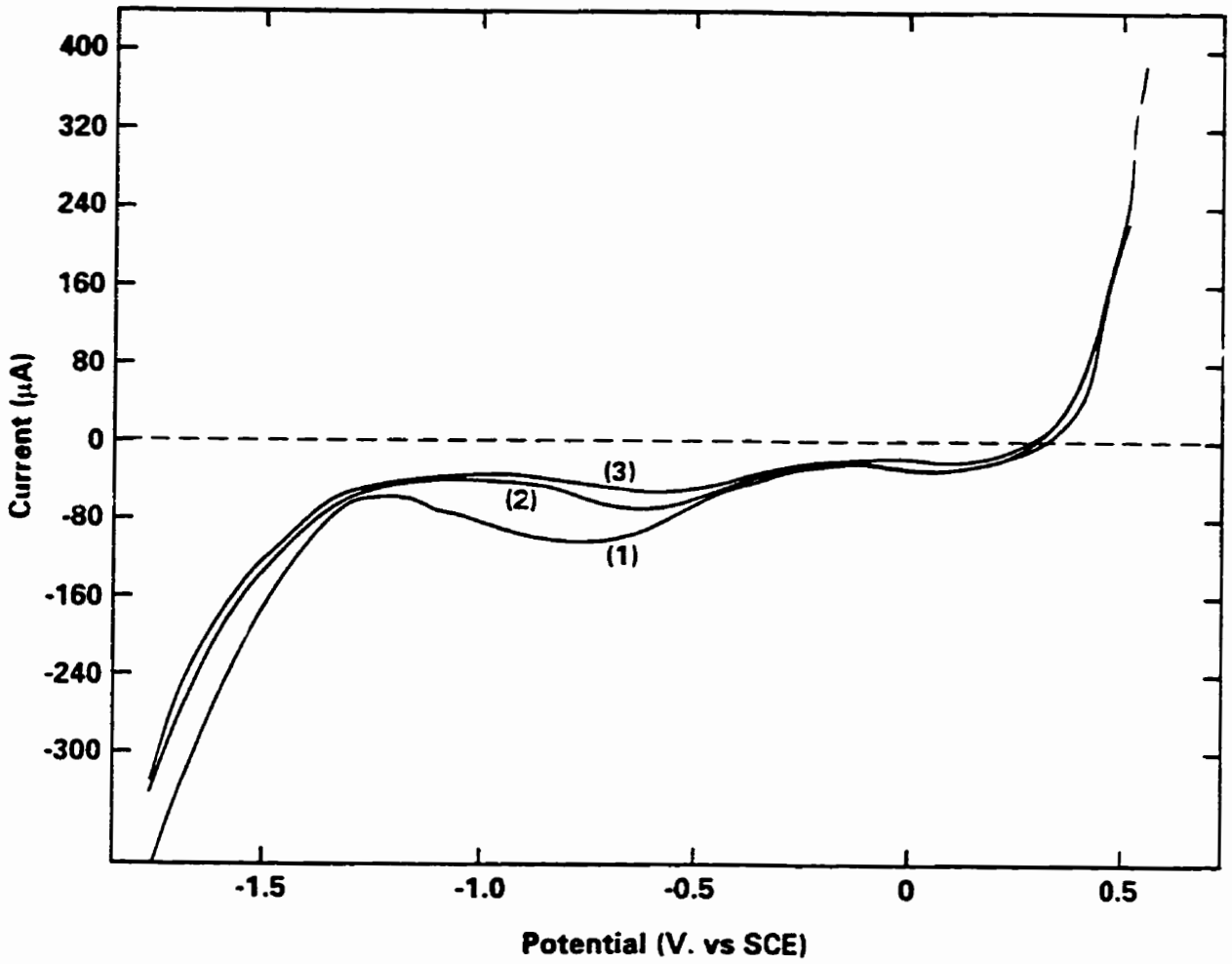

FIGURE 8.11: CSV's recorded after anodic oxidation for 90 minutes at (1) 0.1 V (2) 0.425 V and (3) 0.55 V in SCSSS + HCO_3^-.

Figures 8.12 to 8.14 show the overlay of the CSV's for each solution at the three potentials.

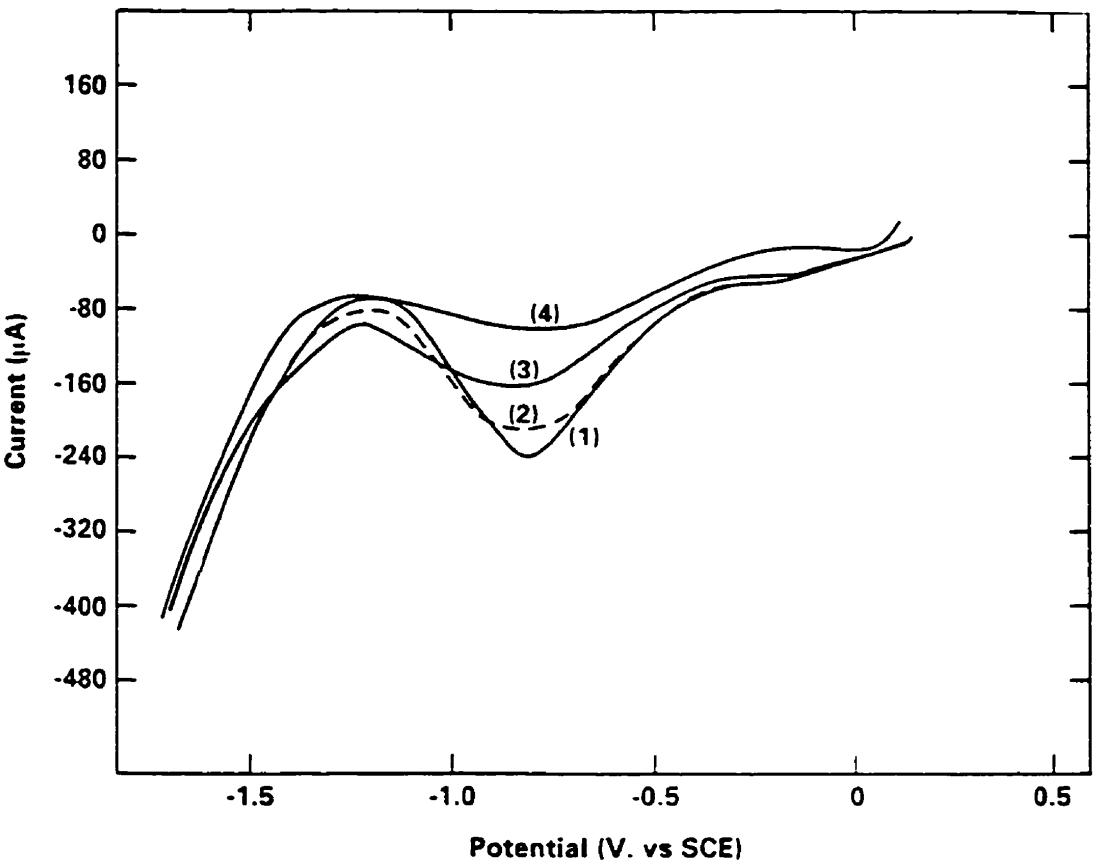

FIGURE 8.12: CSV's recorded after anodic oxidation at 0.1 V in (1) $NaClO_4$ (2) NaCl (3) SCSSS and (4) SCSSS + HCO_3^-.

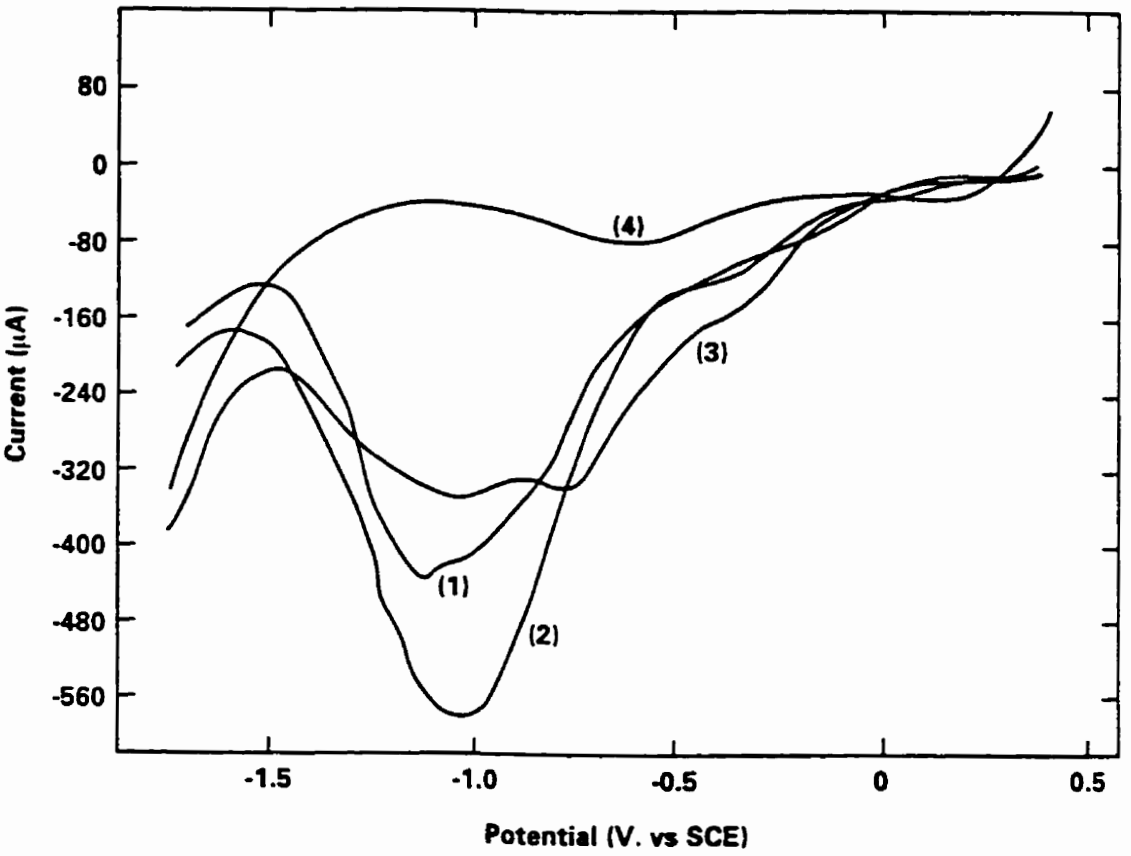

FIGURE 8.13: CSV's recorded after anodic oxidation at 0.425 V in (1) $NaClO_4$ (2) NaCl (3) SCSSS and (4) SCSSS + HCO_3^-.

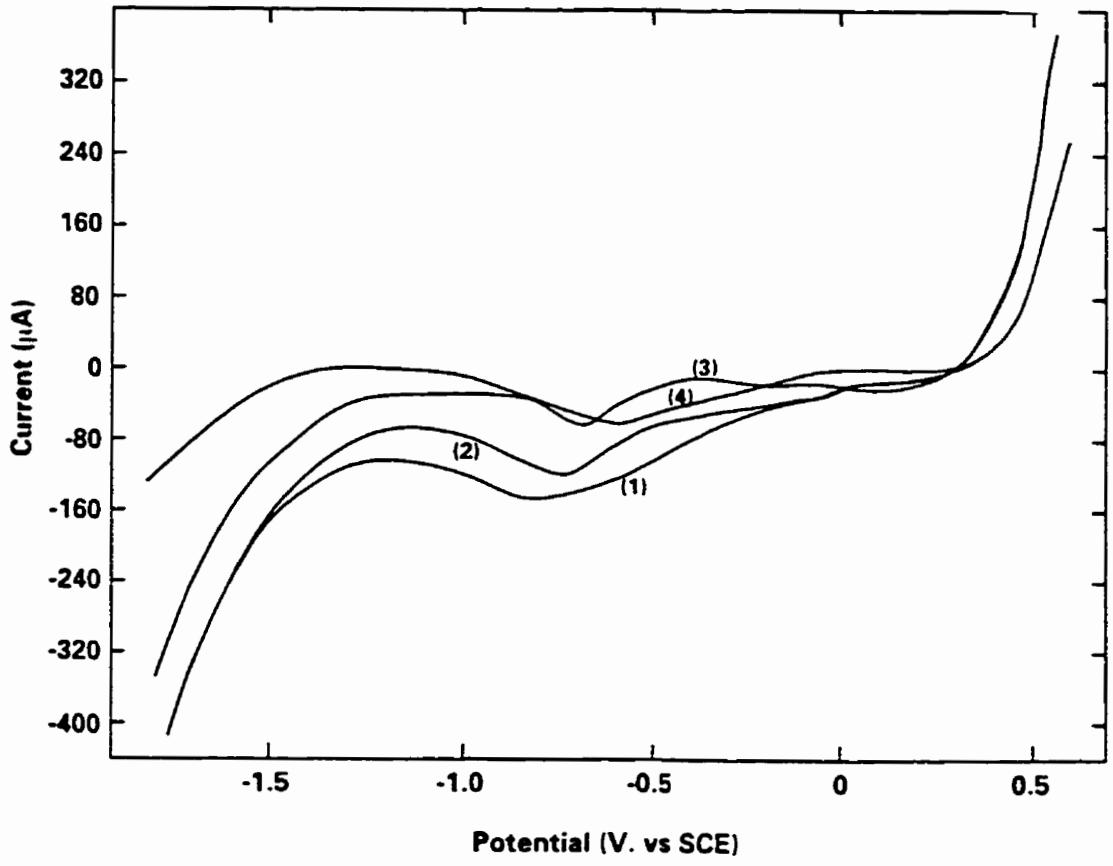

FIGURE 8.14: CSV's recorded after anodic oxidation at 0.55 V in (1) $NaClO_4$ (2) NaCl (3) SCSSS and (4) SCSSS + HCO_3^-.

Two reduction peaks, more obvious in SCSSS than in $NaClO_4$ and NaCl, are observed, along with a shoulder on the leading edge of the reduction peaks. The first reduction peak (at ~-0.7 V) and the second (at ~-0.9 V) were designated

peaks V and VI in Section 2.4.3. The shoulder on the leading edge of peak V at ~-0.2 V (Figure 8.8) is surprising, but has been seen before [63]. Within the compass of our present explanations this peak would be attributed to a layer of U^{VI} (generally thought to be $(UO_2^{2+}{}_{(ads)})$, i.e. Peak IV in Section 2.4.3).

For $NaClO_4$, the reduction at peak V is present for all anodic potentials applied. This peak increases in size with increasing potential until E > 0.425 V. The reduction at peak VI becomes distinct at E ~0.35 V and increases in size with increasing potential until E > 0.425 V. For E > 0.425 V peak VI is no longer present and peak V is much smaller.

For SCSSS (Figure 8.10), reduction at peaks V and VI are broader than in $NaClO_4$. The reduction peak V is present in the CSV's after anodic oxidation at all potentials. Peak V increases in size with increasing potential until E > 0.525 V. The reduction peak VI is noticeable at 0.1 V and increases in size with increasing potential until E > 0.525 V. At E = 0.55 V peak VI is no longer noticeable, while peak V is smaller and similar in size to that observed at 0.525 V in $NaClO_4$ (Figure 8.14).

For NaCl, after anodic oxidation at 0.1 V, the CSV yields a reduction peak almost identical in size and position to that observed in $NaClO_4$ (Figure 8.12). This is consistent with the observation that the log i - log t plots (Figure 8.5) are effectively identical. At 0.55 V, (Figure 8.14), the CSV's for NaCl and $NaClO_4$ are again similar, although the shoulder on the negative side of reduction peak V is slightly larger in $NaClO_4$ than in NaCl. This is also consistent with the log i - log t plots in Figure 8.7, which are very similar. At 0.425 V, (Figure 8.13), the CSV's

are distinctively different, Peak VI is apparently not present in NaCl. This suggests that only $UO_{2.33}$, not $UO_3.2H_2O$, is present after anodic oxidation in NaCl. The log i - log t plots are also different at this anodic potential in which the current recorded in NaCl is a factor of 10 higher than that for $NaClO_4$ (Figure 8.6).

For SCSSS + HCO_3^- (Figure 8.11), anodically oxidized at 0.1 V, the reduction peak is larger and broader than at 0.425 V and 0.55 V, suggesting both reduction peaks V and VI, are present. This is consistent with the log i - log t behaviour which is very similar to that observed in the other solutions, Figure 8.5 (i.e. peak VI is present when log i - log t decays to a small value, but absent when high currents and steady state behaviour are observed). Also, at 0.1 V, (Figure 8.12), the combined reduction peak V and VI is similar to that observed for SCSSS, but smaller, consistent with the observation that the log i - log t behaviour in the two solutions is effectively identical. At 0.425 V, (Figure 8.13) the CSV in SCSSS + HCO_3^- yields much smaller reduction currents than observed in SCSSS, which is consistent with the much higher currents observed in the log i – log t plots at this potential (Figure 8.6). At 0.55 V, (Figure 8.14) the CSV is very similar to that recorded in SCSSS, consistent with the similar log i - log t plots recorded in both solutions (Figure 8.7).

8.1.3 Cathodic charge

Figure 8.15 shows the cathodic charges (Qc) recorded as a function of applied potential calculated from the CSV's in Figures 8.8 to 8.11 as described in

Section 3.4.5.

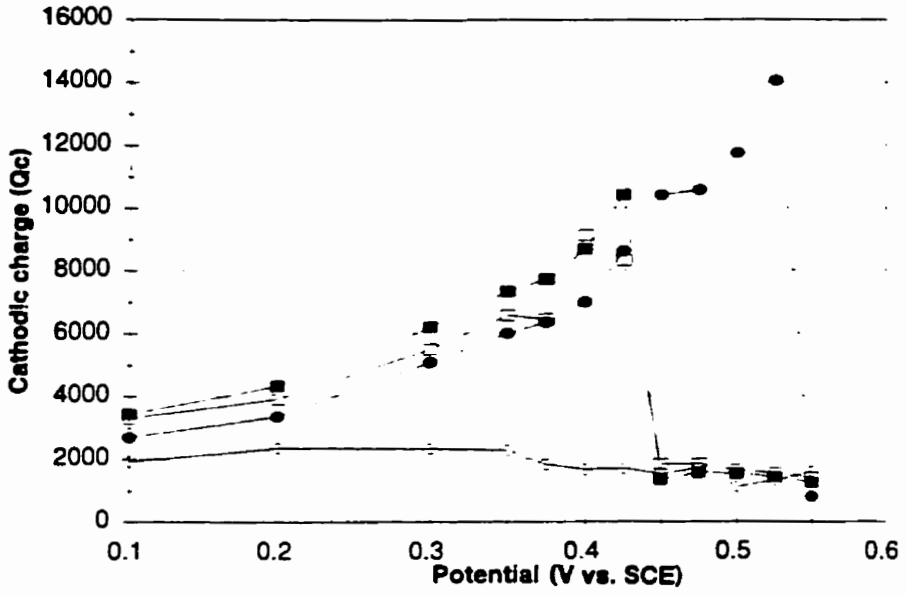

FIGURE 8.15: Plot of the cathodic charges (Qc) recorded as a function of applied potential from the CSV's in -■- $NaClO_4$ -⊟- NaCl -●- SCSSS and -⊖- SCSSS + HCO_3^-.

The Qc values are similar for $NaClO_4$, SCSSS and NaCl at potentials ≤ 0.45 V. At anodic potentials between 0.45 V and 0.525 V, the Qc value recorded in SCSSS is much greater than that recorded in $NaClO_4$ and NaCl, but becomes similar again at 0.55 V. The Qc values recorded in SCSSS + HCO_3^- are lower at anodic potentials ≤ 0.45 V, but are similar to the values recorded in $NaClO_4$ and NaCl at potentials ≥ 0.45 V (Figure 8.15).

8.1.4 Logarithmic Current - Potential Plots

The final values of the currents recorded over the whole potential range (0.1 to 0.55 V) are plotted logarithmically as a function of applied potential in Figure 8.16.

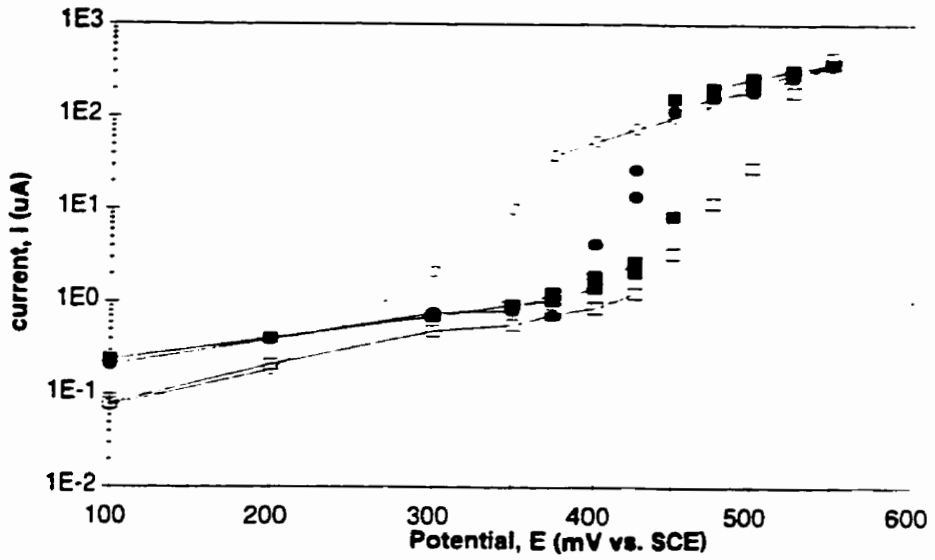

FIGURE 8.16: Plot of the steady state currents obtained after anodic oxidation for 90 minutes in ⊸ $NaClO_4$ ⊸ NaCl ⊸ SCSSS and ⊸ SCSSS + HCO_3^-.

The plot can be divided into two distinct regions. For $NaClO_4$ the first region is observed for $E \leq 0.425$ V and the second region for $E \geq 0.425$ V. For SCSSS the first region occurs for $E \leq 0.5$ V and the second region for $E \geq 0.5$ V. For NaCl the first region occurs for $E \leq 0.425$ V and the second region for $E \geq 0.425$ V. However, there is some scatter in the data in the potential range between 0.375 and 0.45 V in $NaClO_4$ and NaCl.

For SCSSS + HCO_3^-, three regions are observed. The first region occurs

at $E \leq 0.2$ V and the log i – log t plots show that film growth predominates in the same manner as in the absence of carbonate (i.e. in SCSSS alone) (Figure 8.5). The second region at $0.2 V < E < 0.35$ V is the region where steady state currents are eventually achieved and a Tafel region is obtained, whereas in the other solutions non-steady state suppression of the current is observed. The third region occurs at $E > 0.35$ V when a change in Tafel slope is observed from a value of ~60 mV^{-1} to ~105 mV^{-1}. In this region, all four solutions look the same, although SCSSS requires a higher potential to achieve this common state.

The largest difference in current, between the four solutions, occurs at 0.425 V. The current is a factor of 3 higher in $NaClO_4$ than in SCSSS and a factor of 10 higher in NaCl than in $NaClO_4$. For HCO_3^-, the current is a factor of 100 higher than in $NaClO_4$ (Figures 8.6 and 8.16)

8.1.5 Uranium Concentration

The uranium concentration was measured in $NaClO_4$ after a sequential series of oxidations for 90 minutes at four anodic potentials (0.45, 0.475, 0.5 and 0.525 V). The electrode was repolished in between each potential, but the solution was not changed. The uranium concentration was also measured after anodic oxidation for 90 minutes at a potential of 0.55 V in a fresh solution of $NaClO_4$. The U^{VI} concentration after the sequence from 0.425 to 0.525 V ($[U]_T$) was 11.9 $g.L^{-1}$ and after 0.55 V ($[U]_{550}$) was 7.5 $g.L^{-1}$.

8.2 DISCUSSION

Although there are many different forms of log i - log t plots possible, Figure 8.17 illustrates the most likely forms for UO_2 oxidation and dissolution. The figure shows the behaviour expected for a number of film formation / dissolution scenarios which could occur at a rotating disc electrode when the influence of solution transport processes is eliminated. While Figure 8.17 is illustrating film growth/dissolution by oxidation of a metal, the growth and dissolution of a higher oxide on UO_2 is expected to proceed by similar processes. Figure 8.17A illustrates film growth by the high field ion conduction process (HFIC). In the HFIC process, the U^{6+} ions are moving out to, and the O^{2-} ions are moving in from the electrode / solution interface. Providing no dissolution occurs, this process, HFIC, will result in a linear log i - log t plot in which the rate of film growth is inversely proportional to its thickness. Figure 8.17B illustrates the current - time behaviour anticipated for anodic dissolution proceeding at a steady state rate unimpeded by film growth. Figure 8.17C illustrates film growth by the HFIC process leading to the formation of an oxide with a finite dissolution rate (i.e. the combination of 8.17A and 8.17B). Figure 8.17D illustrates dissolution leading to local supersaturation with dissolved species and, hence, the precipitation and growth of an oxide/hydroxide film which eventually blocks dissolution.

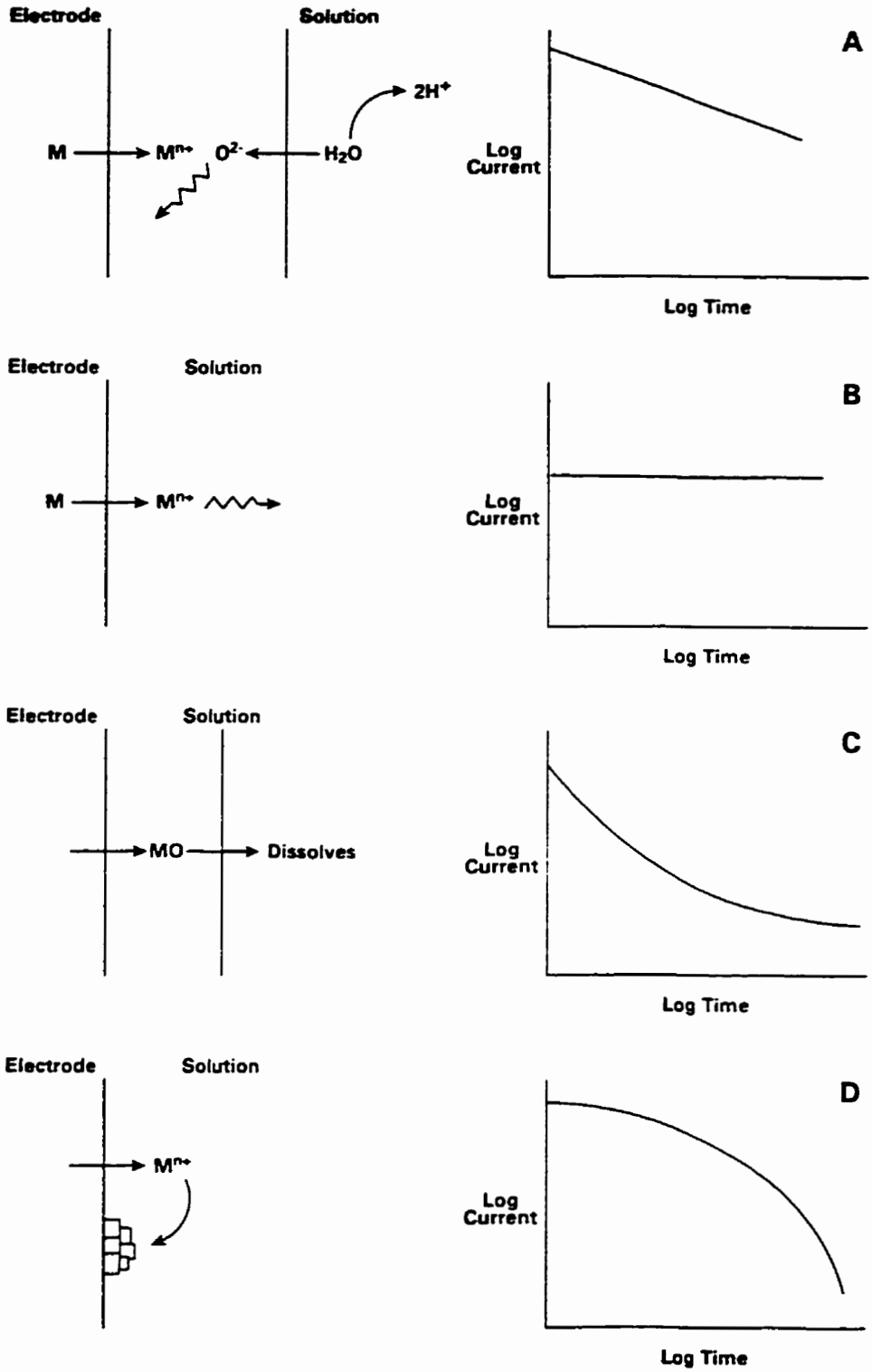

FIGURE 8.17: Schematic illustration of film growth / dissolution for anodic oxidation on a metal by (A) HFIC; (B) anodic dissolution proceeding at a steady state rate with no film growth; (C) HFIC followed by the dissolution of the oxide; (D) dissolution followed by the formation of an oxide.

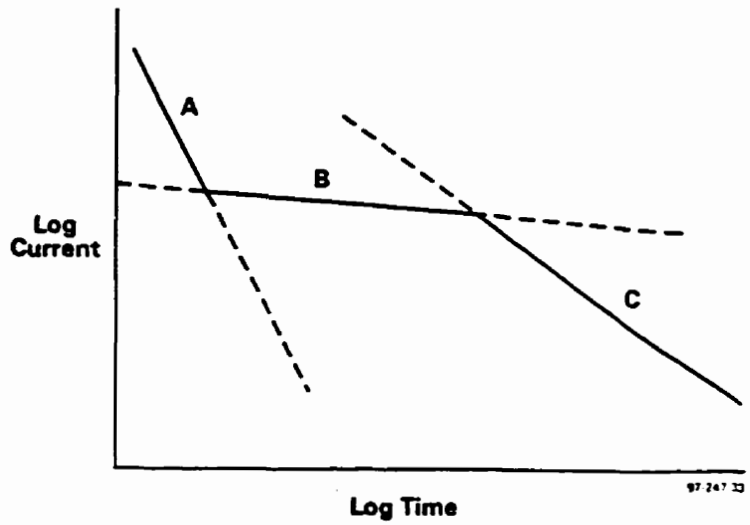

FIGURE 8.17E: Schematic illustration of HFIC leading to dissolution followed by precipitation of a film.

The form of the log i - log t expected via the combination of 8.17C and 8.17D is illustrated in Figure 8.17E; i.e. the growth of a film with a finite solubility (by HFIC), which subsequently dissolves at a rate sufficient to cause local supersaturation and, hence, the precipitation of a second film which eventually blocks dissolution.

All of the above films will be different in structure since their mechanisms of formation are distinctively different. A film grown by HFIC (Figure 8.17A) would be expected to retain the surface features of the original oxide since no major structural rearrangement has occurred. A film grown by deposition/precipitation (i.e. nucleation and growth from solution in Figure 8.17B) would be expected to have a different morphology to the substrate oxide, and could exhibit crystalline facets.

Films grown via these distinct ways (Figures 8.17C and 8.17D) would

differ in composition depending on the complexity of the film formation / dissolution / deposition process. For example, if a multiplicity of oxidation states (M^{n+}, $M^{(n+1)}$, etc.) exist for the metal cation, it is possible that the film grown by HFIC would comprise a lower oxidation state than the final deposited oxide. These differences generally lead to the observation of separate cathodic reduction peaks for multilayer films, as observed in this work.

A more detailed discussion of the film formation processes for UO_2 in $NaClO_4$, NaCl, SCSSS and SCSSS + HCO_3^- is given below.

$\underline{NaClO_4}$

The log i -log t plot (Figure 8.1) can be separated into two regions; the non-steady state region for $E \leq 0.425$ V and the steady state region for $E \geq 0.425$ V.

In the non-steady state region ($E \leq 0.425$ V) the current - time transients decay continuously with time and have the form expected for the behaviour illustrated in Figure 8.17D (i.e. dissolution followed by a deposition of a film which blocks dissolution). The Qc - E plot (Figure 8.15) increases linearly in the non-steady state region indicating that the amount of charge associated with the reduction of the film increases with the potential of its formation. This increase in charge clearly shows that there is an increase in resistive material (i.e. deposition of an insulating film) at oxidized sites.

However, the CSV in Figure 8.8, clearly shows that more than one film is present. This is consistent with previously published data by Sunder et al. [63].

They observed that initially a film of composition $UO_{2.33}$ formed, followed by its conversion to a deposited layer of $UO_3.2H_2O$. They also observed that both films, particularly the deposited layer, thicken with the time spent at a constant potential, even for E = 0.1 V. The increase in the size of the reduction peak in the CSV (Figure 8.8) confirms that both the $UO_{2.33}$ film and the deposited $UO_3.2H_2O$ film thicken with potential over the non-steady state region.

The high value of the U^{VI} to U^{IV} ratio obtained by XPS analysis after anodic oxidation at 0.1 V for a duration of 20 hours (Table 6.1) offers clear evidence that a U^{VI} phase ($UO_3.2H_2O$ in $NaClO_4$) is present.

Since at least two films are present, the log i - log t behaviour can not be interpreted according to the scheme shown in Figure 8.17D. Therefore, an interpretation according to the scheme shown in Figure 8.17E would be more appropriate. Using the scheme in Figure 8.17E, a film of $UO_{2.33}$ grows by HFIC,

$$UO_2 + 0.33H_2O \rightarrow UO_{2.33} + 0.66H^+ + 0.66e \qquad (2.1)$$

and is subsequently dissolved to yield a supersaturated UO_2^{2+} solution at the electrode surface,

$$UO_{2.33} + 0.33H^+ \rightarrow UO_2^{2+} + 0.33OH^- + 1.34e \qquad (2.2)$$

The UO_2^{2+} results in the deposition of a $UO_3.2H_2O$ layer,

$$UO_2^{2+} + 3H_2O \rightarrow UO_3.2H_2O + 2H^+ \qquad (2.4)$$

At short times in Figure 8.1, the first stage of film growth (i.e. UO_2 to $UO_{2.33}$) is not observed, only the second stage (i.e. $UO_{2.33}$ to $UO_3.2H_2O$) is observed. A possible explanation for this is that a process such as that shown in Figure 8.17A, would be rapid due to the high current, which would flow initially,

and expected to quickly reach a limiting film thickness since the oxygen can not penetrate deep into the solid UO_2 surface. Consequently, the current decay for the growth of this thin layer could be over in a few seconds, especially at the very positive potentials that are being applied, and hence, would not be observed in the current-time plots.

Within a short period of time the log current in Figure 8.1 ($E < 0.425$ V) changes from almost steady state to definitely decaying and has the form shown schematically in Figure 8.17D. Previous work by Sunder et al. [63] shows that the dual surface layer of $UO_{2.33}$ and $UO_3.2H_2O$ grows as the current decays and is independent of electrode rotation rate, with the amount of $UO_3.2H_2O$ increasing more rapidly than that of $UO_{2.33}$.

The CSV's in Figure 8.8 clearly show that the peak due to the reduction of $UO_3.2H_2O$ (Peak VI) becomes dominant over the peak for $UO_{2.33}$ (Peak V) reduction as the potential of oxide formation increases. This sequence of events is consistent with the rapid growth of a film ($UO_{2.33}$) which undergoes electrochemical dissolution (as UO_2^{2+}). The subsequent precipitation of the dissolution product (as $UO_3.2H_2O$) leads to a blockage of the dissolution process and hence, to a decay in current. Since the decay in current is independent of the electrode rotation rate, Sunder et al. concluded that the deposition was occurring at occluded sites, from which transport rates would be unaffected by electrode rotation rate. They speculated that these occluded sited were located at grain boundaries.

However, the SEM photomicrograph of the electrode anodically oxidized

at 0.425 V (Figure 7.4) clearly shows that dissolution sites are widely distributed across the electrode surface and are not preferentially located at grain boundaries. This general dissolution process leads to the general deposition of $UO_3.2H_2O$ which blocks dissolution from all surface sites, not just those sites located at grain boundaries.

A second piece of evidence which clearly demonstrates that the current decay is due to the deposition of dissolved U^{VI} is observed in the current transients recorded at 0.375 V in fresh solutions and solutions saturated with dissolved uranium (Figure 8.18). These transients show that the switch from stage B (Figure 8.17E) behaviour, the tendency to achieve steady state, to stage C behaviour, the tendency to decrease, depends on the concentration of U in the solution. This suggests that a primary driving force for the deposition of U^{VI} solids is the degree of saturation of the solution.

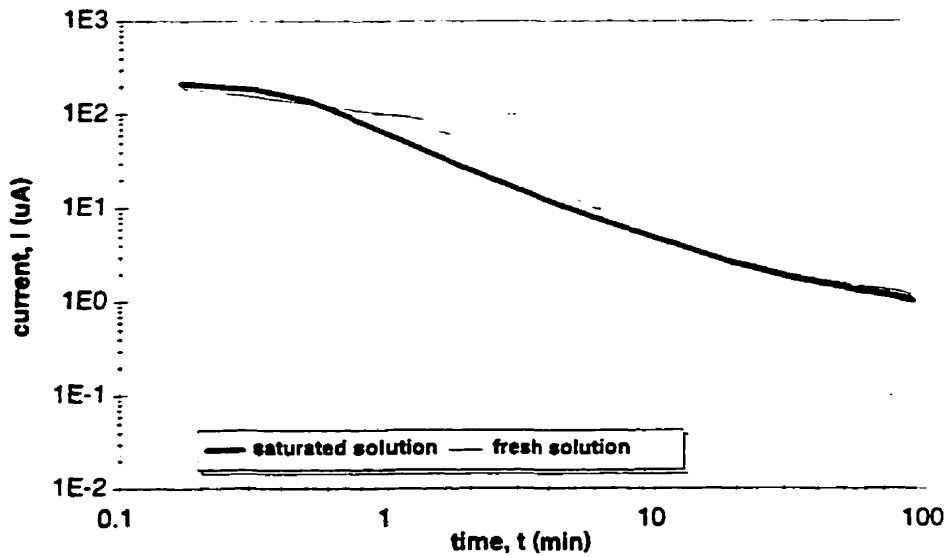

FIGURE 8.18: Plot of current as a function of time after anodic oxidation at 0.375 V in a fresh $NaClO_4$ solution and a $NaClO_4$ solution saturated with dissolved uranium.

The current transients confirm that the anodic behaviour in the non-steady state region can be viewed according to that suggested schematically in Figure 8.17E which is a combination of 8.17C and 8.17D. Furthermore, a primary driving force for the deposition of U^{VI} solids occurs when general supersaturation of the bulk solution occurs, not local supersaturation at individual dissolution sites. This is clearly shown in the SEM photomicrograph (Figure 7.4) which illustrates that the grain boundaries are not preferentially attacked.

For $E \geq 0.425$ V in Figure 8.1, the current - time transients reach a steady state (i.e. the rate of $UO_{2.33}$ film formation = the rate of its oxidative dissolution as UO_2^{2+}) and should have the form illustrated in Figure 8.17C (i.e. film formation leading to dissolution).

In this steady state region, Sunder et al. [63] found that the dissolution/hydrolysis/acidification rate is sufficiently rapid to establish local acidity when oxidation is occurring at high potential (Reactions 2.4and 2.5). This acidity leads to an increase in the local solubility of U^{VI} which is then transported away from the dissolution site,

$$UO_2 \rightarrow UO_{2.33} \rightarrow (UO_2^{2+})_{ads} \rightarrow (UO_2^{2+})_{soln} \qquad (8.1)$$

rather than deposited as $UO_3.2H_2O$.

The current - time transients (Figure 8.1), the CSV's (Figure 8.8) and the low Qc values (Figure 8.15) are consistent with this explanation. When high steady state dissolution currents are observed (i.e. $E \geq 0.425$ V) the corresponding CSV shows only the presence of a thin layer of $UO_{2.33}$; i.e. the

deposited $UO_3.2H_2O$ which blocks dissolution is not present. The low Qc values indicate a decrease in deposited material at oxidized sites.

The SEM (Figure 7.8) taken after anodic oxidation at 0.55 V, clearly shows that, under steady state dissolution conditions, general attack of the surface occurs with a number of localized sites experiencing severe pitting. Also, no deposited film is present. The localized pits clearly indicate that acidic conditions are established leading to extensive localized dissolution. Furthermore, this local acidity does not occur preferentially at grain boundaries.

However, previous evidence [15] suggests that the $UO_{2.33}$ film does not form in acidic solutions (pH < 5) and that dissolution proceeds through a U^{VI} species on the UO_2 surface. If this is true, why is a reduction peak for $UO_{2.33}$ observed under what is believed to be acidified conditions? A possibility is that the pH across the surface varies from site to site, more acidic conditions prevailing in the etched and pitted sites than on the general surface. The SEM photomicrographs at 0.425 V and 0.55 V offer evidence to support this due to the formation of holes, which could develop local acidity.

The transition from a deposit - covered surface to one dissolving steadily (E = 0.425 V) is clearly demonstrated by the fall in Qc for anodic potentials above 0.425 V, Figure 8.15, which corresponds to the increase in anodic current to yield steady state log i- log t plots (Figure 8.1) as opposed to non-steady state plots. The disappearance of the deposited film ($UO_3.2H_2O$) where this transition occurs, is clearly indicated in the CSV's recorded after anodic oxidation (Figure 8.8).

In the transition region, the behaviour is unpredictable; i.e. sometimes a

decaying non-steady state current is observed (Figure 8.6), and sometimes steady state behaviour is observed (Figure 7.1).

In this transition region, whether steady state is established depends on a combination of H^+ and U^{VI} (UO_2^{2+}) species concentrations. Both concentrations will increase as the dissolution current increases. An increase in H^+, due to the rapid hydrolysis of dissolved UO_2^{2+}, will increase the solubility of $UO_3.2H_2O$, (equations 2.5, 2.6 and 2.7),

$$2UO_2^{2+} + 2H_2O \rightarrow (UO_2)_2(OH)_2^{2+} + 2H^+ \quad (2.5)$$

$$3UO_2^{2+} + 5H_2O \rightarrow (UO_2)_3(OH)_5^{+} + 5H^+ \quad (2.6)$$

$$UO_3.2H_2O + 2H^+ \rightarrow UO_2^{2+} + 3H_2O \quad (2.7)$$

Conversely, an increase in U^{VI} (UO_2^{2+}) will lead to saturation with respect to U^{VI} and the rapid nucleation and growth of the deposited film (equations 2.2 and 2.4),

$$UO_{2.33} + 0.33H^+ \rightarrow (UO_2^{2+})_{ads} + 0.33OH^- + 1.34e \rightarrow (UO_2^{2+})_{soln} \quad (2.2)$$

$$UO_2^{2+} + 3H_2O \rightarrow UO_3.2H_2O + 2H^+ \quad (2.4)$$

This is clearly demonstrated in the current - time transients recorded for anodic oxidation at 0.45 V in fresh $NaClO_4$ solution (low U^{VI}) when reaction proceeds via steps 2.2 and 2.5 to 2.7, and in saturated solution (high U^{VI}) when reaction proceeds via steps 2.2 and 2.4 (Figure 8.19).

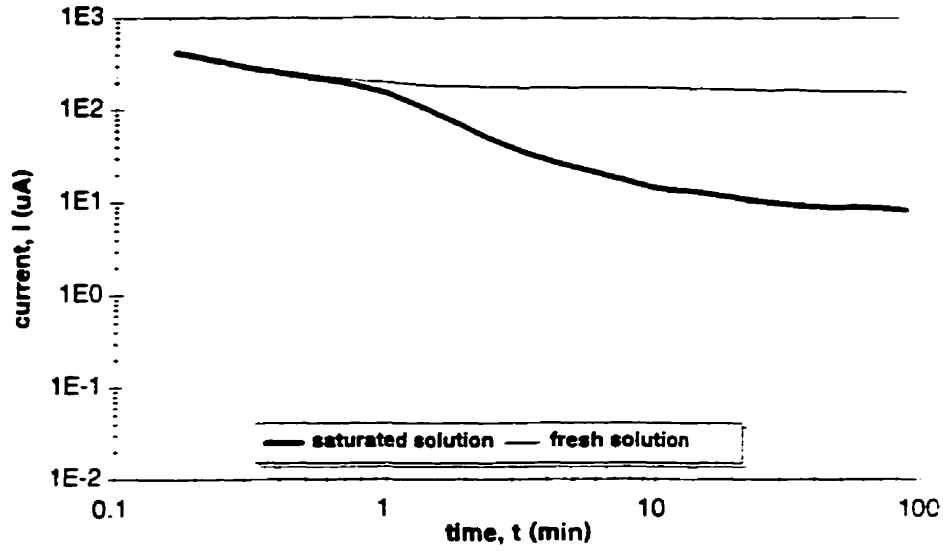

FIGURE 8.19: Plot of current as a function of time after anodic oxidation at 0.45 V in a fresh $NaClO_4$ solution and a $NaClO_4$ solution saturated with dissolved uranium.

Consequently, the unpredictable behaviour in this region is not surprising. Sunder et al [63] also observed this unpredictability in two different UO_2 specimens with a transition region in the potential range from 0.3 to 0.4 V.

NaCl

The similarities and differences between NaCl and $NaClO_4$ will be compared at 0.1 V in the non-steady state region, at 0.55 V in the steady state region and at 0.425 V, the transition region.

In the non-steady state region, the current-time transients (Figure 8.5) are effectively identical in both solutions and have the form illustrated schematically in Figure 8.17D (i.e. dissolution followed by deposition of a film which blocks

dissolution). The CSV recorded in NaCl is also very similar to that recorded in $NaClO_4$ (Figure 8.12) which shows that the film of $UO_{2.33}/UO_3.2H_2O$ formed is similar in both solutions. The presence of a $UO_3.2H_2O$ film is confirmed by the XPS data recorded after anodic oxidation at 0. 1 V (Table 6.1). The U^{VI} to U^{IV} ratio is large for specimens oxidized in both solutions. Since at least two films are present, the log i – log t behaviour must be interpreted according to the scheme shown in Figure 8.17E (i.e. a combination of 8.17C and 8.17D) and oxidation follows the same sequence as in $NaClO_4$.

In the steady state region, the current-time transients (Figure 8.7) for NaCl and $NaClO_4$ are again effectively identical. Also, the CSV's are similar for the two solutions and show only a thin layer of $UO_{2.33}$ present on the electrode surface. The CSV results are supported by the XPS results. The U^{VI}:U^{IV} ratios recorded after anodic oxidation at 0.5 V (Table 6.1), indicate that a much lower amount of U^{VI} is present on the UO_2 surfaces than observed for potentials in the non-steady state region.

A final piece of evidence to show the similarities in oxidation behaviour in NaCl and $NaClO_4$ is observed in the SEM photomicrographs (Figures 7.8 and 7.10). The photomicrographs show that after anodic oxidation in both solutions, the surfaces are generally attacked with a high density of locally etched sites. All of the above similarities for oxidation behaviour in NaCl and $NaClO_4$ at high potentials, (i.e. in the steady state region) indicate that identical acidic conditions are established in both solutions and oxidation and dissolution follows the sequence of reactions outlined in the reaction scheme, 8.1.

In the transition region (E = 0.425 V) the Qc - E plot (Figure 8.15) clearly shows similar behaviour in $NaClO_4$ and NaCl. However, two sets of experiments at 0.425 V yield quite different behaviours in both solutions. In one experiment, Figure 8.6, non-steady state behaviour is observed in $NaClO_4$, whereas in NaCl the behaviour is closer to steady state. In the second experiment, Figure 7.1, the behaviour is reversed.

SEM photomicrographs confirm that a surface deposit accumulates for the non-steady state experiment in NaCl (Figure 7.6). Conversely, the steady state experiment in $NaClO_4$ clearly shows that the surface is free of surface deposits and is in fact generally attacked with local etched sites, as observed at 0.55 V. While this confirms that the non-steady state behaviour can be attributed to the formation of a $UO_3.2H_2O$ deposit which blocks dissolution, it does not show that there is any significant difference in anodic oxidation behaviour in NaCl and $NaClO_4$.

It would appear that the differences observed in the transition region are due to the unpredictable behaviour in the transition, not differences between NaCl and $NaClO_4$.

SCSSS

In the non-steady state region, the current - time transients (Figure 8.5) are similar in $NaClO_4$, NaCl and SCSSS. However, the form of the CSV's (Figure 8.12) confirms the preliminary observations made by the cyclic voltammetry (Figure 5.3); that the nature of the product formed on the surface of the

electrode is different in SCSSS compared to that formed in $NaClO_4$ and NaCl.

The XPS results recorded after anodic oxidation at 0.1 V for 20 hours (Table 6.1) confirm this difference. The U^{VI}:U^{IV} ratio suggests that only a surface film consisting of $UO_{2.33}$ is present, consistent with the absence of a $UO_3.2H_2O$ deposit to block dissolution. The XPS also indicates that substantial amounts of calcium and silicon are present. The presence of calcium and silicon may rapidly block the dissolution / deposition process by being incorporated into the U^{VI} solid. If this U^{VI} solid was a very thin film, the XPS would see predominantly the underlying $UO_{2.33}$ layer and the U^{VI}:U^{IV} ratio would be lower than expected.

The reduction peak present in the CSV (Figure 8.12) has a lower peak current, is broader and displaced to a more negative potential than that recorded in the CSV for $NaClO_4$. However, these CSV's were recorded after only short anodic oxidations, whereas the XPS results were observed after anodic oxidation for 20 hours.

Therefore, a comparison of the log i - log t plots after anodic oxidation for 20 hours (Figure 6.1) and 90 minutes (Figure 8.5) must be made. The current - time transient for anodic oxidation for 20 hours has a final current, which is a factor of 10 lower than that after 90 minutes. This continued decay in current indicates that the growth of the surface film that blocks dissolution continues. Tait et al. [88] observed a decrease in dissolution rate of UO_2 in the presence of Ca^{2+} and SiO_4^{4-}, both constituents of SCSSS. They also found that both ions were strongly adsorbed or incorporated into a precipitated phase on the UO_2 surface since it took several weeks to restore the dissolution rate after removing

Ca^{2+} and SiO_4^{4-} from the solution. Hence, the low current, the CSV and the XPS results confirm that calcium and silicon are incorporated into the surface phases blocking the oxidation / dissolution process.

In the steady state region ($E \geq 0.425$ V), the current - time transients are effectively identical for all three solutions; $NaClO_4$, NaCl and SCSSS. The CSV's recorded after anodic oxidation at 0.55 V, Figure 8.14, are also similar but with the reduction peak for SCSSS lower and positioned at less negative potentials than observed for NaCl and $NaClO_4$. These relative peak sizes and positions suggest that slightly more deposited film may be present after anodic oxidation in the latter two solutions compared to SCSSS.

The XPS results for oxidation at 0.5 V (Table 6.1) confirm that the surface consists primarily of $UO_{2.33}$. Only small amounts of silicon are incorporated into the surface compared to the behaviour in the non-steady state region. The SEM photomicrograph after anodic oxidation at 0.55 V (Figure 7.9) clearly indicates that the surface is generally attacked with a high density of locally etched sites in a similar manner to oxidation in $NaClO_4$ (Figure 7.8) and NaCl (Figure 7.10). Since only small to insignificant amounts of deposited film are present, the absence of silicon is not surprising.

Consequently, the similarities at high potentials indicate that identical acidic conditions are established in all three solutions. Once these acidified local conditions are established, the deposition of silicon-containing U^{VI} phases is prevented; i.e. the exact composition of the bulk solution becomes irrelevant once local acidification is established.

The Qc - E plot (Figure 8.15) and the log i - E plot (Figure 8.16) show that the transition from non-steady state film deposition to dissolution at acidified sites is delayed in SCSSS until a much higher potential is reached and that the transition is more gradual than for NaCl and $NaClO_4$. The delayed and more gradual nature of the transition indicated in the log i - E plot is most likely due to the calcium/silicon containing U^{VI} deposit blocking the surface.

The reduction peak observed in the CSV after anodic oxidation at 0.425 V in SCSSS (i.e. in the transition region) is very broad by comparison to those recorded in the other solutions (Figure 8.13) and reduction of the deposited U^{VI} phase is almost certainly incomplete by the potential at which integration of the profile is terminated (i.e. at the minimum in the cathodic current after the reduction peak, Section 5.1.3). It is possible that such an underestimation accounts for the lower Qc values observed as a function of oxidation potential, Figure 8.15.

The height of peak V, due to $UO_{2.33}$ reduction, is generally lower in proportion to the amount of U^{VI} oxide available for reduction (Peak VI) compared to other solutions. The width of the reduction peak suggests that the U^{VI} oxide is not so readily reduced as that formed in $NaClO_4$ and NaCl. This could mean that it is not in good conductive contact with the UO_2, but since it is very effective in blocking dissolution, this seems unlikely. More likely, it is of different composition due to the incorporation of Ca and/or Si ions. The incorporation of these ions could lead to the deposition of a less soluble U^{VI} phase, accounting for the more persistent blockage of the dissolution process, and the more negative potential

required for its reduction.

SCSSS + HCO_3^-

In the non-steady state region, the log i - log t plots (Figure 8.5) are effectively the same in SCSSS + HCO_3^- as observed in SCSSS. This similarity indicates that the addition of bicarbonate, expected to accelerate dissolution (as discussed in Section 2.4.6.2) by complexing UO_2^{2+}, does not prevent the deposition of calcium/silicon containing U^{VI} phases in SCSSS. By contrast, even at 0.1 V (Figure 8.20), the addition of HCO_3^- to $NaClO_4$ leads to a higher current than observed in $NaClO_4$ alone. Clearly, this concentration (10^{-2} mol.L^{-1}) of HCO_3^- is insufficient to counterbalance the influence of the calcium and silicon content of SCSSS at this relatively low anodic oxidation potential.

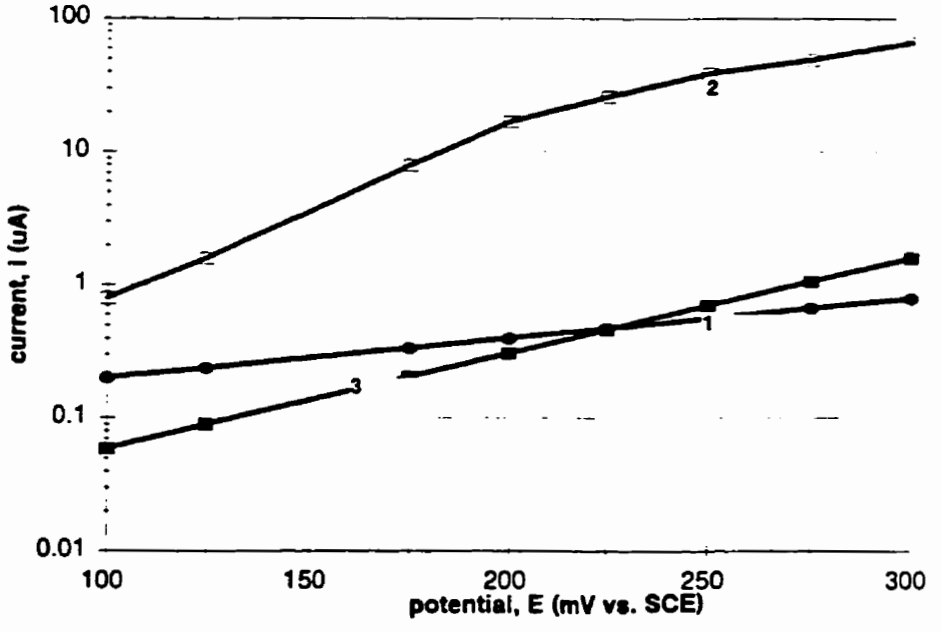

FIGURE 8.20: Plot of current as a function of potential after anodic oxidation in (1) $NaClO_4$ (2) $NaClO_4$ + HCO_3^-, and (3) SCSSS + HCO_3^-.

The similarity in the current-time transients in all four solutions in the non-steady state region (Figure 8.5) suggests that the rate determining step may be similar in all solutions. At this potential, the formation rate of UO_2^{2+} would be expected to be slow, i.e.,

$$UO_2 \rightarrow UO_{2.33} \rightarrow UO_2^{2+} \qquad (8.4)$$

Consequently, the subsequent rate of deposition of the U^{VI} phase should be roughly the same in all solutions,

$$UO_2^{2+} \rightarrow UO_3.2H_2O \qquad (8.5)$$

However, the addition of bicarbonate could have two effects:

(i) by complexing UO_2^{2+}, it could prevent its redeposition as a U^{VI} - containing deposit which then blocks the dissolution process;

(ii) it could accelerate the slow oxidative dissolution step resulting in a thinner layer of $UO_{2.33}$ and a higher dissolution current [73, 88].

In $NaClO_4$ solutions, the higher anodic oxidation current at 0.1 V (Figure 8.20) indicates that both of these processes occur on addition of bicarbonate. By contrast, in SCSSS, although the CSV's at 0.1 V (Figure 8.12) shows a thinner film in SCSSS + HCO_3^- than in SCSSS alone, the oxidation current is suppressed (Figure 8.20), indicating that the kinetics of deposition of a calcium / silicon containing U^{VI} phase are sufficiently rapid to prevent complexation and accelerated dissolution by HCO_3^-.

However, as the anodic potential is increased, the ability of bicarbonate to accelerate dissolution at the expense of deposition is enhanced. This is shown

by the attainment of steady state currents at lower potentials in SCSSS + HCO_3^- than in the other solutions, and by the observation that Qc does not increase with anodic oxidation potential (Figures 8.15 and 8.16).

The ability of calcium and silicon to suppress dissolution is not completely overcome by the addition of this amount of bicarbonate. This is shown in Figure 8.20 in which the steady state currents are higher when calcium and silicon are absent (i.e., in $NaClO_4$) than when they are present (i.e., in SCSSS).

The SEM offers further evidence that a calcium/silicon containing U^{VI} phase was present even after anodic oxidation at 0.425 V. The photomicrograph of the surface after anodic oxidation in SCSSS + HCO_3^- (Figure 7.7) has areas with a similar matte finish to the surface observed after anodic oxidation in SCSSS alone (Figure 7.5), while other areas show the same general etching pattern observed after anodic oxidation in either $NaClO_4$ or NaCl (Figures 7.4 and 7.6).

At high potentials, in the steady state region, the behaviour is similar in all four solutions (i.e. the CSV's in Figure 8.14 and log i - log t plots in Figure 8.7), suggesting that at potentials > 0.5 V, the development of local acidity occurs in a similar manner for all four solutions. It would appear that this concentration of HCO_3^- is insufficient to buffer the local pH at the dissolving UO_2 surface.

9.0 SUMMARY AND CONCLUSIONS

The anodic dissolution of UO_2 was studied in simple electrolyte solutions ($NaClO_4$ and NaCl) and complex electrolyte solutions (SCSSS and SCSSS + HCO_3^-) using potentiostatic and cyclic voltammetry. Under potentiostatic conditions, the anodic oxidation of UO_2 in $NaClO_4$, NaCl, SCSSS and SCSSS + HCO_3^- solutions can be divided into two regions.

(1) In the non-steady state region ($E \leq 0.425$ V) the UO_2 surface is covered by the formation of surface films which block the oxidative dissolution process. The XPS and SEM results show that the UO_2 surface becomes covered by a thin film of $UO_{2.33}$ and a thicker deposited layer of a U^{VI} solid which was distributed uniformly over the surface. This general dissolution process leads to the general deposition of U^{VI} solid which blocks dissolution from all surface sites, not just those sites located at grain boundaries.

In $NaClO_4$ and NaCl solutions, the U^{VI} solid is a $UO_3.2H_2O$ deposit, while in SCSSS and SCSSS + HCO_3^- solutions the U^{VI} solid contains calcium and silicon ions which lead to a more rapid blocking of the dissolution / deposition process by their incorporation into the U^{VI} solid.

The rate determining step in this region is similar for all four solutions. At $E \leq 0.425$ V, the formation rate of UO_2^{2+} would be expected to be slow, i.e.,

$$UO_2 \rightarrow UO_{2.33} \overset{\text{slow}}{\rightarrow} UO_2^{2+}$$

Consequently, the subsequent rate of deposition of the U^{VI} phase should be roughly the same in all four solutions,

$$UO_2^{2+} \rightarrow U^{VI}_{solid}\ (UO_3.2H_2O \text{ in } NaClO_4)$$

The kinetics of deposition of a calcium / silicon containing U^{VI} phase are sufficiently rapid to prevent complexation and accelerated dissolution by HCO_3^-.

(2) In the steady state region ($E \geq 0.425$ V) the rate of $UO_{2.33}$ film formation becomes equal to the rate of its oxidative dissolution as UO_2^{2+}. The dissolution / hydrolysis / acidification rate is sufficiently rapid to establish local acidity when oxidation is occurring at high potentials. This local acidity leads to an increase in solubility of U^{VI} which is then transported away from the dissolution site as UO_2^{2+}, rather than depositing on the surface as a U^{VI} solid,

$$UO_2 \rightarrow UO_{2.33} \rightarrow (UO_2^{2+})_{ads} \rightarrow (UO_2^{2+})_{soln}$$

The SEM examination confirms that this local acidity does not occur preferentially at grain boundaries.

For anodic oxidation in $NaClO_4$ and NaCl solutions, attainment of steady state differs only due to the unpredictable behaviour in the transition from a deposited covered surface to one dissolving steadily. For anodic oxidation in SCSSS, achievement of steady state requires a higher potential than for $NaClO_4$ and NaCl. Once the local acidified conditions associated with the steady state are established, the deposition of calcium / silicon containing U^{VI} phases is prevented. For anodic oxidation in SCSSS + HCO_3^-, steady state occurs at lower potentials than the other three solutions. Therefore the ability of HCO_3^- to

accelerate dissolution at the expense of deposition is enhanced. However, the ability of calcium and silicon to suppress dissolution is not completely overcome by the addition of 10^{-2} mol.L^{-1} HCO_3^-.

Considering the results of this thesis, the proposed mechanism for the electrochemical oxidative dissolution of UO_2, given in Section 2.4.5, for solutions containing simple electrolytes ($NaClO_4$ and NaCl) is verified. For more complex electrolyte solutions (SCSSS and SCSSS + HCO_3^-), the proposed mechanism follows the same reaction pathway as that for simple electrolyte solutions. The main differences between complex and simple electrolyte solutions are the U^{VI} phase formed, and the potential at which the oxidative dissolution threshold is achieved.

ACKNOWLEDGEMENTS

I would like to begin by thanking my supervisor, Dr. Dave Shoesmith, for help and guidance throughout my M.Sc. project, for creating a learning experience and increasing my knowledge in electrochemistry and science.

Next, I would like to thank Drs. Peter Sargent and John Tait for the opportunity to work on my M.Sc. project at AECL in Pinawa, Manitoba.

The majority of the credit for my practical electrochemical training belongs to Jim Betteridge who graciously allowed me the use of his equipment and laboratory.

Thanks to all members of the Electrochemistry and Corrosion Science Section at AECL for beneficial interaction throughout my project.

The technical assistance of Neil Miller (XPS data) and Rick Kaatz (SEM photomicrographs) is acknowledged.

Finally, thanks to Lesa Cafferty, the glass blower, for fabricating equipment and Sheldon Swenson, the graphics illustrator, for professionally drawing some of my graphics.

This work is part of the Nuclear Fuel Waste Management Program which is jointly funded by AECL and Ontario Hydro under the auspices of the CANDU Owners Group.

REFERENCES

[1] Shoesmith, D.W., B.M. Ikeda, F. King, S. Sunder. 1996. Prediction of long-term behaviour for nuclear waste disposal. Atomic Energy of Canada Limited Report, AECL-11580.

[2] Shoesmith, D.W. and S. Sunder. 1992. The prediction of nuclear fuel (UO_2) dissolution rates under waste disposal conditions. J. Nucl. Mater., 190, 20.

[3] Lemire, R.J. and P.R. Tremaine. 1980. Uranium and plutonium equilibria in aqueous solutions to 200°C. J. Chem. Eng. Data 25, 361.

[4] Paquette, J. and R.J. Lemire. 1981. A description of the chemistry of aqueous solutions of uranium and plutonium to 200°C using potential-pH diagrams. Nucl. Sci. Eng., 79, 26.

[5] Garisto, F. and N. C.Garisto. 1985. A UO_2 solubility function for the assessment of used nuclear fuel. Nucl. Sci. Eng., 90,103.

[6] Lemire, R.J. and F. Garisto. 1989. The Solubility of U, Np, Pu, Th and Tc in a Geological Disposal Vault for Used Nuclear Fuel. Atomic Energy of Canada Limited Report, AECL-10009.

[7] Garisto, N.C. and D.M. Leneveu. 1988. A vault model for the assessment of used fuel disposal in Canada. Mat. Res. Soc. Sym. Proceed., 112, 313.

[8] Goodwin B.W., R.J. Lemire and L.H. Johnson. 1982. A stochastic model for the dissolution of irradiated UO_2 fuel. Canadian Nuclear Society

International Conference on Radioactive Waste Management, Conference Proceedings, Winnipeg, MB, 1982, 298.

[9] Garisto, N.C. and F. Garisto. 1986. The dissolution of UO_2: a thermodynamic approach. Nucl. Chem. Waste Manage. 6, 203.

[10] Barner, J.O., W.J. Gray, G.L. McVay and J.W. Schade. 1986. Interactive leach tests of UO_2 and spent fuel with waste package components in salt brine. Pacific Northwest Laboratory Report, PNL-4898-SRP.

[11] Wronkiewicz, D.J., J.K. Bates, T.J. Gerding, E. Veleckis and B.S. Tani. 1992. Uranium release and secondary phase formation during unsaturated testing of UO_2 at 90°C. J. Nuc. Mater. 190, 107.

[12] Johnson, L.H. and D.W. Shoesmith. 1988. Spent Fuel. In Radioactive Waste Forms for the Future (W. Lutze and R.C. Ewing, editors). Elsevier Science Publishers B.V.,635-698.

[13] Sunder, S. and D.W. Shoesmith. 1991. Chemistry of UO_2 fuel dissolution in relation to the disposal of used nuclear fuel, Atomic Energy of Canada Limited Report, AECL-10395.

[14] Shoesmith, D.W., S. Sunder. 1991. An electrochemistry based model for the dissolution of UO_2. Atomic Energy of Canada Limited Report, AECL-10488.

[15] Sunder S., D.W. Shoesmith, R.J. Lemire, M.G. Bailey and G.J. Wallace. 1991. The effect of pH on the corrosion of nuclear fuel (UO_2) in oxygenated solutions. Corrosion Science 32, 373.

[16] Shoesmith, D.W., S. Sunder and W. H. Hocking. 1994. Electrochemistry of UO_2 nuclear fuel. In Electrochemistry of Novel Materials (editors, J. Lipkowski and P.N. Ross) VCH Publishers Inc., New York, 297.

[17] Grambow, B. 1989. Used fuel dissolution and oxidation. An evaluation of literature data. SKB Technical Report, SKB 89.

[18] Needes, C.R.S., M.J. Nicol and N.P. Finkelstein. 1975. Electrochemical model for the leaching of uranium dioxide:2 - Alkaline carbonate media. In Leaching and Reduction in Hydrometallurgy (A.R. Burkin, editor). Inst. Min. Metall., London, U.K., 12.

[19] Nicol, M.J. and C.R.S. Needes. 1975. The anodic dissolution of uranium dioxide - 1. In perchlorate solutions. Electrochimica Acta 20, 585.

[20] Nicol, M.J., C.R.S. Needes and N.P. Finkelstein. 1975. Electrochemical model for the leaching of uranium dioxide: 1 - Acid media. In Leaching and Reduction in Hydrometallurgy (A.R. Burkin, editor). Inst. Min. Metall., London, U.K., 1.

[21] Shoesmith, D.W. , S. Sunder, M.G. Bailey and G.J. Wallace. 1989. The corrosion of nuclear fuel (UO_2) in oxygenated solutions. Corrosion Science 29, 1115.

[22] Rudnicki, J.D., R.E.Russo and D.W. Shoesmith. 1994. Photothermal deflection spectroscopy investigations of uranium dioxide oxidation. J. Electroanal. Chem. 372, 63.

[23] Shoesmith, D.W., W.H. Hocking, S. Sunder, J.S. Betteridge and N. H. Miller. 1994. Electrochemical studies of SIMFUELs. J. Alloys and Comps. 213/214, 551.

[24] Sunder, S., D.W. Shoesmith, M.G. Bailey, F.W. Stanchell and N.S. McIntyre. 1981. Anodic oxidation of UO_2 - Part 1. Electrochemical and X-ray photoelectron spectroscopic studies in neutral solutions. J. Electroanal. Chem. 130, 163.

[25] Hocking, W.H., D.W. Shoesmith and J.S. Betteridge. 1992. Reactivity effects in the oxidative dissolution of UO_2 nuclear fuel. J. Nucl. Mater. 190, 36.

[26] Belle, J. 1980. Uranium dioxide properties and nuclear applications. J. Ed., AEC-USA, Washington, DC.

[27] Matzke, Hj. 1986. Adv. Ceram., 17, 1.

[28] Matzke, Hj. 1986. Science of advanced LMFBR fuels. Elsevier, Amsterdam.

[29] Kleykamp, H. 1985. J. Nucl. Mater., 131, 221.

[30] Matzke, Hj. 1987. Radiat. Effects, 64, 3.

[31] Matzke, Hj. 1988. Nucl. Instrum. Methods Phys. Res., B32, 455.

[32] Matzke, Hj. 1987. Atomic transport properties in UO_2 and mixed oxides (U, Pu) O_2. J. Chem. Soc. Faraday Trans. 2, 83, 1121.

[33] Matzke, Hj. 1980. Radiat. Effects, 53, 219.

[34] Matzke, Hj. 1990. J. Chem. Soc. Faraday Trans., 86, 1257.

[35] Ball, R.J. and R.W. Grimes. 1990. J. Chem. Soc. Faraday Trans., 86, 1257.

[36] Grimes, R.W. and Catlow C.R.A. 1991. J. Chem. Soc. London, 335A, 609.

[37] Thomas, L.E. and Charlot, L.A. 1990. Analytical electron microscopy of light-water reactor fuels. Ceram. Trans., 9, 397.

[38] Une, K., Tominga, Y. and Kashibe, S. 1991. J. Nucl. Sci. Technol., 28, 409.

[39] Matzke, Hj., Ottaviani, J., Pellottiero, D. and Roualt, J. 1988. J. Nucl. Mater., 160, 142.

[40] Killeen, J.C. 1980. The effect of niobium oxide additions on the electrical conductivity of UO_2. J. Nucl. Mater., 88, 185.

[41] Dudney, N.J., Coble, R.L. and Tuller, H.L. 1981. J. Amer. Ceram. Soc., 64, 627.

[42] Hyland, G.J. and Ralph, J. 1983. Electronic contributions to the high-temperature thermophysical properties of UO_{2+x} : A critical analysis. J. High Temp.-High Press., 15, 179.

[43] Winter, P.W. 1989. The electronic transport properties of UO_2. J. Nucl. Mater., 161, 38.

[44] Aronson, S., J.E. Rulli and B.E. Schaner. 1961. Electrical properties of non-stoichiometric uranium dioxide. J. Chem. Phys., 35, 1382.

[45] Memming, R. 1983. Processes at semiconductor electrodes. In Comprehensive Treatise of Electrochemistry, eds. B.E. Conway, J.O'M.

Bockris, E. Yeager, S.U.M. Khan and R.E. White, Vol. 7 (Plenum, New York) p. 529.

[46] Hocking, W.H., J.S. Betteridge and D.W. Shoesmith. 1991. The mechanism of oxygen reduction on UO_2. Atomic Energy of Canada Limited Report, AECL-10402.

[47] Gronvold, F. 1955. High-temperature x-ray study of uranium oxides in the UO_2-U_3O_8 region. J. Inorg. Nucl. Chem. 1, 357-370.

[48] Willis, B.T.M. 1987. Crystallographic studies of anion-excess uranium oxides. J. Chem. Soc. Faraday Trans. II, 83, 1073.

[49] Bevan, D.J.M., I.E. Gray and B.T.M. Willis. 1986. The crystal structure of β-U_4O_{9-y}. J. Solid State Chem., 61, 1.

[50] Willardson, R.K., J.W. Moody and H.L. Goering. 1958. The electrical properties of uranium oxides. J. Inorg. Nucl. Chem. 6, 19-33.

[51] Manes, L. and J. Naegele. 1976. On the electronic properties of actinide oxides. In Plutonium and Other Actinides (H. Blank and R. Linder, editors). North-Holland, Amsterdam, Netherlands, 361-382.

[52] Hoekstra, H.R. A. Santoro and S. Siegel. 1961. The low temperature oxidation of UO_2 and U_4O_9. J. Inorg. Nucl. Chem. 18, 166-178.

[53] Hoekstra, H.R., S. Siegel and F.X. Gallagher. 1970. The uranium-oxygen system at high pressure. J. Inorg. Nucl. Chem 32, 3237-3248.

[54] Smith, D.K., B.E. Scheetz, C.A.F. Anderson and K.L. Smith. 1982. Phase relations in the uranium-oxygen-water system and its significance on the solubility of nuclear waste forms. Uranium 1, 79.

[55] Dharwadkar, S.R., M.S. Chandrasekharaiah and M.D. Karkhanavala. 1978. A physiochemical study of the uranium-oxygen system between $UO_{2.65}$ to $UO_{2.67}$. J. Nucl. Mater. 71, 268.

[56] O'Hare, P.A.G., B.M. Lewis and S.N. Nguyen. 1988. Thermochemistry of uranium compounds. XVII. Standard molar enthalpy of formation at 298.15K of dehydrated shoepite $UO_{3.0}.9H_2O$. Thermodynamics of (schoepite + dehydrated schoepite + water). J. Chem. Thermodyn. 20, 1287.

[57] Hoekstra, H.R. and S. Siegel. 1973. The uranium trioxide-water system. J. Inorg. Nucl. Chem. 35, 761.

[58] Grenthe, I., J. Fuger, R.J.M. Konings, R.J. Lemire, A.B. Muller, C. Nguyen-Trung and H. Wanner. 1992. "Chemical Thermodynamics of Uranium, Volume 1, Chemical Thermodynamics," H. Wanner and I. Forest, editors, North Holland, Amsterdam.

[59] Mueller, T.R. and M. Petrek. 1986. In Encyclopedia of Electrochemistry of the Elements (editor, Bard, A.J.) Dekker, New York, Vol. IX, Part B.

[60] Lemire, R.J. 1988. Effects of high ionic strength groundwaters on calculated equilibrium concentrations in the uranium-water system. Atomic Energy of Canada Limited report, AECL-9549.

[61] McIntyre, N.S., S. Sunder, D.W. Shoesmith and F.W. Stanchell. 1981. Chemical information from XPS - applications to the analysis of electrode surfaces. J. Vac. Sci. Technol. 18, 714.

[62] Shoesmith, D.W., S. Sunder, M.G. Bailey, G.J. Wallace and F.W. Stanchell. 1984. Anodic oxidation of UO_2. Part IV. X-ray photoelectron spectroscopic and electrochemical studies of film growth in carbonate solutions. Appl. Surf. Sci. 20, 39.

[63] Sunder, S. L.K. Strandlund and D.W. Shoesmith. 1996. Anodic Dissolution of UO_2 in slightly alkaline sodium perchlorate solutions. Atomic Energy of Canada Limited Report, AECL-11440.

[64] Sunder, S., D.W. Shoesmith, H. Christensen, M.G. Bailey and N.H. Miller. 1989. Electrochemical and x-ray photoelectron spectroscopic stucdies of UO_2 fuel oxidation by specific radicals formed during radiolysis of groundwater. Mater. Res. Symp. Proc. 127, 317.

[65] Sunder, S., D.W. Shoesmith, M.G. Bailey and G.J. Wallace. 1983. Anodic oxidation of UO_2. Part III electrochemical and x-ray photoelectron spectroscopic studies in alkaline solutions. J. Electroanal. Chem. 150, 217.

[66] Shoesmith, D.W., S. Sunder, M.G. Bailey and D.G. Owen. Anodic oxidation of UO_2. Part III: Electrochemical studies in carbonate solutions. Atomic Energy of Canada Limited Report, AECL-7956.

[67] Sunder, S., N.H. Miller and GJ. Wallace. 1992. Determination of criteria for selecting a UO_2 dissolution model for the nuclear fuel waste management concept assessment. Mater. Res. Symp. Proc. 257, 345.

[68] Needes, C.R.S. and M.J. Nicol. 1973. A study of some redox reactions at a UO_2 surface, Report No. 7073 (Nat. Inst. Met. Repub. S. Afr.).

[69] Shoesmith, D.W. and G.M. Bailey, unpublished.

[70] Sunder, S., D.W. Shoesmith, M.G.Bailey and G.J. Wallace. 1982. Mechanism of oxidative dissolution of UO_2 under waste disposal vault conditions. In Canadian Nuclear Society International Conference on Radioactive Waste Management, Conference Proceedings, Winnipeg, MB, 1982, 398.

[71] Grenthe, I. D. Ferri, F. Salvatore and G. Riccio. 1984. Studies on metal carbonate equilbria. Part 10. A solubility study of the complex formation in the uranium (VI)-water-carbon dioxide (g) system at 25°C. J. Chem. Soc. Dalton Trans. 11, 2439.

[72] Shoesmith, D.W., S. Sunder, M.G. Bailey and G.J. Wallace. 1986. Mechanism of oxidation and dissolution of CANDU fuel. In Canadian Nuclear Society 2nd International Conference on Radioactive Waste Management, Conference Proceedings, Winnipeg, MB, 1986, 674.

[73] Shoesmith, D.W., S. Sunder, M.G. Bailey and N.H. Miller. 1996. Corrosion of used nuclear fuel in aqueous perchlorate and carbonate solutions. J. Nucl. Mater., 227, 287.

[74] Hocking, W.H., J.S. Betteridge and D.W. Shoesmith. 1994. The cathodic reduction of oxygen on uranium dioxide in dilute aqueous solution. J. Electroanal. Chem., 379, 339.

[75] Shoesmith, D.W., J.S. Betteridge and W.H. Hocking. 1996. The cathodic reduction of oxygen on n-type UO_2 in dilute alkaline aqueous solution. J. Electroanal. Chem., 406, 69.

[76] Betteridge, J.S., N.A.M. Scott, D.W. Shoesmith, L.E. Bahen, W.H. Hocking and P.G. Lucuta. 1996. Effects of hyperstoichiometry and fission products on the electrochemical reactivity of UO_2 nuclear fuel. Atomic Energy of Canada Limited Report, AECL-11647.

[77] Sunder, S., D.W. Shoesmith, N.H. Miller and G.J. Wallace. 1992. Determination of criteria for selecting a UO_2 fuel dissolution model for nuclear fuel waste management concept assessment. Mater. Res. Soc. Symp. Proc. 257, 345.

[78] Sunder, S., D.W. Shoesmith, H. Christensen and N.H. Miller. 1992. Oxidation of UO_2 fuel by the products of gamma radiolysis of water. J. Nucl. Mater. 190, 78.

[79] Sunder, S., D.W. Shoesmith, H. Christensen, N.H. Miller and M.G. Bailey. 1990. Oxidation of UO_2 fuel by radicals formed during radiolysis of water. Mater. Res. Soc. Symp. Proc. 176, 457.

[80] Bailey, M.G., L.H. Johnson and D.W. Shoesmith. 1985. The effects of the alpha radiolysis of water on the corrosion of UO_2. Corrosion Science 24, 233.

[81] Sunder, S., D.W. Shoesmith, L.H.Johnson, G.J. Wallace, M.G. Bailey and A.P. Snaglewski. 1987. Oxidation of CANDU fuel by the products of the alpha radiolysis of groundwater. Mat. Res. Soc. Symp. Proc. 84, 102.

[82] Nel, H.J. 1958. Discussion of the attrition of uraninite. Geol. Soc. S. Afr. Trans. 61, 194.

[83] Johnson, L.H., D.W. Shoesmith, G.E. Lunansky, M.G. Bailey and P.R. Tremaine. 1982. The mechanisms of leaching and dissolution of uranium oxide fuel. Nuclear Technology 26, 238.

[84] Johnson, L.H., D.M. LeNeveu, F. King, D.W. Shoesmith, M. Kolar, D.W. Oscarson, S.Sunder, C. Onofrei and J.L. Crosthwaite. 1996. The disposal of Canada's nuclear fuel water: A study of postclosure safety of in-room emplacement of used CANDU fuel in copper containers in permeable plutonic rock. Volume 2: Vault Model. Atomic Energy of Canada Limited Report, AECL-11494-2.

[85] Wilson, C.N. and W.J. Gray. 1990. Measurement of soluble nuclide dissolution rates from spent fuel. Scientific Basis for Nuclear Waste Management XIII. Mater. Res. Soc. Symp. Proc. 176, 489.

[86] Sunder, S. and N. H. Miller. 1996. Oxidation of CANDU uranium oxide fuel by air in gamma radiation at 150 °C. J. Nucl. Mater. 231, 121.

[87] Strandlund, L. K. and S. Sunder, unpublished.

[88] Tait, J. C. and J. L. Luht. 1997. Dissolution rates of uranium fom unirradiated UO_2 and uranium and radionuclides from used CANDU fuel using the single-pass flow-through apparatus. Ontario Hydro Report 06819-REP-01200.0006 R00.

[89] Lahalle, M. P., J. C. Krupa, R. Guillaumont, M. Genet, G. C. Allen and N. R. Holmes. 1989. Surface analysis of UO_2 leached in meneral water studied by X-ray photoelectron spectroscopy. Scientific Basis for Nuclear Waste Management XIII, eds. W. Lutze and R. C. Ewing, Mater. Res. Soc. Symp. Proc. 127, 351.

IMAGE EVALUATION
TEST TARGET (QA-3)

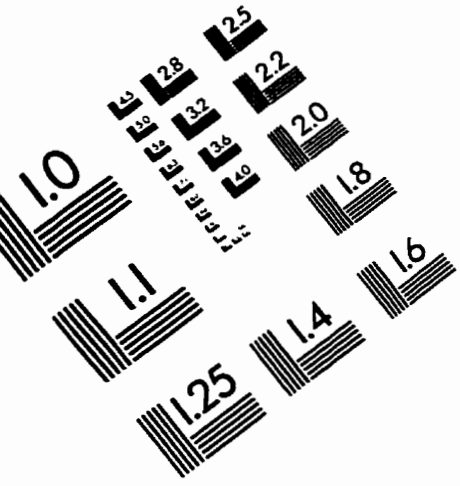

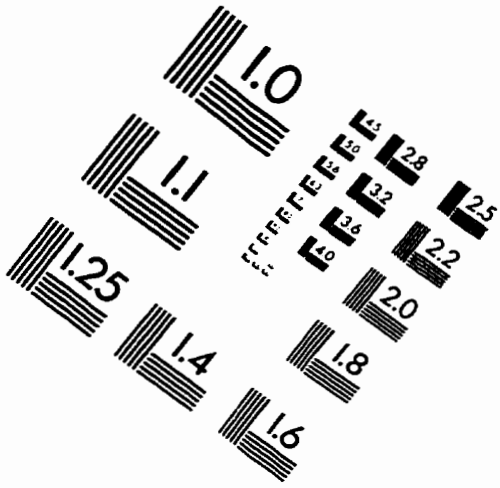

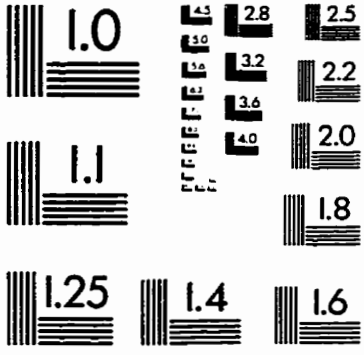

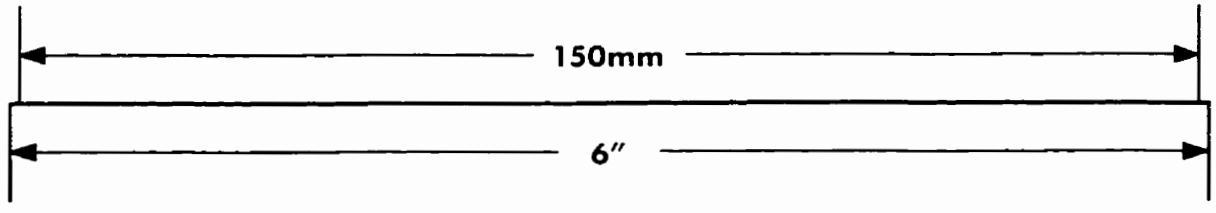

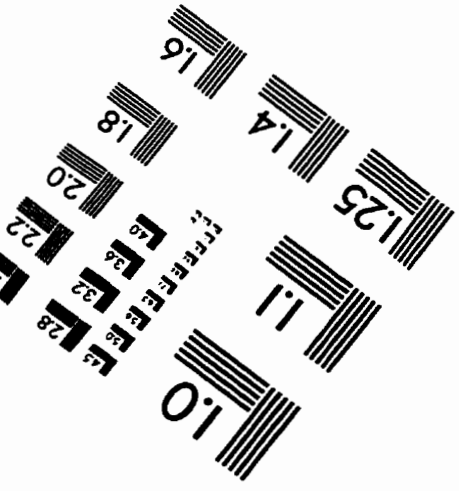

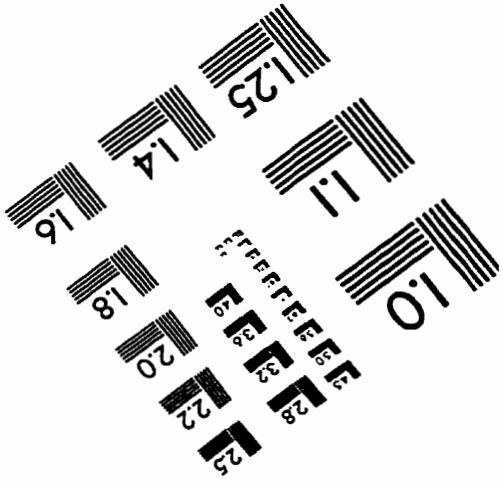

APPLIED IMAGE, Inc
1653 East Main Street
Rochester, NY 14609 USA
Phone: 716/482-0300
Fax: 716/288-5989